Department of Chemical Engineering

Faculty of Engineering and the Built Environment

University of Cape Town

Using Simulation and Laboratory Validation to Develop a $MnCO_3$ Recovery Process using CO_2

Author: Thabo Sibanda

Supervisor: Prof. Alison Lewis

Co-Supervisors: Jemitias Chivavava and Senzo Mgabhi

February 2025

Dissertation submitted in fulfilment of the requirements for the degree of Master of Science in Chemical Engineering

Declaration

Plagiarism Declaration:

I know the meaning of plagiarism and declare that all the work in the document, except for that which is properly acknowledged, is my own. This thesis/dissertation has been submitted to the Turnitin module (or equivalent similarity and originality checking software), and I confirm that my supervisor has seen my report and that any concerns revealed by such have been resolved with my supervisor.

Signed by candidate

Signed: Thabo Sibanda

16 February 2025

Acknowledgements

It is with God that I was able to complete this milestone, with that, I thank Him wholeheartedly. My mother in heaven, your son has completed a major milestone, and I know you were always watching over me. I love you and thank you so much.

I would like to thank Prof. Alison E. Lewis for entrusting me with this opportunity and allowing me to be part of the Crystallization and Precipitation Research (CPU) Unit. I thank Hilton Heydenrych for believing in me, his patience and motivation in both my work and career. The opportunity to complete my master's is owed to you.

I would like to express my deepest gratitude to Jemitias Chivavava and Senzo Mgabhi for their unwavering supervision, guidance, support, and motivation throughout the research and writing of this thesis. Their expertise and profound knowledge in precipitation science proved to be invaluable in both the laboratory experiments and the successful completion of this work. Without their precious contributions, the understanding and execution of this research would not have been possible. For this, I am deeply and truly grateful.

To my fellow CPU research mates, Madimetsa Matau, Jac Sussens, Tawanda William Mumvumi, and Buhle Nxiwa, I thank you for all your challenging questions and intense discussions we had in the seminars and on our desks. All these positively contributed a lot to completing this thesis.

A special thank you goes to: Mr Clint Prinsloo for his assistance in the fabrication of the reactor used for this work and for providing technical support; and Miranda Waldron, Mrs Charney Anderson Small, and Rachel Cupido for providing technical analytical support.

I am grateful to the Helmut & Babs Amos Scholarship by the DAAD-Stiftung for their generous financial support for my studies, and the Manganese Metal Company for funding this research work and providing their technical expertise.

Finally, I extend my deepest appreciation to my partner, Karabo Johanna Ndlovu, for always being there for me to steadfast emotional support, your unwavering belief in my abilities, and your constant reassurance throughout this journey. To my friends, Londiwe Nobanda and Nontlantla Mkwenkweni, thank you for your relentless encouragement and camaraderie; your reminders to persevere inspired me to strive harder each day. Lastly, I am forever indebted to my family for their countless sacrifices, patience, and unwavering belief in my goals. This achievement would not have been possible without their unconditional support.

Abstract

Manganese (Mn) is a critical metal in the production of lithium-ion battery (LiB) precursors due to its role in improving safety, stability and promoting higher efficiency and faster charging of LiBs. Battery-grade Mn or High Purity Manganese Sulphate Monohydrate (HPMSM, $MnSO_4 \cdot H_2O$), a key LiB precursor, requires low Mg and Ca content (< 0.01 wt.% each). Industrial $MnSO_4$ pregnant leach solutions are a valuable source of HPMSM but conventional purification using electrowinning is energy-intensive, unsustainable, and environmentally harmful. **Therefore, this study aimed to investigate the feasibility of chemical precipitation using a greenhouse gas (carbon dioxide gas, CO_2) and ammonia (NH_3) as a sustainable and cheaper alternative purification method.** A high-concentration industrial $MnSO_4$ pregnant leach solution containing at least 93.9 wt.% Mn^{2+}, 2.23 wt.% Mg^{2+}, and 0.14 wt.% Ca^{2+} was used. The results on the effect of pH from thermodynamic simulations were compared to experimental results. Experimental results investigated the effect of pH from 5.0 to 6.6 and CO_2 bubbling times from 1 to 12 h using a 1.0 L semi-batch and continuously stirred glass reactor at ambient temperature and pressure. The CO_2 was sparged at 0.4 L/min and the agitator speed was 500 rpm.

The thermodynamic simulation predicted more than 94% Mn^{2+} recovery at pH > 5.0, with optimal Mn^{2+} selectivity at pH < 6.6. The experimental results showed optimal Mn^{2+} recovery of 61.3% at pH 6.6 and 8 h CO_2 bubbling time, with the rejection of 57.6% Mg^{2+} and 46.3% Ca^{2+} from the $MnCO_3$ precipitate, respectively. The discrepancy between simulation and experimental results was attributed to the slow dissolution rate of CO_2. Finally, regardless of the CO_2 bubbling time and pH, the washed $MnCO_3$ precipitate contained at least 98.8% Mn, 0.15% Ca, and 0.05% Mg, meeting high-purity Mn specifications, but slightly lower than the requirements for battery grade Mn (> 99.9 wt.%, ultra-high-purity). The CO_2 bubbling time and pH have a significant influence on both the recovery of Mn^{2+} and the rejection of Mg^{2+} and Ca^{2+}. It is recommended that future work to explore the influence of pH 6.6-7.0, the effect of increasing partial pressure of CO_2, and the use of nanobubbles to enhance the CO_2 absorption. This study showed that carbonate precipitation using CO_2 and NH_3 can selectively recover Mn^{2+} from an industrial $MnSO_4$ leachate containing high Mg^{2+} and Ca^{2+} impurities, offering a sustainable process with great potential for industrial application.

Table of Contents

List of Figures

List of Tables

Glossary

Abbreviation List

HPMSM	High Purity Manganese Sulphate Monohydrate ($MnSO_4.H_2O$)
ICP-MS	Inductively Coupled Plasma Mass Spectrometry
IAP	Ionic Activity Product
XRD	X-Ray Diffraction
SEM	Scanning Electron Microscopy
PSD	Particle Size Distribution
EMM	Electrolytic Manganese Metal
LiB	Lithium Ion Battery
PLS	Pregnant Leaching Solution
EV	Electric Vehicle
NMC	Nickel-Manganese-Cobalt
HPMSS	High Purity Manganese Sulphate Solution

Nomenclature

CO_2	Carbon dioxide gas
wt.%	Weight percentage
NH_3 (aq)	28-30 wt.% ammonia solution
$MnCO_3$	Manganese carbonate
Mn	Manganese metal
Mn^{2+}	Manganese ion in solution
μ	Chemical potential (J/mol)
μ^*	Equilibrium Chemical potential (J/mol)
$\Delta\mu$	Difference in chemical potential (J/mol)
ρ	Density (kg/m^3)
a	activity (mol/dm^3)
a^*	Equilibrium activity (mol/dm^3)
R	Universal gas constant
T	Absolute temperature (K)
K_{SP}	Solubility product
S or ΔC	Supersaturation ratio
$v.$	Number of moles of ions (moles)
C	Actual concentration (mol/L)
C_{eq}	Equilibrium concentration (mol/L)
ΔG	Change of Gibbs energy (kJ)
B^0_{hom}	Homogeneous nucleation rate
B^0_{het}	Heterogeneous nucleation rate
B_{sec}	Secondary nucleation rate
J_A	Gas mass flux ($mol.m^{-2}.s^{-1}$)
D_{CO2}	Carbon dioxide binary diffusion coefficient ($m^2.s^{-1}$)
Mg	Magnesium metal

Mg^{2+}	Magnesium ion in solution
Ca	Calcium metal
Ca^{2+}	Calcium ion in solution

1 INTRODUCTION

This section explains the importance of this study for purifying industrial manganese (II) sulphate solution ($MnSO_4$) in South Africa and globally to supply high-purity $MnSO_4.H_2O$.

1.1 Background

Manganese (Mn), in the form of high-purity manganese sulphate monohydrate (HPMSM, $MnSO_4.H_2O$) is increasingly used to produce nickel-manganese-cobalt (NMC) cathode precursors for lithium-ion batteries (LiBs) used in the electric vehicle and energy storage systems (Ding et al., 2019, Fleischmann et al., 2023, International Energy Agency, 2023). Mn improves safety, and stability and has a low internal resistance, which promotes higher efficiency and faster charging of LiBs (Yu et al., 2019a, Zhang et al., 2018). According to the Benchmark Mineral Intelligence (2020) report, the demand for HPMSM is expected to increase by 25% per year from 2021 to 2031, with a forecasted supply deficit of 721 kilo tonnes by 2040.

South Africa has the largest Mn ore deposits globally and could be a potential key supplier of HPMSM. Battery-grade Mn, or HPMSM, is characterized by extremely low impurity concentrations of magnesium and calcium, typically below 0.01 wt.% each. This grade of Mn is produced primarily through the processing of Mn ore, which in South Africa consists mainly of pyrolusite (MnO_2), bixbyite (Mn_2O_3), hausmannite (Mn_3O_4), and impurities such as hematite (Fe_2O_3), magnesium oxide (MgO), silica (SiO_2), calcium oxide (CaO), and aluminium (III) oxide (Al_2O_3) (Nayl et al., 2011, Tangstad, 2013). After physical beneficiation, the Mn ore is processed via a hydrometallurgical route. During the leaching stage, Mn is dissolved using sulphuric acid (H_2SO_4) in a reducing environment with sulphur dioxide (SO_2) or sodium hypochlorite (NaClO) reductants. However, this also co-extracts iron (Fe^{3+}), magnesium (Mg^{2+}), calcium (Ca^{2+}), and other base metals such as copper (Cu^{2+}), nickel (Ni^{2+}), zinc (Zn^{2+}), and cobalt (Co^{2+}). This contaminates the pregnant leach solution (PLS) of manganese (II) sulphate ($MnSO_4$). The Fe^{3+} and base metal impurities (Cu^{2+}, Ni^{2+}, Zn^{2+}, and Co^{2+}) are removed using hydrolysis and selective chemical precipitation, respectively. However, the purified $MnSO_4$ PLS still has Mg^{2+} and Ca^{2+} with concentrations higher than 0.1 wt.%, which would lead to reduced battery capacity if used to produce LiB precursors (Gomez-Martin et al., 2022, Zou et al., 2016).

Electrowinning (reductive precipitation) is conventionally used to purify the $MnSO_4$ PLS and produces a high-purity electrolytic manganese metal (EMM) (Lu et al., 2016, Lyu et al., 2021). The significant advantage of electrowinning is its production of EMM with Mg and Ca content below 0.01 wt.%, meeting the LiB precursor requirements (Nie et al., 2013). However, this process is energy-intensive and generates about 6 to 7 tonnes of waste residue per ton of EMM produced (Ning et al., 2010, Li et al., 2018). This process also has a large carbon footprint and technical challenges. For these reasons, electrowinning is not suitable for sustainable battery-grade Mn production. This has driven the search

for innovative, sustainable, and cheaper technologies to purify the industrial $MnSO_4$ solution and produce HPMSM.

Chemical precipitation provides an alternative cheaper and easy-to-operate process for selective recovery of Mn from industrial $MnSO_4$ solutions. Chemical precipitation methods to produce hydroxides, oxides, sulphides, and carbonates have been studied by various investigators (Zhang and Cheng, 2007b, Zhang et al., 2010, Lin et al., 2016b, Wen et al., 2024a). Among these, carbonate precipitation shows the greatest potential for selectively recovering Mn, i.e., minimizing the co-precipitation of Mg^{2+} and Ca^{2+}, and can thus potentially meet the specifications for the LiB precursor (Pakarinen and Paatero, 2011). Therefore, this study aims to investigate carbonate precipitation as a viable and sustainable alternative to electrowinning for the purification of industrial $MnSO_4$ solutions, contributing to the global supply of high-purity Mn for LiBs.

1.2 Problem statement

Although electrowinning is conventionally used to purify industrial $MnSO_4$ pregnant leach solutions, it is unsustainable. This is because it is energy-intensive, large carbon footprint, and produces large amounts of waste. Carbonate precipitation provides a cheaper method of purification as it can selectively recover Mn^{2+} from solutions containing Mg^{2+} and Ca^{2+} impurities (Zhang et al., 2010, Lin et al., 2016b, Muanda and Omalanga, 2021). Additionally, the utilisation of carbon dioxide (CO_2), a greenhouse gas, as a precipitant presents a potentially sustainable and environmentally friendly process that aligns with global efforts to reduce carbon emissions.

The use of CO_2 to recover $MnCO_3$ from dilute Mn pregnant solutions ($Mn^{2+} < 5$ g/L) has been successfully demonstrated (Yu et al., 2019b, Wang et al., 2016, Hongliang et al., 2016). However, its use in high-concentration Mn solutions ($Mn^{2+} > 50$ g/L) remains largely unexplored. Furthermore, the recovery efficiency and $MnCO_3$ purity from such high concentrations has not been evaluated or compared to electrowinning. Therefore, this study aimed to investigate the use of CO_2 gas for the selective precipitation of $MnCO_3$ from a high-concentration industrial $MnSO_4$ pregnant leach solution and determine its ability to produce high-purity $MnCO_3$ suitable for LiB precursor production. However, downstream processing of $MnCO_3$ typically releases CO_2 back into the atmosphere. To enhance sustainability, the overall future industrial $MnCO_3$ production process using CO_2 should explore a closed-loop system that captures and recycles the emitted CO_2, thereby minimizing net carbon output.

1.3 Aims and objectives

This study aimed to investigate the use of CO_2 gas as a precipitant to selectively recover $MnCO_3$ from an industrial $MnSO_4$ pregnant leach solution using a semi-batch system.

The objectives of this study were to:

1. determine the feasibility of precipitating $MnCO_3$ from an industrial pregnant solution using CO_2 gas and aqueous NH_3; and to identify operating conditions using thermodynamic simulation.

2. investigate the effect of pH and CO_2 bubbling time experimentally on the recovery and purity of the $MnCO_3$ precipitate.

1.4 Scope and limitations

This study was set to investigate and validate thermodynamic simulation results experimentally to develop a $MnCO_3$ precipitation process using CO_2 gas and NH_3 (aq). The industrial $MnSO_4$ pregnant leach solution (Mn^{2+} > 50 g/L) was comprised of at least 93.9 wt.% Mn^{2+}, 2.23 wt.% Mg^{2+}, and 0.14 wt.% Ca^{2+}. The investigated parameters were limited to the solution pH value and CO_2 bubbling time. The pH values tested were obtained from the thermodynamic simulation, which favoured minimal Mg^{2+} and Ca^{2+} co-precipitation and promoted high recovery of Mn^{2+}. The $MnCO_3$ precipitate was analysed but was not dissolved in an acid to form high-purity $MnSO_4$. No economic calculations were performed in this study; however, reagent usage was considered as a basis for assessing the industrial feasibility of the study.

1.5 Structure of Thesis

This thesis is comprised of six chapters, starting with Chapter 1, which introduces the research, aims, and scope of the study. Chapter 2 outlines the precipitation theory, which includes supersaturation, nucleation, particle growth, and gas-liquid theory. In Chapter 3, a summary of the relevant literature on operating conditions and parameters that affect precipitation is reviewed. Chapter 4 provides a detailed description of the thermodynamic simulations, experimental setup, procedure, and analytical techniques used in this study. Results obtained from the experiments are presented and discussed in Chapter 5. Chapter 6 concludes the study by presenting its key findings and recommendations for further investigations.

2 THEORY

This chapter introduces the fundamentals of precipitation theory. The concepts of supersaturation and metal carbonate solubility are defined and discussed because they affect kinetics processes like nucleation, crystal growth, aggregation, agglomeration, and the resulting crystal structure and morphology. Lastly, the gas-liquid mass transfer principles are summarized. Together, these theories will aid in developing the methodology and experimental design, interpreting the results, and answering critical questions for this study.

2.1 Precipitation

Precipitation is a reaction in which sparingly soluble solids or crystals are formed rapidly from a liquid solution phase. It is industrially employed in a wide range of applications like the production of pharmaceuticals, dyes, pigments and paints, and the recovery of heavy metals from process streams and wastewaters (Myerson, 2002, Lewis, 2019). While precipitation is widely used for manganese (Mn) recovery, it is one of several technologies available for this purpose. A brief description of these technologies is shown in Table 2.1.

Table 2.1: Commonly used technologies for Mn recovery from aqueous solutions (Nie et al., 2013, Farrah et al., 2007, Wang et al., 2019, Choppin et al., 2002).

Technology	Separation principle	Advantages	Disadvantages
Electrowinning (reductive precipitation)	Converts soluble Mn^{2+} to metallic Mn^{0} by supplying electrons using electric current.	• High purity	• Energy-intensive • Produces large amounts of waste. • Large carbon footprint.
Crystallisation	Separates metals using the difference in their solubilities under different conditions	• High recovery	• Co-crystallises magnesium and calcium. • Requires multiple repeats for solutions with high concentrations, increasing operating costs.
Solvent Extraction	The Mn^{2+} ions are extracted and separated from other metal ions in solution using an organic solvent.	• Ease of operation • Good performance • High purity	• Poor separation of Mn from calcium • High solvent cost • Requires multiple extraction stages, increasing operating costs and fire risk.

Technology	Separation principle	Advantages	Disadvantages
Ion-exchange	Exchanges ions between those dissolved in an aqueous solution or gas and those in a solid cation exchange resin.	• High selectivity	• Suited for trace metals due to limited resin capacity. • Poor separation of Mn from calcium. • Requires multiple extraction stages, increasing operating costs.
Chemical precipitation	Reagents added to produce a sparingly soluble salt that crystallises out of the solution	• Cost-effective • Well-developed • High purity products	• High sensitivity to pH • May have poor selectivity • Produces sludge.

From the different technologies, electrowinning and chemical precipitation are better suited to treat industrial $MnSO_4$ pregnant leach solutions. This is because they can produce high purity Mn products on a large scale from a variety of solutions. In the case of chemical precipitation, the use of carbon dioxide (CO_2) as a precipitant offers a potential environmentally friendly process for recovering Mn because it is cheaper, readily available, and can achieve high recoveries.

2.1.1 The mechanism of CO_2 gas dissolution and speciation

The CO_2 gas first dissolves and then speciates into carbonate species as shown by:

$$CO_2\ (g) \rightleftharpoons CO_2\ (aq) \tag{2-1}$$

$$CO_2\ (aq) + H_2O\ (l) \rightleftharpoons H_2CO_3\ (aq) \tag{2-2}$$

$$H_2CO_3\ (aq) \rightleftharpoons HCO_3^-(aq) + H^+(aq) \tag{2-3}$$

$$HCO_3^-(aq) \rightleftharpoons CO_3^{2-}(aq) + H^+(aq) \tag{2-4}$$

The hydration of CO_2 (aq) is kinetically slow at pH < 8, but is relatively rapid at pH > 11 (Stumm and Morgan, 1996). This is because at high pH, the high amount of OH^- ions react with both H^+ ions and HCO_3^- shown by Equation (2-5) (Zeng et al., 2013, Zhu et al., 2017):

$$CO_2\ (aq) + OH^-(aq) \rightleftharpoons HCO_3^-(aq) \tag{2-5}$$

From these all equations, the total carbonate concentration (C_T) in solution is defined as:

$$[C_T] = [H_2CO_3^*\ (aq)] + [HCO_3^-(aq)] + [CO_3^{2-}(aq)] \tag{2-6}$$

2.2 Supersaturation

Precipitation is thermodynamically driven by supersaturation, which governs the nucleation and growth rates. Supersaturation occurs when the concentration of the dissolved solute exceeds its equilibrium solubility. This state is quantified by the difference in the solute chemical potential ($\Delta\mu$) between the actual chemical potential (μ) of a solute in a supersaturated solution and its equilibrium chemical potential (μ_{eq}) of the solid phase, as expressed by Equation (2-7):

$$\Delta\mu = \mu - \mu_{eq} = \mathrm{RT}ln\left(\frac{a}{a^*}\right) \tag{2-7}$$

Where R, T, a, and a^* is the universal gas constant, absolute temperature, actual activity of the reacting species in solution, and the equilibrium activity of the reacting species, respectively. Therefore, $\Delta\mu = 0$ defines equilibrium, at $\Delta\mu > 0$, spontaneous precipitation may occur, and $\Delta\mu < 0$ means dissolution of the precipitate becomes spontaneous.

An increased level of supersaturation enhances the rate of nucleation, crystal growth, and aggregation (Myerson et al., 2019). The solubility product constant (K_{SP}), the product of the activity of the ionic species, governs the equilibrium between the precipitate and its ions in solution, as shown in Equation (2-8):

$$K_{SP} = ({a_A}^*)^x \times ({a_B}^*)^y \tag{2-8}$$

Where ${a_A}^*$ and ${a_B}^*$ represent equilibrium activities of reactants A and B, respectively. The K_{SP} of a substance indicates the maximum concentration of the ionic substance in water at a specific temperature. Myerson (2002) describe the level of supersaturation using a ratio:

$$S = \frac{{a_A}^x \times {a_B}^y}{K_{SP}} \tag{2-9}$$

Supersaturation is most commonly expressed (Söhnel and Garside, 1992) as:

$$S = \left(\frac{{a^{v^+}}_A \times {a^{v^+}}_B}{K_{SP}}\right)^{\frac{1}{v}}, \qquad v = v^+ + v^- \tag{2-10}$$

Where v is the number of moles of ions formed from one mole of electrolyte. The product value of ${a^{v^+}}_A \times {a^{v^+}}_B$ is defined as an ionic activity product (IAP), in which if IAP > K_{SP}, the solution is supersaturated, and precipitation occurs. Alternatively, supersaturation is expressed using concentration:

$$S = \frac{C}{C_{eq}} \ or \ \Delta C = C - C_{eq} \tag{2-11}$$

Where C and C_{eq} represent the actual and equilibrium concentrations of the dissolved solids, respectively. Precipitation occurs when a $S > 1$ or $\Delta C > 0$.

2.2.1 Solubility of metal carbonates

Table 2.2 shows the K_{SP} values of $MnCO_3$, $MgCO_3$ and calcite $CaCO_3$ at 25°C. These low K_{SP} values indicate sparing solubility. Among them, $MnCO_3$ has the lowest K_{SP}, which means it is the least soluble and would preferentially precipitate first, followed by $CaCO_3$ and then $MgCO_3$.

Table 2.2. Solubility Products of metal carbonates at 25°C (Speight, 2017).

Metal carbonate	Formula	Solubility Product Coefficient (K_{SP})
Manganese carbonate	$MnCO_3$	2.34×10^{-11}
Magnesium carbonate	$MgCO_3$	6.82×10^{-6}
Calcium carbonate	$CaCO_3$	3.36×10^{-9}

The operating conditions such as pH, temperature, pressure, and concentration determine the amount of solute required to make a saturated solution (Myerson, 2002). Metal carbonate solubility decreases with increasing pH and temperature (Beckmann, 2013, Gamsjager et al., 1998). While pressure strongly affects the solubilities of gases dissolved in liquids, it has a less significant effect on solids. Higher metal concentrations in solutions increases the supersaturation ratio, as seen via the Equation (2-11). A supersaturated state is crucial for precipitation to occur, which can even happen when the starting reactants are all soluble. For instance, precipitation can be triggered by the formation of a highly insoluble product from a reaction between soluble components.

2.3 Kinetic processes

Kinetic processes for precipitation determine the mechanisms of crystal formation and the rate at which crystals form. These processes include nucleation, growth, aggregation, and agglomeration, which influence the change in particle size distribution over time.

2.3.1 Nucleation

Nucleation is described as the birth of new nuclei and the first-order phase transition (Christo N, 2015, Stumm and Morgan, 1996). Nucleation is divided into primary and secondary mechanisms, as summarized in Figure 2.1.

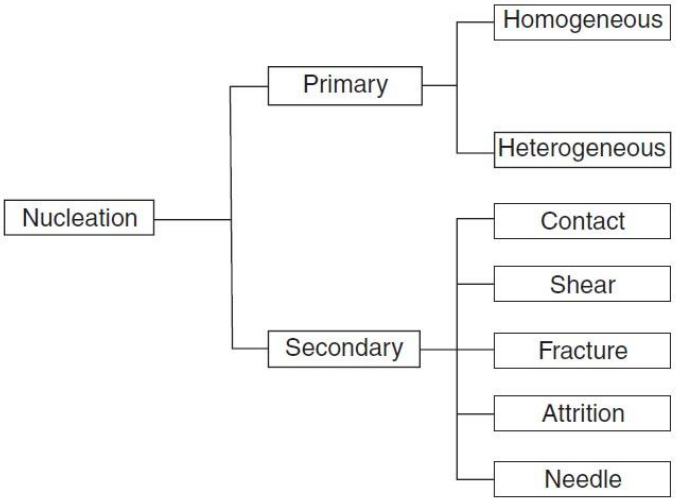

Figure 2.1: Mechanisms and modes of nucleation (adapted from Jones (2002)).

2.3.1.1 Primary nucleation

Primary nucleation, according to the classical nucleation theory, is the formation of nuclei from a solution where no pre-existing crystalline material is present. Primary nucleation subdivided into homogenous and heterogeneous (Jones, 2002). Homogenous nucleation is the spontaneous formation of nuclei from a supersaturated solution with only solute and solvent molecules, while the presence of foreign particles or surfaces such as dust induces heterogeneous nucleation.

2.3.1.1.1 Homogeneous nucleation

Thermodynamically, homogenous nucleation is defined as the change in the total free energy required to form a cluster, (ΔG):

$$\Delta G = \Delta G_s + \Delta G_V = \beta L^2 \sigma + \alpha L^3 \Delta G_V \tag{2-12}$$

where ΔG_s is the surface excess free energy and ΔG_V is the volume excess free energy. The term ΔG_V describes the spontaneous tendency of a supersaturated solution to undergo deposition. It becomes negative because the solid state is more stable than the liquid. Therefore, the Gibbs free energy of the system is decreased. On the other hand, ΔG_s favours dissolution. The factors β and α are for the volume and the area of the shape (based on the characteristic length L), respectively, and σ is the surface tension. Based on the diameter d of the nuclei, the area factor $\beta = \pi$ and the volume factor $\alpha = \pi/6$ are found for a spherical nucleus (Myerson et al., 2019), from which Equation (2-12) for spherical clusters with radius r, becomes:

$$\Delta G = 4\pi r^2 \sigma + \frac{4}{3}\pi r^3 \Delta G_v \tag{2-13}$$

where ΔG_v is the free energy of transformation per unit volume. Beckmann (2013) used a vapour phase droplets theory to explain the nucleation mechanism. In this theory, the droplet size equals the stable clusters of its crystal size at equilibrium. The crystal size is defined by Equation (2-14), where the total ΔG reaches a maximum value called the activation barrier for nucleation (ΔG_{crit}):

$$r_c = -\frac{2\sigma}{\Delta G_v} \tag{2-14}$$

The size of the droplet grows if ΔG becomes negative upon adding a building block (Beckmann, 2013). For clusters bigger than r_c, ΔG continuously drops, making growth energetically favourable. Figure 2.2 shows that cluster sizes beyond the critical size have the minimum Gibbs free energy and ΔG_V decreases and ΔG_s increases as the radius of the cluster increases.

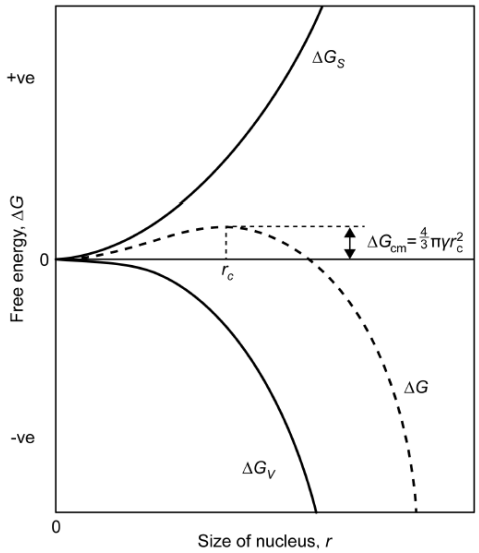

Figure 2.2: Gibbs free energy change for nucleation versus the size of the nucleus (Mullin, 2001)

The homogeneous nucleation rate that depends on the supersaturation ratio is shown in Equation (2-15) (Jones, 2002, Myerson et al., 2019):

$$B^0{}_{hom} = A_{hom}\, exp\left[-\frac{16\pi\sigma^3 v^2}{3k^3T^3(lnS)^2}\right] \tag{2-15}$$

where A_{hom} is the pre-exponential factor, ν is the molecular volume in m^3/mol, k is Boltzmann's constant in J/K, T is the absolute temperature in K, and S is the supersaturation ratio. It is evident that the homogeneous nucleation rate increases with increasing temperature and supersaturation and decreases with an increase in surface energy.

2.3.1.1.2 Heterogeneous nucleation

In heterogeneous nucleation, the presence of foreign particles substantially decreases the ΔG_{crit}, the energy required to form stable nuclei, and significantly occur at low supersaturation (Jones, 2002). The heterogeneous nucleation rate is defined by Equation (2-16) (Jones, 2002, Markov, 2016):

$$B^0{}_{het} = A_{het}\, exp\left[-\frac{16\pi\sigma^3 v^2 f(\phi)}{3k^3T^3(lnS)^2}\right] \tag{2-16}$$

where $f(\phi)$ is the correction factor for the surface energy reduction defined by Mullin (2001):

$$f(\phi) = \frac{(2+cos\theta)(1-cos\theta)^2}{4} \tag{2-17}$$

where θ is the contact angle between the crystalline deposit and the foreign solid surface or wetting in a solid-liquid system, which varies between 0 and 180°.

2.3.1.2 Secondary nucleation

Secondary nucleation is defined as the formation of nuclei from the presence of existing crystals from the same solute in a supersaturated solution (Botsaris, 1976). The parent crystals act as catalysts for the

new crystals by providing a surface, which occurs at low supersaturation, therefore, requiring less energy. Secondary nucleation can also be induced by introducing small crystals of the precipitating solid or other material into the supersaturated solution to start nucleation. This is known as seeding, in which the seeds provide a surface for nucleation and crystal growth, which hinders spontaneous nucleation (Myerson et al., 2019).

The secondary nuclei can be formed through initial breeding or dust breeding, collision breeding and fluid shear. During initial breeding, the existing crystals shed extremely small fragments that serve as sites for the growth of new crystals.

The existing parent crystals can collide with each other and the vessel walls or the impeller to produce small fragments. This is collision breeding. The fluid shear mechanism suggests that the shearing of the layer between the crystal and the solution by agitation is sufficient to remove a layer of the adsorbed molecules into the solution, where they grow into crystals (Myerson et al., 2019). For materials with moderate to high solubility, collision or attrition breeding is believed to be the most significant secondary nucleation mechanism (Doran, 2013). The rate of secondary nucleation is a function of supersaturation (ΔC), degree of agitation (N_S), and suspension or magna density (M_T), and expressed (Myerson et al., 2019) as:

$$B_{sec} = k'_N N_S^i M_T^j (\Delta C^n) \tag{2-18}$$

where the nucleation constant, k'_N, is dependent on the conditions of the reactor or crystallizer. The order of the dependence of secondary nucleation on impeller speed, suspension magna density, and supersaturation is indicated by the exponents *i, j,* and *n*, respectively. According to Jones (2002), the values of the exponents *i* and *n*, are within ranges 0-7.8 and 0.14-1.07, respectively.

2.3.2 Growth

In the presence of supersaturation, crystal growth of the nuclei begins as soon as stable nuclei have formed. These nuclei can be amorphous particles or tiny crystals that are usually nanoscopic in size and can spontaneously grow to macroscopic sizes (Myerson et al., 2019). Two main processes lead to the growth of crystals from a solution. First, growth units are transported from the bulk solution to the crystal surface by mass diffusion. Second, they are incorporated into the crystal lattice via a surface reaction process (Jones, 2002). Different crystal faces can grow at different rates. Therefore, the overall crystal habit is determined by the slowest growth process. Figure 2.3 shows the crystal growth mechanism on the surface of a growing crystal. According to the growth mechanism by Mullin (2001), the growth unit:

a) diffuses through the diffusion boundary layer,
b) absorbs onto the crystal surface,
c) is either incorporated into the lattice or desorbs back to the solution, and
d) loses its remaining solvation shells before the final lattice incorporation, if retained.

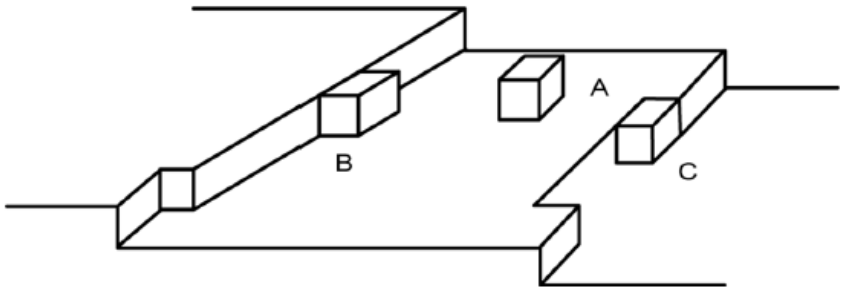

Figure 2.3: The crystal growth mechanism on the surface of a growing crystal (Myerson et al., 2019).

Site A binds only to the surface of a growing layer, while the molecule at site B binds to both the surface and the growth stage. At site C, the molecule is attached to three surfaces at a so-called kink site. From an energy perspective, C is more favourable than B, and B is more favourable than A (Myerson et al., 2019). The diffusion of the growth unit into the adsorption layer creates a concentration profile that creates supersaturation and is a driving force for crystal growth. The concentration profile on the crystal surface during diffusion and integration is depicted in Figure 2.4.

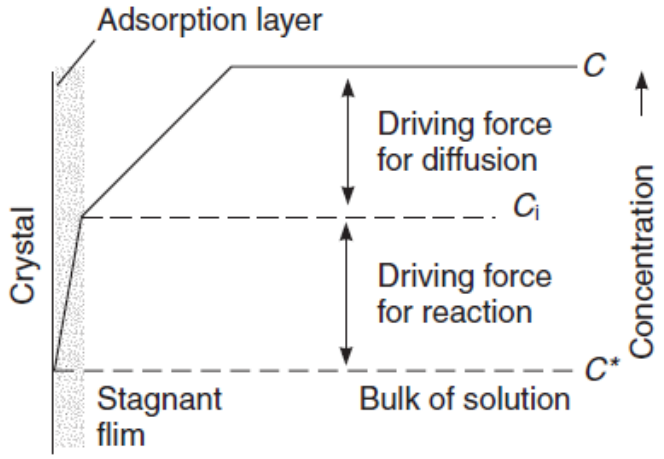

Figure 2.4: Growing crystal-solution interface (Jones, 2002).

The diffusive-convective transport and integration reaction driving forces are determined by the differences between the bulk solution concentration (C), the interfacial concentration (C_i), and the equilibrium solubility (C^*). The growth rate (G) can be expressed as:

$$G_d = k_d A(C - C_i)^g \tag{2-19}$$

$$G_r = k_r A(C_i - C^*)^g \tag{2-20}$$

$$G = k_g A(C - C^*)^g \tag{2-21}$$

where g is a growth order in the range of 5 and 10, A is the surface area of the crystal, k_d is the diffusion rate constant, k_r is the surface reaction rate constant, and k_g is the overall growth constant. The total resistance of diffusion and integration reaction in series is defined by equation (2-22):

$$\frac{1}{k_g} = \frac{1}{k_d} + \frac{1}{k_r} \tag{2-22}$$

The nucleation rate and growth rate are strongly affected by supersaturation, which then affects the crystal size as illustrated in Figure 2.5.

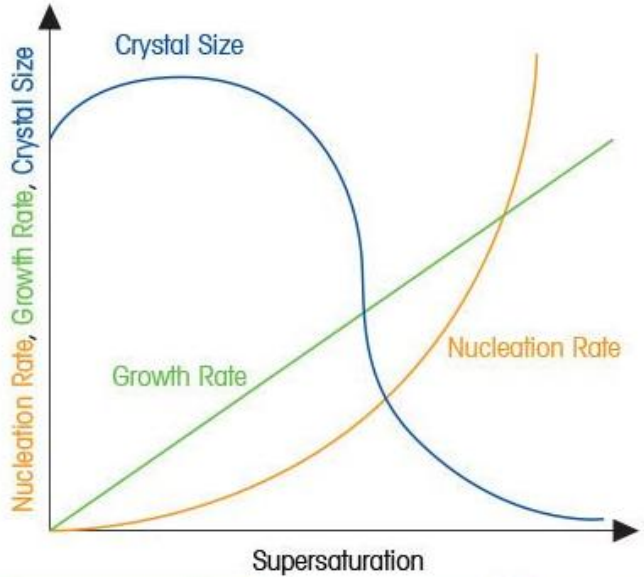

Figure 2.5: The effect of supersaturation on nucleation and growth rates (Mettler Toledo, 2024).

At low supersaturation, the crystal growth rate is faster than the nucleation rate, resulting in a larger crystal size distribution. Increased supersaturation leads to linearly increased nucleation and exponential growth rates. However, at higher supersaturation, the nucleation rate is faster than the growth rate, so a large number of smaller crystals are formed, but they grow more slowly, thus producing a smaller crystal size distribution. Therefore, controlling supersaturation is essential when it comes to producing crystals of the desired size.

2.3.3 Aggregation

Aggregation is the collision of individual particles that eventually aggregate into stable larger particles held in place by weak intermolecular forces such as van der Waals forces (Söhnel and Garside, 1992). These aggregates are loosely bound and can easily disintegrate. There are two aggregation methods, i.e., primary, and secondary aggregation. Primary aggregation has been suggested to occur due to diffusion field limitations or impurity action, particularly at high growth rates or surface nucleation (Jones, 1993).

Secondary aggregation is caused by the hydrodynamic factor when smaller particles, usually < 1 μm in size, move in the Brownian motion. This leads to perikinetic collisions and perikinetic aggregation. Particles with sizes greater than 1 μm move by fluid deformation caused by mechanical stirring or convective currents and this leads to orthokinetic collisions and orthokinetic aggregation (Jones, 2002, Myerson et al., 2019). The effectiveness of aggregate formation depends on particle interactions and is influenced by supersaturation. For stable aggregates to form, the colliding particles must overcome

repulsive forces and generate sufficient attractive forces to resist inertial forces that would otherwise cause them to disintegrate (Beckmann, 2013). Additionally, particle growth plays a role in cementing the particles together, stabilizing the aggregates.

2.3.4 Agglomeration

Agglomeration is the process by which stable aggregates are bonded together to form a larger particle (Jones, 2002, Beckmann, 2013). Compared to aggregates, these particles are held together more tightly and are more difficult to break apart. This is because they are supported by inner-solid bridges created between the aggregates and require supersaturation. At higher supersaturations, stronger agglomerates form due to an increased growth rate of the inner-solid bridges.

During precipitation, the separation of the solids from the liquid is crucial so that agglomeration can increase the separation efficiency. This is because agglomeration creates larger particles that are easy to filter out. The disadvantage of agglomeration is that the inner-solid bridges can trap the impure mother liquor, reducing the purity of the solid precipitate (Giulietti et al., 2001). Agglomeration is influenced by mixing intensity, pH, ionic strength, solids concentration, and supersaturation.

2.3.5 Effect of supersaturation on crystal structure and morphology of $MnCO_3$

In the $MnCO_3$ precipitation process, low supersaturation tends to form particles with well-defined crystal structures, such as rhombohedral crystals. Conversely, at high supersaturation, amorphous or poorly crystalline particles are formed. This is because, at low supersaturation, the growth rate is favoured over the nucleation rate, which allows for orderly crystal growth and as such, well-defined crystals are formed with smooth surfaces, whereas high supersaturation leads to higher nucleation rate than the growth rate, which means smaller crystals are produced with rough surfaces (Sunagawa, 2005).

Brugman et al. (2020) further supports that the $MnCO_3$ morphology changes significantly with supersaturation levels. At high supersaturation, the $MnCO_3$ particles become amorphous and rough; however, if given more time, the supersaturation is reduced, which transforms the particles into a more crystalline form. Furthermore, the crystal exhibits more spherical forms resulting from particle aggregation and agglomeration due to the increased number of nucleation sites. Furthermore, it has been demonstrated that intermediate supersaturation levels can produce distinct morphologies, such as hexagonal and rod-like structures (Yu et al., 2019a, Geng et al., 2019).

These are not only affected by the concentration of Mn^{2+} and the availability of HCO_3^- and CO_3^{2-} ions but also the presence of Mg^{2+} and Ca^{2+} impurities, which interfere with the nucleation of $MnCO_3$ particles, promoting the alternative crystal structures through co-precipitation (Loewenthal and Maais Gv, 1977). Therefore, high supersaturation levels lead to more rapid, less ordered crystal growth, and lower levels favour structured, rhombohedral forms. In the current work, rhombohedral structures are expected to form due to the use of CO_2, which often provides low supersaturation.

2.4 Gas-liquid mass transfer theory

In this study, CO_2 gas was used as a precipitant and was bubbled through an industrial $MnSO_4$ solution to recover $MnCO_3$. Therefore, understanding the principles of gas-liquid mass transfer is essential. Various models that describe the processes at the phase interface during the physical absorption of a gas to a liquid are available. These include steady-state two-film theory, unsteady-state Danckwerts' surface renewal theory, Levich's absorption model, and Higbie's penetration theory (Whitman, 1962, Charpentier, 1981, Higbie, 1935, Levich and Tobias, 1963). For illustration, the steady-state two-film theory is summarized below.

Three assumptions are made: the CO_2 gas is pure, so, no transport phenomena occurs; the gas and liquid interfaces have a laminar film; mass transfer is due to steady-state diffusion; interface is at equilibrium, with concentrations related by Henry's law; and the bulk sides are well mixed. The dissolution of CO_2 gas in the $MnSO_4$ solution takes place through the following steps:

1. Diffusion of CO_2 through the gas film
2. Absorption of CO_2 by the gas-liquid interface
3. Diffusion of CO_2 through the liquid film
4. Absorption of CO_2 into the bulk of the liquid

In steps 1 and 3, the gas must overcome resistances due to the gas and liquid film by the diffusion mechanism. According to Mishra and Kapoor (1978), these steps presents a mass-transfer limitation, and therefore, this section focuses on them only.

2.4.1 Diffusion of CO_2 through the gas and liquid film

The gas diffusion occurs if the bulk gas concentration is higher than interfacial concentration. The diffusion of the gas through the gas film is driven by the partial pressure gradient (p_g-p_l) of the solute, and that through the liquid is driven by the concentration gradient (c_g-c_l) (Wilhelm, 1985):

$$\frac{dW}{dt} = k_p(p_g - p_l) = k_c(c_g - c_l) \tag{2-23}$$

where W is the amount of absorbed gas, t is the time for this absorption, k_p is the coefficient of diffusion through the gas film, k_c is the coefficient of diffusion through the liquid film, and the subscripts g and l mean gas and liquid. The diffusion rate of a gas given by Equation (2-23) and is only constant at a constant temperature and pressure. The rate of diffusion given by Fick's first law defines the diffusion of a gas in solution as (Fick, 1855):

$$J_A = -D_{AB}\frac{dc_A}{dy} \tag{2-24}$$

Where J_A is molar flux (mol.m^{-2}.s^{-1}), D_{AB} is the binary diffusion coefficient for A in B (m^2.s^{-1}), and $\frac{dc_A}{dy}$ is the concentration gradient (mol.m^{-4}). The Speedy–Angell power-law can be used to determine the binary diffusion coefficient of a gas (Lu et al., 2013):

$$D_{CO_2} = D_O \left[\frac{T}{T_s} - 1\right]^m \quad (2\text{-}25)$$

where $D_O = 13.942 * 10^{-9} \frac{m^2}{s}$, Ts = 227.0 K, and m = 1.7094

The resistance of the gas diffusion is linked to the solubility of the gas determined by Henry's Law. This law states that the solubility of the CO_2 gas is proportional to its partial pressure as shown by Equation (2-26) (Wilhelm, 1985):

$$C^0_{CO_2} = K_{H,CO_2} \times P_{CO_2} \quad (2\text{-}26)$$

Where K_{H,CO_2} and P_{CO_2} is the Henry's constant in water at 25°C and partial pressure of CO_2, respectively. The value of K_{H,CO_2} has been reported by Dukes (2020) as 0.0365 $mol.L^{-1}.atm^{-1}$. The value for $\frac{1}{k_p} \approx 0$ since the assumed gas is pure. Therefore, the overall mass transfer coefficient is:

$$\frac{1}{K_L} = \frac{1}{k_p} + \frac{K_{H,CO_2}}{k_c} = \frac{0.0365}{k_c} \quad (2\text{-}27)$$

3 LITERATURE REVIEW

This section provides a summary of the sources of manganese, the production of the $MnSO_4$ leach solution, available technologies for treating industrial $MnSO_4$ leach solutions, and the application of carbonate precipitation as a purification technology. Although the literature covers a wide range of factors affecting precipitation, this review focuses on the effect of pH and CO_2 bubbling time on manganese recovery and selectivity.

3.1 Manganese production and uses

Manganese (Mn) occupies about 0.096% of the earth's crust, making it the twelfth most abundant element and the fourth most widely used metal worldwide after Fe, Al, and Cu (Zhang and Cheng, 2007a, International Manganese Institute, 2024). South Africa, Australia, Brazil, and China account for more than 85% of the world's manganese reserves of 1.9 billion metric tonnes (U.S. Geological Survey, 2024). It is estimated that 20 million metric tonnes of Mn ore was globally produced in 2023, of which most of it comes from South Africa, Gabon, Australia, Ghana, China, India, and Brazil (U.S. Geological Survey, 2024). About 90% of this Mn is used in the steel industry, while less than 10% is used as an alloying element with other metals and in applications such as agriculture and chemicals (Kesler and Simon, 2015). Additionally, approximately 2% to 3% of Mn is used in the manufacturing of batteries (International Manganese Institute, 2024).

The use of Mn in the production of lithium batteries (LiBs) is forecasted to increase due to the adoption of electric vehicle (EV) and energy storage technologies. In the production of LiBs, Mn is used to make the precursor for cathode materials in lithium-ion batteries used in EVs. Two prominent Mn-based cathode precursor types are nickel-manganese-cobalt (NMC) and lithium-manganese-oxide (LMO). The NMC precursor is synthesized by mixing nickel, manganese, and cobalt sulphate solutions in controlled ratios (Kartini et al., 2022). The LMO precursor, on the other hand, is prepared by mixing manganese (III) oxyhydroxide (MnOOH) and lithium hydroxide (LiOH) solutions (Chitrakar et al., 2001). Additionally, lithium iron manganese phosphate (LFMP or $Li(Fe,Mn)PO_4$) is a promising cathode material due to its high specific capacity, stable structure, safety, low price, and environmental friendliness (Sun et al., 2024, Zeng et al., 2025).

3.1.1 Sources of manganese

Mn can be produced from primary sources consisting of high-grade ores containing over 40% Mn or from secondary sources containing low-grade Mn (< 40%). The production of Mn from primary and secondary sources is summarized in the following sections.

Primary sources

The mineralogical composition of Mn ores directly impacts the efficiency of beneficiation and leaching processes. The majority of Mn generally comes from sediments where layers of manganese mineral oxides, carbonates, and less-appearing silicates and sulphides are mixed with iron (Kesler and Simon,

2015, Tangstad, 2013). Table 3.1 summarizes the most significant manganese-containing minerals and their Mn content.

Table 3.1: Significant Mn-containing minerals (Tangstad, 2013).

Mineral	Chemical Formula	Mn Content (%)
Oxide Types		
Pyrolusite	MnO_2	63.2
Vernadite	$MnO_2.H_2O$	44 - 52
Braunite	$3(Mn,Fe)_2O_3.MnSiO_3$	48.9 - 56.1
Braunite II	$7(Mn,Fe)_2O_3.CaSiO_3$	52.6
Manganite	γ-MnOOH	62.5
Psilomelane	$(K,Ba)(Mn^{2+}Mn^{4+})_8O_{16}(OH)_4$	48.6 - 49.6
Cryptomelane	$(K,Ba)Mn_8O_{16}.xH_2O$	55.8 - 56.8
Hollandite	$(Ba,K)Mn_8O_{16}.xH_2O$	42.5
Todorokite	$(Ca,Na,K)(Mn^{2+}Mn^{4+})_6O_{12}.xH_2O$	49.4 - 52.2
Hausmannite	$(Mn,Fe)_3O_4$	64.8
Jacobsite	Fe_2MnO_4	23.8
Bixbyite	$(Mn,Fe)_2O_3$	55.6
Carbonate Types		
Manganocalcite	$(Mn,Ca)CO_3$	< 20 - 25
Oligonite	$(Fe,Mn)CO_3$	23-32
Rhodochrosite	$MnCO_3$	47.6
Silicate Types		
Rhodonite	$MnSiO_3$	42
Tephroite	Mn_2SiO_4	54.4
Sulphide Types		
Alabandine	MnS	63.2
Gauerite	MnS_2	46.2

The Mn-containing minerals mainly consist of pyrolusite (MnO_2), bixbyite (Mn_2O_3), and hausmannite (Mn_3O_4). The presence of impurities such as hematite (Fe_2O_3), magnesium oxide (MgO), silica (SiO_2), calcium oxide (CaO), and aluminium (III) oxide (Al_2O_3) in Mn ores poses significant challenges in the production of high-purity Mn products (Nayl et al., 2011, Tangstad, 2013).

Secondary sources

Secondary sources of Mn like spent batteries and industrial residues offer a sustainable alternative to primary mining, reducing environmental impact while contributing to the circular economy (Zhang and Cheng, 2007a, Wu et al., 2024). With the increased use of LiBs, the recycled LiBs will become an increasingly important source of manganese in the near future.

A substantial secondary source of Mn is Electrolytic Manganese Residue (EMR), a major byproduct of manganese metal production. EMR can contain more than 7 wt.% of Mn depending on the production process (Wen et al., 2024b). There are over 130 million metric tonnes of EMR stockpiled globally, with China contributing more than 10 million tonnes of EMR per year (Li et al., 2018, Su et al., 2023). This substantial accumulation is because about 6 to 7 tonnes of EMR is generated per ton of electrolytic manganese metal produced.

Ferromanganese slag is another viable secondary source of Mn that can contribute to the global Mn supply. Baumgartner and Groot (2014) showed that it is possible to produce a high-purity Mn^{2+} leach solution from the ferromanganese slag. Rozelle et al. (2021) identified over 500 kilo tonnes of Mn in the byproducts from mining and metallurgical processes in Pennsylvania. Of this amount, 5.5 kilo tonnes was disposed of through acid mine drainage. This study showed that some waste streams from metallurgical processes may have significant amounts of Mn that could potentially be extracted.

3.1.2 The production process of the manganese pregnant leach solution

Figure 3.1 shows a typical flowsheet of the manganese production from ores. The production of the primary Mn-ore begins with beneficiation, in which a combination of crushing, grinding, milling, screening, washing, jigging, magnetic separation, and electrostatic separation produce ore concentrates with Mn > 35% (Singh et al., 2020).

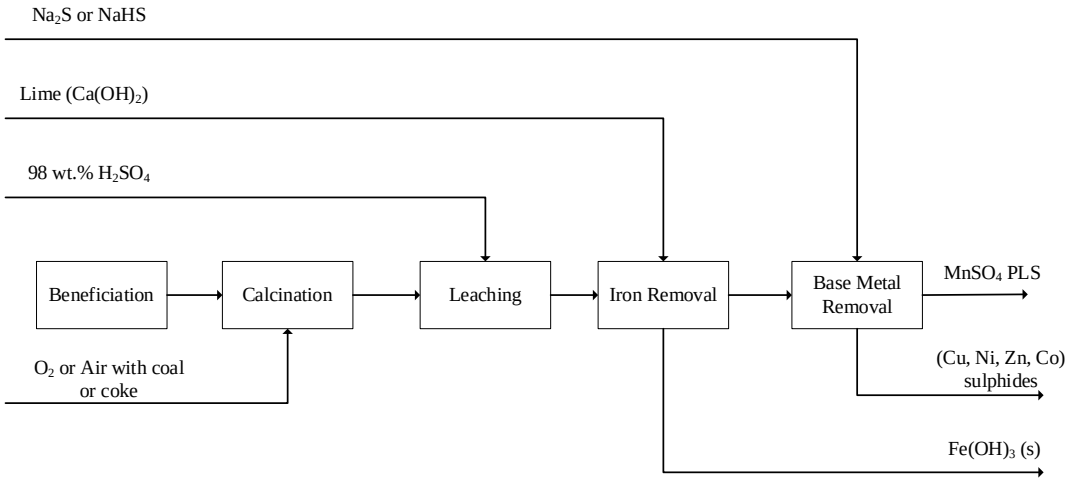

Figure 3.1: Typical process for producing manganese metal (adapted from Zhang and Cheng (2007a)).

The Mn ores in South Africa predominantly contain minerals with Mn oxidation states of +2, +3, +4, +6, and +7, such as MnO_2, Mn_2O_3, Mn_3O_4, etc. Higher oxidation states of manganese oxides are stable in acidic solutions and, thus, insoluble. To address this, conventional hydrometallurgical processing conventionally employs calcination at temperatures between 700 and 1200°C to reduce these oxides to soluble manganous oxide (MnO), which is readily soluble in sulphuric acid (H_2SO_4) in a reductive environment (Hariprasad et al., 2009, Nayl et al., 2011, Sorensen et al., 2010, Zhang and Cheng, 2007a). However, calcination is energy-intensive and may not always be necessary. Alternatively, chemical reduction using SO_2 or organic reductants such as lactose or sawdust can directly convert higher oxidation states of Mn oxides to soluble Mn^{2+} without the high-temperature treatment (You et al., 2015, Ismail et al., 2008).

The MnO is then leached using a concentrated H_2SO_4 in a reductive environment to form a pregnant leach solution (PLS) of manganese sulphate ($MnSO_4$) (Hariprasad et al., 2009). Sulphuric acid is preferred because of its cost-effectiveness and high extraction efficiency for MnO. Leaching occurs at

pH below 5, which co-leaches iron, base metals (copper, cobalt, nickel, and zinc), magnesium (Mg^{2+}), and calcium (Ca^{2+}) impurities.

Ferrous iron (Fe^{2+}) is firstly oxidized to ferric iron (Fe^{3+}) using air or oxygen at a pH of 2-5, and then Fe^{3+} is hydrolysed and precipitated as iron hydroxide ($Fe(OH)_3$) at the pH of 2.5-5.5 (Lin et al., 2016a, Stefánsson, 2007, Xinzhuang et al., 2021). The base metal impurities are removed by sulphide precipitation using either aqueous (Na_2S, NaHS, and NH_4S), or gaseous sulphide (H_2S) at a pH of 1.5-7.0 (Tokuda et al., 2008). It is generally challenging to separate Mg^{2+} and Ca^{2+} from the $MnSO_4$ solutions because they have similar ionic radii and solubility profiles to Mn^{2+}. Fluoride precipitation using either hydrogen fluoride (HF) or ammonium fluoride (NH_4F) is extensively and commonly used in China to precipitate and remove Mg^{2+} and Ca^{2+} as MgF_2 and CaF_2, respectively. However, this method introduces F^- as impurities which require further treatment of the $MnSO_4$ with extractors and adsorbents, and these ions can corrode the equipment used. Furthermore, the MgF_2 and CaF_2 precipitates are difficult to filter (Wang et al., 2019). Therefore, the remaining purified $MnSO_4$ pregnant leach solution still has Mg^{2+} and Ca^{2+} with concentrations higher than 0.1 wt.%, making the solution unacceptable to be used for LiB production as it would lead to low capacity (Gomez-Martin et al., 2022, Zou et al., 2016).

3.2 Application of precipitation in the recovery of manganese from leach solutions

This chapter discusses electrowinning and chemical precipitation as the viable technologies for the purification of industrial $MnSO_4$ solution.

3.2.1 Electrowinning

Electrowinning, otherwise known as electrodeposition or reductive precipitation, involves using electric current to supply electrons to reduce soluble Mn^{2+} to metallic Mn^0 or electrolytic manganese metal (EMM). Electrowinning is the most used process to purify industrial $MnSO_4$ pregnant leach solution because it produces a high-purity EMM with Mg and Ca content below 0.01 wt.% (Nie et al., 2013). The associated reactions that occur during electrowinning are (Harris and Auerswald, 1977):

Cathodic reactions:	**Potential (V)**	**Equation**
$Mn^{2+}{}_{(aq)} + {SO_4}^{2-}{}_{(aq)} + 2e^- \rightarrow Mn^0{}_{(s)} + {SO_4}^{2-}{}_{(aq)}$	-1.18	(3-1)
$Mg^{2+}{}_{(aq)} + {SO_4}^{2-}{}_{(aq)} + 2e^- \rightarrow Mg^0{}_{(s)} + {SO_4}^{2-}{}_{(aq)}$	-2.37	(3-2)
$Ca^{2+}{}_{(aq)} + {SO_4}^{2-}{}_{(aq)} + 2e^- \rightarrow Ca^0{}_{(s)} + {SO_4}^{2-}{}_{(aq)}$	-2.87	(3-3)
$2H_2O_{(l)} + 2e^- \rightarrow H_{2(g)} + 2OH^-{}_{(aq)}$	-0.83	(3-4)
$Mn^{2+}{}_{(aq)} + 2H_2O_{(l)} \rightarrow Mn(OH)_{2(s)} + 2H^+{}_{(aq)}$	-1.55	(3-5)
$2H^+{}_{(aq)} + 2e^- \rightarrow H_{2(g)}$	0.00	(3-6)

Anodic reactions:	**Potential (V)**	**Equation**
$2H_2O_{(l)} \rightarrow O_{2(g)} + 4H^+_{(aq)} + 4e^-$	+1.23	(3-7)
$SO_4{}^{2-}_{(aq)} + 2H^+_{(aq)} \rightarrow H_2SO_{4(aq)}$	-	(3-8)
$Mn^{2+}_{(aq)} + SO_4{}^{2-}_{(aq)} + O_{2(g)} + 2e^- \rightarrow MnO_{2(s)} + SO_4{}^{2-}_{(aq)}$	+1.21	(3-9)

The high negative reduction potentials of Mg^{2+} and Ca^{2+} impurities mean that Mn^{2+} is more easily reduced at the cathode. As such, these impurities will remain in solution during electrowinning, making the process highly selective for Mn^{2+} (Qin et al., 2019).Furthermore, since the reduction potentials of Mg^{2+} and Ca^{2+} are much more negative than that of water, hydrogen gas (Equation (3-4)) will form before these metals can deposit onto the cathode, further limiting the reduction of Mg^{2+} and Ca^{2+}. On the anodic side, H_2SO_4 is produced, and therefore the effluent solution is recycled back to the leaching stage (Harris and Auerswald, 1977). About 1.5% of Mn^{2+} ions are further oxidized to an unwanted MnO_2, as shown by the reaction (3-9) (Ning et al., 2010). Electrowinning is however energy-intensive, produces large amounts of waste, and has a large carbon footprint (Ning et al., 2010). Therefore, electrowinning is unsuitable for sustainable battery-grade Mn production.

3.2.2 Chemical precipitation

Chemical precipitation involves adding a precipitant to a solution with Mn^{2+} to produce a sparingly soluble salt. It is the most used process to remove heavy metals from wastewater or leach solutions (Masindi et al., 2022, Qasem et al., 2021). The recovery of Mn using chemical precipitation can be achieved by hydroxide, oxidative, sulphide and carbonate precipitation (Zhang and Cheng, 2007b, Zhang et al., 2010, Lin et al., 2016b, Wen et al., 2024a). Although hydroxide precipitation can achieve high recovery of Mn, it has poor selectivity as it occurs at pH > 8.0, leading to the co-precipitation of Mg^{2+} and Ca^{2+} (Zhang et al., 2010). Oxidative precipitation uses toxic and corrosive gases like sulphur dioxide (SO_2) or sodium hypochlorite (NaClO) as a reducing agent with respect to Mn (Zhang and Cheng, 2007b). For this, very precise controls are required, which may increase the capital cost significantly, making the process unfeasible.

Sulphide precipitation requires pollution control and management, and the Mn sulphide is not a favourable product for the manganese industry, needing further conversion (Zhang and Cheng, 2007b, Tünay and Kabdaşli, 1994, Lewis, 2010). Carbonate precipitation has been shown to have fast kinetics, is cheaper, simple to do, and can achieve high Mn^{2+} selectivity over Mg^{2+} and Ca^{2+} (Pakarinen and Paatero, 2011, Zhang et al., 2010, Lin et al., 2016b, Muanda and Omalanga, 2021). Additionally, high selectivity occurs at low pH values between 5.0 and 7.0, requiring less reagent usage. Thus, carbonate precipitation of Mn was explored in this study to treat the $MnSO_4$ pregnant leach solutions.

Various carbonate precipitants are available for optimal precipitation efficiency. The use of sodium carbonate (Na_2CO_3) has shown that 98% of Mn^{2+} can be recovered from solutions (Zhang et al., 2010, Du et al., 2015, Muanda and Omalanga, 2021). However, it is expensive, and it introduces unwanted sodium ions that produce saline brines, which are expensive to discard. Limestone ($CaCO_3$) introduces unwanted Ca^{2+} ions and requires high pH values which leads to the co-precipitation Mg^{2+} (Silva et al., 2012, Aziz and Smith, 1992, Bamforth et al., 2006). This is because at low pH, $CaCO_3$ dissolves, and the carbonate ion is released as carbon dioxide gas (CO_2), and thus, no precipitation occurs. Ammonium bicarbonate (NH_4HCO_3) can achieve high Mn selectivity and recovery; however, it is expensive (Lin et al., 2016b, Ju et al., 2023, Hai et al., 2019). Precipitation using CO_2 offers a cheap and potentially environmentally friendly process for recovering Mn. This is because CO_2 is cheaper, readily available, and can achieve high recovery and selectivity. Therefore, this study aims to investigate the use of CO_2 to selectively recover Mn from an industrial $MnSO_4$ with Mg^{2+} and Ca^{2+}. Section 3.3 summarizes the use of CO_2 for different metal carbonates and explores strategies to optimize their processes.

3.2.2.1 The chemistry of manganese carbonate precipitation using CO_2

After the dissolution and speciation of CO_2 gas to form bicarbonate (HCO_3^-) and carbonate (CO_3^{2-}) ions (Equation (2-3) to (2-4)), these ions react with the dissolved metal ions (Me^{2+}) to form metal carbonates. This reaction mechanism is shown by Equation (3-10) and Equation (3-11):

$$Me^{2+}{}_{(aq)} + HCO_3{}^{-}{}_{(aq)} \rightleftharpoons MeCO_3{}_{(s)} + H^{+}{}_{(aq)} \quad (3\text{-}10)$$

$$Me^{2+}{}_{(aq)} + CO_3{}^{2-}{}_{(aq)} \rightleftharpoons MeCO_3{}_{(s)} \quad (3\text{-}11)$$

These reactions are only possible when supersaturation is achieved. The release of the proton (H^+) makes the reaction mixture acidic, which makes the control of pH during the precipitation process important to prevent the decrease in supersaturation that results in low Me^{2+} recovery.

3.3 The recovery of metal carbonates using CO_2 as a precipitant

The recovery of Mn, Mg, Ca, and lithium (Li) carbonates from solutions using CO_2 gas has been explored in various studies.

3.3.1 Manganese carbonate

Sibrell et al. (2007) used wastewater from the Palmerton zinc superfund site, which consisted of 56.4 mg/L Mn^{2+}, 372 mg/L Ca^{2+}, 353 mg/L Mg^{2+}, and 328 mg/L Zn^{2+}. The wastewater was first passed through a column filled with $CaCO_3$ and then bubbled with CO_2 gas for 2 h at the rate of 0.25 L/min. A co-precipitation of 42.2% Mn with 97.8% Zn was reported; however, neither the operating pH nor the co-precipitation of other metals (e.g., Mg^{2+} and Ca^{2+}) was reported, which is essential for assessing selectivity. On the other hand, Yu et al. (2019a) recovered more than 99% of Mn^{2+} from artificial wastewater from an electrolytic Mn plant, which consisted of 1.5 g/L Mn^{2+}, 1 g/L Mg^{2+}, and 0.5 g/L

Ca^{2+}. The CO_2 was bubbled at 0.5 L/min for 6 h, and the pH was 6.6. Also, in this study, the co-extraction of Mg^{2+} and Ca^{2+} were not reported. Furthermore, both studies omitted details about the CO_2 bubbling efficiency, which affects mass transfer and thus precipitation kinetics.

Wang et al. (2016) combined ammonia (NH_3) and CO_2 gas to recover $MnCO_3$ from a EMR leachate solution containing 2.87 g/L of Mn^{2+}. A maximum of 94.2% of Mn was recovered when CO_2 was bubbled for 2 minutes at 2 L/min, an NH_3:Mn^{2+} molar ratio of 3:1, and a final pH of 7.5. While this method was effective, the requirements of high ammonia dosage raise concerns about the economic viability and the secondary NH_3 pollution risk in wastewater, especially for large-scale operations. Additionally, the reported short CO_2 bubbling time seems rather inconsistent with the generally slow dissolution kinetics of CO_2 in aqueous media, which could challenge reproducibility. Furthermore, Chen et al. (2016) recovered 99.99% of Mn^{2+} from a EMR leachate that contained 7.14 g/L Mn^{2+} at pH > 11.5. The CO_2 was bubbled at 0.8 L/min for 20 minutes. However, Ca^{2+} and Mg^{2+} co-precipitated as dolomite. The high pH risks the occurrence of hydroxide precipitation (e.g., $Mg(OH)_2$ and $Ca(OH)_2$), complicating the $MnCO_3$ purity. All these studies highlight the dissolution of CO_2 and pH as the critical parameters, that longer bubbling times and high pH are required for higher Mn^{2+} recovery.

3.3.2 Other metal carbonates

Magnesium carbonate ($MgCO_3$) and calcium carbonate ($CaCO_3$) are co-precipitants in the context of $MnCO_3$ recovery. Teir et al. (2007) bubbled 1 L/min of CO_2 for 40 minutes to recover $MgCO_3$ from a 21 g/L Mg^{2+} leachate. At the pH of 9, maximum recovery of 94% Mg and highest purity was achieved. The co-precipitation of Mn^{2+} and Ca^{2+} was not reported. On the other hand, Zhu et al. (2017) investigated the absorption rate of CO_2 in a CO_2–$MgCl_2$–NH_3 system, and found that both the recovery of Mg^{2+} and CO_2 absorption rate were highest at pH > 9.0 after 4 h, indicating slow kinetics when NH_3 is involved. Chen et al. (2017) recovered Mg^{2+} from a Mg-Li-Cl brine composed of 50 g/L Mg^{2+} and 2.5 g/L Li^{+}. Under optimal conditions, a combination of 0.06 L/min of CO_2 and trioctylamine (TOA) was used to recover a maximum of 99% Li^{+} and 67.41% Mg^{2+} at parameters of TOA 50 vol%, organic to the aqueous ratio of 8, and pH of 9. These studies show that Mg^{2+} can be effectively precipitated using CO_2 at pH > 8, however, this overlaps with the $MnCO_3$ precipitation at pH between 7 to 8.5.

$CaCO_3$ is mostly recovered using CO_2 from alkaline solutions that are typically leached from steelmaking slag containing CaO (Andrade, 2020, Andrade and Sanjuán, 2018). Ji et al. (2024) bubbled 0.1 L/min of CO_2 for 1 h to recover $CaCO_3$ from a 6.0 g/L Ca^{2+} limewater. At pH > 7.0, more than 80% of Ca was recovered. Said et al. (2013) recovered 73% of Ca^{2+} when CO_2 was bubbled at 1.0 L/min for 1 h and pH > 8.0. In both studies, the co-precipitation of Mn^{2+} was not assessed, but they show that $CaCO_3$ precipitation is effective at pH > 7.0. Under these conditions, the Ca solubility is low and the absorption rate of CO_2 is high, thus, high recoveries are achieved in a short CO_2 bubbling time (Lívanský, 1982, Du, 2017). Within the first hour, the reaction rate is rapid but significantly slows down when CO_2 is bubbled for longer than 1 h.

Lithium carbonate (Li_2CO_3) is rather co-utilized with $MnCO_3$ to produce LiB. Han et al. (2020) bubbled 0.5 L/min of CO_2 for 102 minutes to recover Li_2CO_3 from a 20 g/L Li^+ synthetic sulphate solution. At a pH of 8.0, 45.5% of Li was recovered. Battaglia et al. (2022) on the other hand recovered Li_2CO_3 from an artificial brine solution containing about 4.0 g/L Li^+ after bubbling CO_2 at 0.075 L/min for 40 minutes. The solution also contained Ca^{2+}, Mg^{2+}, Mn^{2+}, Co^{2+}, and Ni^{2+} impurities. At a pH > 8.5, more than 63% of Li^+ was recovered. In addition, when the temperature was increased to 80°C, the recovery increased to 80% with a purity of 99%. Lastly, Ramírez Velázquez et al. (2024) recovered 79.5% of Li^+ from a 3.1 g/L Li^+ synthetic solution after bubbling CO_2 at 0.5 L/min for 30 minutes, and at pH > 9.0.

These studies show that it is feasible to use CO_2 as a carbonate precipitant, and that high recoveries can be achieved. Furthermore, they show that pH, CO_2 bubbling rate and bubbling time, and other factors have a significant effect on the efficiency of the process. The following section discusses critical factors that affect carbonate precipitation using CO_2 gas and the chosen factors for this study with their reasons.

3.4 Factors that affect the efficiency carbonate precipitation

In the recovery of Mn^{2+} from aqueous solutions using CO_2 gas, factors such as pH, CO_2 bubbling time, solid-liquid ratio, temperature, mixing intensity, and CO_2 partial pressure affect the precipitation efficiency of $MnCO_3$. The effect of these parameters is briefly presented and discussed below.

3.4.1 Effect of pH on manganese recovery and selectivity

The pH affects the absorption and speciation of CO_2, and also the solubilities of dissolved metals. The speciation of CO_2 affects the concentrations of HCO_3^- and CO_3^{2-} ions. At pH < 6.0, the dissociation of H_2CO_3 (aq) (Equation (2-3)) is limited due to the high concentration of H^+ ions. This leads to low concentrations of HCO_3^- and CO_3^{2-} ions, which would result in low Mn^{2+} recovery. As the pH increases to 8.0, the enhanced dissociation of H_2CO_3 (aq) leads to higher HCO_3^- and CO_3^{2-} concentrations, resulting in high Mn^{2+} recovery. Furthermore, an increase in pH results in lower metal solubilities. Therefore, high pH leads to a high degree of supersaturation due to the increase in the concentration of carbonate species and reduced Mn solubility, resulting in high precipitation rates and Mn^{2+} recovery.

Various studies have reported the effect of pH on the recovery and selectivity of Mn^{2+} in carbonate precipitation (Ma et al., 2013, Zhang et al., 2010, Xing et al., 2017, Lin et al., 2016b, Baumgartner and Groot, 2014, Muanda and Omalanga, 2021, Aziz and Smith, 1992, Ali et al., 2022). Thermodynamic simulations were carried by Ma et al. (2013) to predict the formed Mn species at pH values between 4 and 14 when using a combination of Na_2CO_3 and NH_3 to recover Mn from a synthetic $MnSO_4$ solution. It was found that $MnCO_3$ formed at a pH range of 4-8, a mixture of $MnCO_3$ and $Mn(OH)_2$ at pH 8-12, and $Mn(OH)_2$ at the pH range of 12-14. This suggests that for high Mn^{2+} selectivity, a pH < 8 is favourable. This is because, at pH > 8.0, metal hydroxides form instead of carbonates. Metal hydroxides are less selective because many other metal ions such as Ca^{2+} and Mg^{2+} co-precipitate as hydroxides at high pH. This leads to reduced purity of the recovered Mn^{2+}.

Zhang et al. (2010) investigated the precipitation of $MnCO_3$ and selectivity over Mg^{2+} and Ca^{2+} from a nickel laterite waste effluent at the pH range of 5.9-9.5. No precipitation occurred at pH < 6.0. This was also observed by Xing et al. (2017) when recovering Mn^{2+} from a synthetic manganese chloride tetrahydrate ($MnCl_2 \cdot 4H_2O$) using sodium bicarbonate ($NaHCO_3$). Both studies attributed this to the low supersaturation level as the low Mn^{2+} concentrations of less than 2.0 g/L used likely led and the carbonate sources were added stoichiometrically, in which this led to insufficient driving force for precipitation. These studies also failed to note that at pH < 6.0, the dissolved carbonates predominantly form H_2CO_3 rather than HCO_3^- and CO_3^{2-}, limiting $MnCO_3$ precipitation.

When the pH was increased to 7.5, the Mn^{2+} recovery increased to 2.00%, but also 1.43% and 0.99% of Mg^{2+} and Ca^{2+} co-precipitated, respectively. Similarly, Lin et al. (2016b) recovered 99.79% Mn^{2+}, 1.73% Mg^{2+}, and 6.36% Ca^{2+} at the pH range of 7.0-7.5 from a synthetic sulphate solution containing 14.6 g/L Mn^{2+}, 1.89 g/L Mg^{2+} and 1.54 g/L Ca^{2+} using NH_4HCO_3. This is probably because NH_4HCO_3 has a higher solubility compared to $NaHCO_3$ and, therefore, provides high amounts of carbonate ions for efficient precipitation. Zhang et al. (2010) reported < 2% Ca^{2+} co-precipitation at a pH of 7.5, while Lin et al. (2016b) observed 6.36% Ca^{2+} co-precipitation under similar pH. This suggests that a major anion (SO_4^{2-} vs Cl^-) may alter carbonate complexation. A further increase in pH to 9.5 led to 99.9% recovery of Mn^{2+}; however, this also co-precipitated 99.0% of Ca^{2+} and 91.9% of Mg^{2+} (Zhang et al., 2010).

Ying et al. (2017) recovered Mn^{2+} from wastewaters of a sewage treatment plant containing 1.4 g/L Mn^{2+}, 1.1 g/L Mg^{2+} and 0.47 g/L Ca^{2+} using a combination of CO_2 and CaO. At pH > 6.6, more than 99.79% of Mn^{2+} was recovered, however, more than 47% and 6.32% of Ca^{2+} and Mg^{2+} co-precipitated. Baumgartner and Groot (2014) extracted Mn^{2+} from a ferromanganese slag leach solution using $(NH_4)_2CO_3$ and Na_2CO_3. While both carbonate sources achieved high Mn^{2+} recoveries, exceeding 98.9% at pH > 8.5, significant co-precipitation of Mg^{2+} and Ca^{2+} was also observed. When Na_2CO_3 was used, Mg^{2+} and Ca^{2+} co-precipitation exceeded 94.8% and 80%, respectively, while $(NH_4)_2CO_3$ offered some improvement, co-precipitation remained substantial at 30.7% and 92.2% for Mg^{2+} and Ca^{2+}, respectively. Consequently, the resulting $MnCO_3$ precipitate contained more than 1% Ca, exceeding the threshold for battery-grade quality. However, the Mg content in the precipitate was not reported.

On the contrary, Ali et al. (2022) found that increasing the pH from 3 to 8 led to a reduced recovery of Mn^{2+} from 74% to 21%. This could be attributed to the excess Na^+ ions added from the Na_2CO_3 precipitant and NaOH for pH control. This likely led to Na^+ ions to react with HCO_3^- ions to form $NaHCO_3$, consuming the HCO_3^- ions that would otherwise react with Mn^{2+} to form $MnCO_3$, thus, reducing the Mn^{2+} recovery at higher pH values. This means that even though carbonate precipitation indicates that an increase in pH leads to increased Mn^{2+} recovery, the carbonate source matters. Therefore, because CO_2 does not form unwanted substances, its usage would increase Mn^{2+} recovery when pH is increased. The addition of NH_3 (aq) to control pH does introduce an impurity and poses nitrogen pollution, however, precise pH control would be done to reduce the usage of NH_3.

These studies show that high Mn^{2+} recoveries of more than 90% are feasible at pH > 7.5, but this leads to high co-precipitation of Mg^{2+} and Ca^{2+} (Muanda and Omalanga, 2021, Aziz and Smith, 1992). It is therefore suggested to operate in the pH range of 6.0-7.0 for high recovery and high selectivity of Mn^{2+}. This work aims to use CO_2 as the carbonate source to minimize cation competition

3.4.2 Effect of CO_2 bubbling time on the absorption efficiency

The inherently slow dissolution of CO_2 under atmospheric conditions, as highlighted by Ma et al. (2017), presents a significant supply limitation. Mulana et al. (2022) further demonstrated that the amount of CO_2 dissolved in water after 1 hour did not reach its solubility limit of 1.45 g/L. This limitation is amplified in the context of this study, where the high Mn^{2+} concentration creates a high demand for CO_2. To meet the carbonate demand for $MnCO_3$ precipitation, longer CO_2 bubbling times are required. Prolonged CO_2 bubbling increases the supply of HCO_3^- and CO_3^{2-} ions in the solution, promoting carbonate precipitation, thereby increasing Mn^{2+} recovery.

Increasing the CO_2 flowrate initially accelerates CO_2 rate of dissolution in solutions, leading to a higher supply of HCO_3^- and CO_3^{2-} ions for carbonate precipitation. However, at higher flowrates, the dissolution rate plateaus due to the gas-liquid mass transfer limitations and saturation of CO_2 solubility in the liquid phase. Studies by Aboudheir et al. (1998) and Park et al. (2004) observed increased absorption of CO_2 into monoethanolamine (MEA) solutions at lower gas flowrates, attributing this to the increased contact time between the gas and liquid phases, improving mass transfer. Although these studies focused on MEA, the principles of gas-liquid mass transfer and solubility constraints are broadly applicable to CO_2 dissolution in other aqueous solutions, such as $MnSO_4$. Higher flowrates initially enhance CO_2 absorption, but above 0.5 L/min, the reduced gas-liquid contact time reduces the amount of CO_2 that dissolves into the solution (Abdullah et al., 2023, Altiner, 2018). Furthermore, once the solubility limit of CO_2 is reached, no additional gas is absorbed, limiting the overall carbonate speciation and reducing the precipitation efficiency of $MnCO_3$.

Additionally, the CO_2 bubbling time significantly affects the Mn^{2+} recovery from solutions. Slower bubbling rates require longer bubbling times to achieve sufficient recoveries. Studies have shown that bubbling CO_2 exhibits an initially faster reaction rate, which slows down significantly after one hour (Andrade and Sanjuán, 2018, Andrade, 2020, Salmón et al., 2018, Tu et al., 2015, Masindi et al., 2023). This is particularly evident in alkaline solutions (pH > 10), where metal solubility is low, and the absorption rate of CO_2 is high, leading to high metal recovery (Lívanský, 1982, Du, 2017). However, longer CO_2 bubbling times can also lead to reduced supersaturation and slower precipitation rates due to the decreasing metal ion concentration (Abe et al., 2021). As a result, the rate of CO_2 conversion and the amount of CO_2 converted into metal carbonates decrease over time. These findings are based on studies using low concentration solutions. In high-concentration solutions, such as those in the current study, Mn^{2+} recovery may be slower due to the increased demand for HCO_3^- and CO_3^{2-} ions, which are essential for the carbonation process.

3.4.3 Effect of solid-liquid ratio on the efficiency of CO_2 dissolution and speciation

Another factor that may affect the speciation of carbonate species is the solid fraction, which increases the solid-liquid ratio (S/L). When bubbling CO_2 and forming $MnCO_3$, higher S/L: (i) reduces the stirring efficiency (at constant agitator speed) due to increased slurry viscosity, reducing gas-liquid interaction and CO_2 dissolution; and (ii) reduces the availability of H_2O molecules to react with CO_2 (aq), which reduces the formation of carbonate species. As a result of all these actions, the CO_2 dissolution and carbonate species production would be limited, resulting in lower Mn^{2+} recovery.

Studies by Eloneva et al. (2012) and Du et al. (2021) showed a decreased recovery of Ca^{2+} from steel slags when the S/L was increased from 20 to 100 g/L. Similarly, Dri et al. (2014) determined that an increase in S/L from 15 to 50 g/L decreases the amount of carbonate species that reacts with Ca^{2+}.

In contrast, Lee et al. (2012) found no evidence of a relationship between S/L and the recovery of Ca^{2+} from gypsum waste slurry. This is because the temperature of the reaction was observed to increase from 39 to 58°C as the S/L increased. Therefore, this enhanced reaction kinetics, which accelerated the carbonation reaction (Lee et al., 2012). These studies show that there is a potential limitation in the dissolution of CO_2 as the S/L increases. However, this may not be true in all systems as CO_2 dissolution is also influenced by variables such as temperature, solution composition, and agitation speed. Therefore, the effect of S/L may need to be studied for a $MnCO_3$ recovery process using CO_2, especially in terms of scaling up.

3.4.4 Effect of temperature on the recovery of metal carbonates

Temperature influences the solubility and reaction kinetics, and thus, the metal carbonate recovery. An increase in temperature generally leads to increased metal recovery (Muanda and Omalanga, 2021, Mwana et al., 2022). Korchef and Touaibi (2020) found that the recovery of Ca^{2+} using CO_2 increased from 73 to 85% when the temperature increased from 28 to 50°C. Similarly, Ali et al. (2022) found that increasing temperature to 60°C and 80°C improved $MnCO_3$ recovery, likely caused by the enhanced hydration and speciation of CO_2, increasing supersaturation. However, this led to the co-recovery of sodium, as excess Na^+ was used from the Na_2CO_3 precipitant and NaOH for pH control.

The increased recovery was likely caused by the enhanced hydration and speciation of CO_2, increasing supersaturation and precipitation rates. On the contrary, Lin et al. (2016b) determined that increasing the temperature from 25 to 40°C only slightly increased the Mn^{2+} recovery from 98.1% to 99.5%. Above 40°C led to reduced Mn^{2+} recovery, thus, 40°C provides optimal temperature for optimal recovery of $MnCO_3$. Furthermore, increase in temperature leads to reduced absorption capacity of CO_2, with high absorption at about 25°C (Gul and Tezcan Un, 2022, Lívanský, 1982). This shows a trade-off, while high temperatures may increase the carbonate precipitation kinetics, they also reduce the solubility of CO_2, potentially lowering carbonate ion availability. This means operating at 25°C would result in high $MnCO_3$ recovery as there would be a high CO_2 absorption.

3.4.5 Effect of mixing intensity and CO_2 partial pressure on the gas-liquid mass-transfer

High mixing intensity breaks down large CO_2 gas bubbles into smaller ones, increasing the interfacial area between gas and liquid. This enhances the CO_2 absorption, the rate of chemical reactions and supersaturation. Contreras Moreno et al. (2017) observed that the mass transfer coefficient of CO_2 remains constant at mixing speeds above 300 rpm. Similarly, Wang et al. (2016) reported that Mn^{2+} recovery stabilizes at mixing speeds above 190 rpm. In contrary, Ying et al. (2017) found that Mn^{2+} recovery remains constant at mixing speeds above 400 rpm, but this led to over 80% co-precipitation of Ca^{2+}. Therefore, for this study, a 500 rpm was selected to maximise the gas dispersion and mass transfer of CO_2 for high Mn^{2+} recovery during precipitation.

The CO_2 partial pressure (pCO_2) significantly influences the solubility of CO_2 and its rate of dissolution (Mulana et al., 2022, Butler, 2019). According to Henry's Law, higher pCO_2 increases the solubility of CO_2, leading to greater availability of carbonate species (HCO_3^- and CO_3^{2-}) in solution. High concentration of the carbonate species leads to an increased level of supersaturation, and hence an increase in precipitation rate of $MnCO_3$. Higher pCO_2 also enhances the gas-liquid mass-transfer, which improves the overall reaction kinetics and promotes efficient $MnCO_3$ precipitation.

However, the solubility of CO_2 is inherently limited even at excessively high pCO_2 levels, due to the system reaching saturation, beyond which no additional CO_2 is absorbed. Furthermore, high pCO_2 levels requires operating at high pressures requires, necessitating specialized equipment and higher capital costs due to the need for robust pressure-resistant reactors and safety measures. These additional costs can make the process uneconomical for large-scale industrial applications.

From all these parameters, the pH and CO_2 bubbling time are significant in the precipitation process when using CO_2. In the current study, longer bubbling times are required because of the high concentration Mn^{2+} solution used. All these studies were performed in open reactors, and thus, do not mention that a large portion of the CO_2 bubbled does not react but rather leaves the system in the atmosphere. Therefore, even though high flowrates seem to increase the absorption of CO_2, a lot more is lost. From this, it is suggested that CO_2 be bubbled at rates lower than 0.5 L/min. Therefore, the effect of pH and CO_2 bubbling time was investigated and reported in this work.

3.5 Research motivation and gap analysis

The selective recovery of Mn^{2+} from solutions containing Mg^{2+} and Ca^{2+} impurities has been successfully demonstrated using NH_4HCO_3 as a precipitant (Lin et al., 2016b). However, this has not been explored using CO_2 as an alternative precipitant. While the utilisation of CO_2 for the precipitation of Mn from dilute Mn^{2+} solutions ($Mn^{2+} < 5$ g/L) has been reported (Yu et al., 2019b, Wang et al., 2016, Hongliang et al., 2016), its application to solutions with high Mn^{2+} concentrations remains unexplored. In addition to this, the selectivity of Mn^{2+} over other impurities like Mg^{2+} and Ca^{2+} has not been studied when using CO_2.

Previous research has identified several factors affecting the efficiency of $MnCO_3$ precipitation when using CO_2, with pH and CO_2 bubbling time showing a significant influence. Research indicates that a pH range of 6.0-7.0 is optimal for achieving high Mn^{2+} recovery and selectivity. However, these findings are based on Mn^{2+} solutions with low concentrations (Mn^{2+} < 10 g/L), limiting their applicability to industrial solutions with higher Mn^{2+} concentrations (Mn^{2+} > 50 g/L). Furthermore, the effect of CO_2 bubbling time on Mn^{2+} recovery has not been thoroughly investigated, leaving a critical gap in understanding the process dynamics.

This study seeks to address these gaps by investigating the feasibility of producing high-purity $MnCO_3$ through bubbling CO_2 into an industrial $MnSO_4$ solution containing Mg^{2+} and Ca^{2+} impurities. Specifically, this study focused on the effect of pH and CO_2 bubbling time on the Mn^{2+} recovery and selectivity. The findings will contribute to the development of a sustainable and efficient process for recovering high-purity Mn^{2+} from industrial solutions, which is critical for supplying high-purity Mn for lithium-ion battery precursors.

3.6 Hypothesis and Research Questions

1) Increasing the pH value of the solution would improve the Mn^{2+} recovery during $MnCO_3$ precipitation using CO_2 gas. This is due to the increased dissolution of CO_2 which provides more HCO_3^- and CO_3^{2-} ions, and the decreasing solubilities of Mn^{2+}, Ca^{2+}, and Mg^{2+} at higher pH values increasing the supersaturation and, thus, increasing the precipitation rate and recovery. The following key questions will address the hypothesis:

    a) How does the increase in pH affect the recovery of Mn^{2+} compared to Ca^{2+} and Mg^{2+} ions in the precipitation process?
    b) How does the co-precipitation of Ca^{2+} and Mg^{2+} affect the overall purity and efficiency of Mn^{2+} recovery at higher pH values?
    c) Does the pH value affect the particle size distribution, morphology, and shape of the $MnCO_3$ particles?

The $MnSO_4$ pregnant leach solution required about 3.90 moles of dissolved CO_2 gas, however, the dissolution rate of CO_2 is slow. **Therefore, the effect of CO_2 bubbling time on the recovery and selectivity of Mn was investigated**. The overall research question was:

2) How much CO_2 bubbling time does the precipitation reaction require for a sufficient Mn^{2+} recovery? The key questions that will help to answer this research question are as follows.
    a) How does the increase in CO_2 bubbling time affect the recovery of Mn^{2+} in the precipitation process?
    b) How does extending the CO_2 bubbling time influence the rejection of Ca^{2+} and Mg^{2+} ions from the $MnCO_3$ precipitate?

c) How does the increasing CO_2 bubbling time affect the particle size distribution, morphology, and shape of the $MnCO_3$ particles?

4 MATERIALS AND METHODS

This chapter outlines thermodynamic models used for the simulations, the reagents and equipment used, the experimental procedures followed, and the analytical techniques employed in this study.

4.1 Research Approach

This study was divided into two investigations. Firstly, thermodynamic simulations were conducted to confirm the feasibility of selective precipitation of $MnCO_3$ from an industrial $MnSO_4$ pregnant leach solution that consists of Mg^{2+} and Ca^{2+} using carbon dioxide gas (CO_2) and then the identification of the operating pH conditions. Secondly, laboratory-scale experiments were performed at the identified conditions to validate the thermodynamic recovery and selectivity for Mn^{2+}. During the experiments, the effect of pH and CO_2 bubbling time were investigated.

4.2 Models for the thermodynamic simulations

Thermodynamic simulations investigated the effect of pH on the concentrations of carbonate species which affects the Mn^{2+} recovery, and solubility of dissolved metals (Mn^{2+}, Ca^{2+} and Mg^{2+}) which affects the Mn^{2+} selectivity. These simulations were conducted using OLI Studio: Stream Analyzer V.11.5.1.9™. The software employed the Mixed Solvent Electrolyte (MSE) framework using the revised Helgeson-Kirkham-Flowers (HKF) model for the calculation of standard thermodynamic properties of aqueous and solid species (OLI Systems Inc, 2024). The MSE framework is better suited for solvents with ionized salts as it is based on frameworks of Debye-Hückel-Pitzer, UNIQUAC, and ion interaction-virial expansion models that account for excess terms (OLI Systems Inc, 2017, OLI Systems Inc, 2021).

In the simulation, the pH was controlled using H_2SO_4 and potassium hydroxide (KOH) as the acidic and basic titrants, respectively. This is because H_2SO_4 dissociates into H^+ and SO_4^{2-}, and KOH dissociates into K^+ and OH^-. These ions do not complex with carbonate species to any significant degree.

4.3 Experimental Design

4.3.1 Reagents

The industrial $MnSO_4$ pregnant leach solution used in this study was sampled at two different times, three months apart. Feed 1 was used to investigate the effect of pH and feed 2 was used to investigate the impact of CO_2 bubbling time. Table 4.1 shows that the feed solutions consisted primarily of Mn^{2+} ions, with Mg^{2+}, Ca^{2+}, and Na^+ as the major impurities.

Table 4.1: The metal ion weight percentage in the industrial $MnSO_4$ pregnant leach solution (wt.%).

Feed	Mn	Mg	Ca	Na	B	Si	K	Pb	Sr
1	93.9	3.35	0.14	2.45	0.06	0.03	0.04	0.01	0.01
Uncertainty (±)	0.28	0.02	0.00	0.00	0.00	0.00	0.00	0.00	0.00
2	97.1	2.23	0.23	0.18	0.12	0.04	0.02	0.01	0.01
Uncertainty (±)	0.51	0.04	0.00	0.00	0.00	0.00	0.00	0.00	0.00

Analytical grade ammonia (NH_3, ≥ 28-30 wt.%) and manganese carbonate powder ($MnCO_3$, ≥ 99.9 wt.%) from Merck and Sigma-Aldrich, and instrument grade carbon dioxide (CO_2, ≥ 99.9 wt.%) from Air Products South Africa reagents were used throughout the experiments. De-ionized water (resistance ≥ 12 MΩcm) was used to prepare the saturated $MnCO_3$ solution.

4.3.2 Experimental set-up

All the experiments were carried out at 22-25°C, atmospheric pressure (1 atm), and in a 1.25 L continuously stirred tank glass reactor with a working volume of 1.0 L and equipped with four stainless steel baffles. The experimental setup used is shown in Figure 4.1.

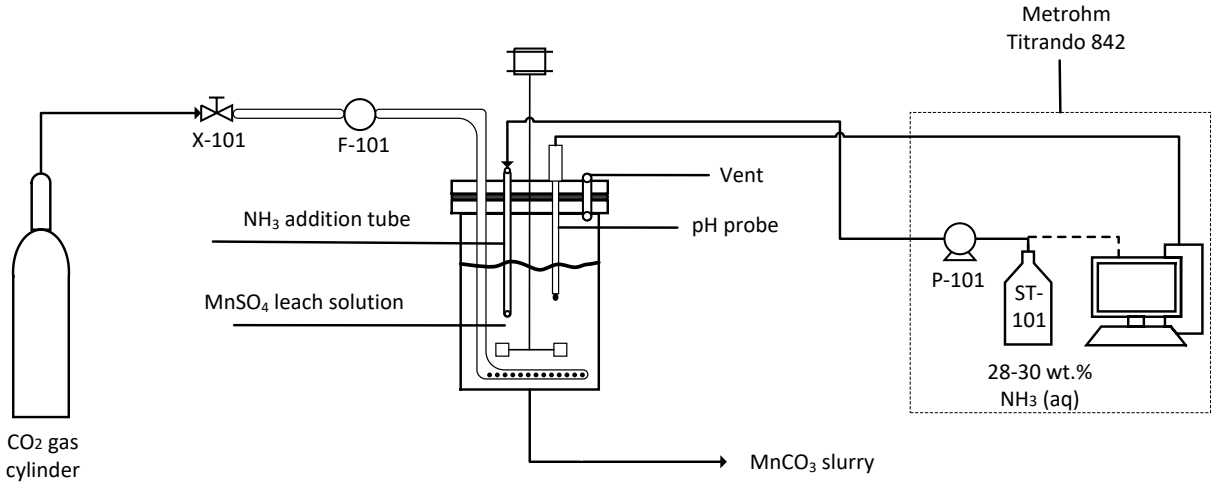

Figure 4.1: Experimental set-up used for precipitation.

The reactor head had 5 ports for the: CO_2 gas sparger; NH_3 dosage; overhead stirrer; pH probe; and gas vent. An IKA stirrer with a 6-bladed Rushton impeller and variable speed control was used to provide mixing. The CO_2 gas was bubbled into the reactor using a sparger system at 0.4 L/min, measured using the gas flow meter (F-101) (Dwyer Instruments, Inc, South Africa) that was calibrated for air and the flowrate was converted for CO_2 gas (Appendix A.1). The sparger system consisted of a ring sparger with a 66 mm inner diameter and 13 sparging orifices 14 mm apart around the ring, of 1.0 mm diameter each. The ring sparger was positioned directly below the impeller to ensure maximum gas-liquid mass transfer.

The Metrohm Titrando 842™ system (Metrohm AG, Switzerland) was used to measure the pH value and temperature of the solution with an accuracy of ± 0.01 and ± 0.01°C, respectively. This system consisted of a sulphide-resistant pH probe that measured and recorded every second, a 1 L bottle (ST-101) (Simax, Czech Republic) filled with NH_3 solution, and an NH_3 pump (P-101) (800 Dosino). The Tiamo™ version 3.0 software was used to control the pH value by controlling the NH_3 dosage. The pH probe was calibrated using Merck buffer solutions, with pH values of 4.01 and 7.01, prior to each experiment. The standard buffer solutions were replaced every two weeks.

4.3.3 Experimental matrix

The preliminary results performed at the pH of 6.6 showed that the bubbling CO_2 for 1 h resulted in less than 5% recovery of Mn^{2+}. This shows that the bubbling time of CO_2 has a significant effect on the Mn^{2+} recovery. Furthermore, the literature showed that high Mn^{2+} selectivity over Mg^{2+} and Ca^{2+} was achievable at pH < 7.0. Therefore, the effects of pH and CO_2 bubbling time were investigated in a range of 5.0 to 6.6 and 1 to 12 h, respectively, as outlined in Table 4.2.

Table 4.2: Experimental matrix.

Parameters	Independent variables	Controlled variables	Measured variables
Operating pH	Agitator speed = 500 rpm CO_2 flowrate = 0.4 L/min CO_2 bubbling time = 8 h	pH: 5.0 5.5 6.0 6.6	Volume of CO_2 gas bubbled. Mass of NH_3 added. Concentration of metals in filtrate Purity of precipitate
CO_2 bubbling time	Agitator speed = 500 rpm CO_2 flowrate = 0.4 L/min Operating pH = 6.6	CO_2 bubbling time (hours): 1 2 4 8 12	

The independent variables to investigate the effect of pH were chosen to ensure that sufficient CO_2 gas dissolved to provide the required HCO_3^- and CO_3^{2-} ions for precipitation. NH_3 (aq) was used to control the pH because the effluent $(NH_4)_2SO_4$ could be used in industries (Harris and Auerswald, 1977, Powlson and Dawson, 2022, Oishi et al., 2007).

4.4 Experimental Procedure

The feed solution was filtered twice using the Buchner funnel connected to a 2 L filtration flask and a nylon filter membrane with a pore size of 0.22 µm before it was used in experiments. The experiments were run using a semi-batch system, where first the reactor head was connected, and the reactor was charged with the double-filtered $MnSO_4$ feed solution. The pH probe was calibrated and connected to the reactor, after which stirring at 500 rpm commenced. The solution was mixed for 15 minutes or until the pH reading remained constant. Thereafter, CO_2 gas was bubbled into the system at 0.4 L/min for 1 h while measuring pH and not controlling it. This was to saturate the system with HCO_3^- and CO_3^{2-} ions. Finally, the NH_3 (aq) was automatically pumped to the reactor by the Titrando to control the pH at the desired value whilst bubbling CO_2.

After the reaction was completed, the reaction slurry was filtered using a Büchner funnel and nylon membrane filter with a pore size of 0.22 µm. The filter cake was dried in the oven at 35°C for 48 h to remove undissolved NH_3 (aq) and moisture. The dried precipitate was washed using a precipitate-to-saturated $MnCO_3$ solution mass ratio of 1:2.5. The saturated $MnCO_3$ solution used to wash the product was prepared as shown in Appendix A.2. The wash mixture was mixed for 20 minutes before it was

filtered. The wet precipitate was washed again using the same amount of saturated $MnCO_3$ solution two more times and filtered. Finally, the wet precipitate was dried at 35°C for 24 h. All the experiments were done in triplicates. The dried-washed precipitate was weighed and analysed using the analyses outlined in section 4.5.

4.5 Measurement techniques and Analysis Methods

4.5.1 Reagent amounts fed

The amount of CO_2 fed was calculated from the flowrate as follows:

$$\text{Volume of } CO_2 \text{ fed} = \text{flowrate} * \text{bubbling time} \quad (4\text{-}1)$$

The volume of the added NH_3 (aq) was taken from the Tiamo™ software and then converted to the mass of added NH_3 which can be seen in Appendix A.3.

4.5.2 Dissolved Metal Ion Concentration

Inductively coupled mass spectrometry (ICP-MS) was employed to measure dissolved metal ion concentrations in both feed and filtrate solutions. Additionally, the dry precipitate was dissolved in 2 wt.% nitric acid (HNO_3) to prepare a 1 g/L solution for ICP-MS analysis to quantify the precipitated metals.

4.5.3 Particle Size and Morphology Analysis

4.5.3.1 Particle Size Distribution (PSD)

The suspended precipitates were characterized for Particle Size Distribution (PSD) using the Malvern Mastersizer 2000 laser diffraction instrument within 15 minutes of the completion of each experiment. $MnCO_3$ saturated solution served as the dispersant medium within the Mastersizer, and the resulting PSD was expressed as a percentage volume distribution.

4.5.3.2 X-Ray Diffraction (XRD)

The washed precipitate was analyzed using X-Ray Diffraction (XRD) to identify the mineral composition of the precipitated metal carbonates. The XRD patterns obtained allowed for definitive confirmation of the mineral phase and morphology.

4.5.3.3 Scanning Electron Microscopy (SEM)

The crystal structure of the dry, unwashed precipitate was determined using Scanning Electron Microscopy (SEM) images. For complex structures, Energy-Dispersive X-ray Spectroscopy (SEM-EDS) was used to determine the elemental analysis of the structure.

4.6 Process efficiency analysis technique

4.6.1 Manganese recovery

Using ICP-MS results and Equation (4-2), the recovery of Mn^{2+} was calculated:

$$\text{Manganese recovery (\%)} = \frac{C_0V_0 - C_1V_1}{C_0V_0} \times 100 \quad (4\text{-}2)$$

where C_0 and C_1 are the concentrations (mg/L) of the manganese in solution, and V_0 and V_1 are the volumes (L) of the feed and residual solutions, respectively.

The Mn^{2+} recovery is divided into four categories, namely, experimental, expected, adjusted, and thermodynamic. **The experimental recovery referred to the** Mn^{2+} actually recovered over the duration of an experiment while **the expected** Mn^{2+} **recovery** was calculated assuming all bubbled CO_2 gas dissolved. **The Adjusted theoretical** Mn^{2+} **recovery** was calculated assuming that added NH_3 (aq) reflects the actual amount of CO_2 dissolved. **Thermodynamic recovery referred to** the Mn^{2+} recovery calculated assuming reaction reaches equilibrium.

4.6.2 Impurity rejection from the $MnCO_3$

The rejections of Mg^{2+} and Ca^{2+} from the $MnCO_3$ precipitate were determined using:

$$\text{Impurity rejection level (\%)} = \left(\frac{C_F V_1}{C_{0,\text{impurity}} V_0}\right) \times 100 \quad (4\text{-}3)$$

where $C_{0,\text{impurity}}$ is the concentration of Mg^{2+} or Ca^{2+} in the feed solution, and C_F is the concentration of Mg^{2+} or Ca^{2+} in the residual filtrate solution.

4.6.3 Purity of the $MnCO_3$

The purity of the washed $MnCO_3$ precipitate was determined using:

$$\text{Metal purity} = \frac{C_{\text{metal}}}{C_{\text{total}}} \times 100 \quad (4\text{-}4)$$

where C_{metal} is the concentration of Mn^{2+}, Mg^{2+}, or Ca^{2+}, and C_{total} the total concentration of all the dissolved metals in the washed precipitate.

5 RESULTS AND DISCUSSION

In this chapter, the findings from the thermodynamic simulations and laboratory experiments described in Chapter 4 are presented and discussed. The effect of pH and CO_2 bubbling time on Mn^{2+} recovery, rejection of impurities (Mg^{2+} and Ca^{2+}), $MnCO_3$ precipitate purity, and characteristics such as PSD, XRD analyses and morphology, are presented and discussed.

5.1 Thermodynamic simulation results

5.1.1 Effect of pH on CO_2 speciation

During the speciation of CO_2 gas, the concentration of the carbonate species (CO_2 (aq), HCO_3^-, and CO_3^{2-}) are strongly affected by the pH of the solution. Figure 5.1 shows the effect of pH on equilibrium log molar concentrations of dissolved carbonate, proton (H^+) and hydroxide (OH^-) ions in water across a pH range of 0-14 at a constant temperature and pressure of 25°C and 1 atm, respectively.

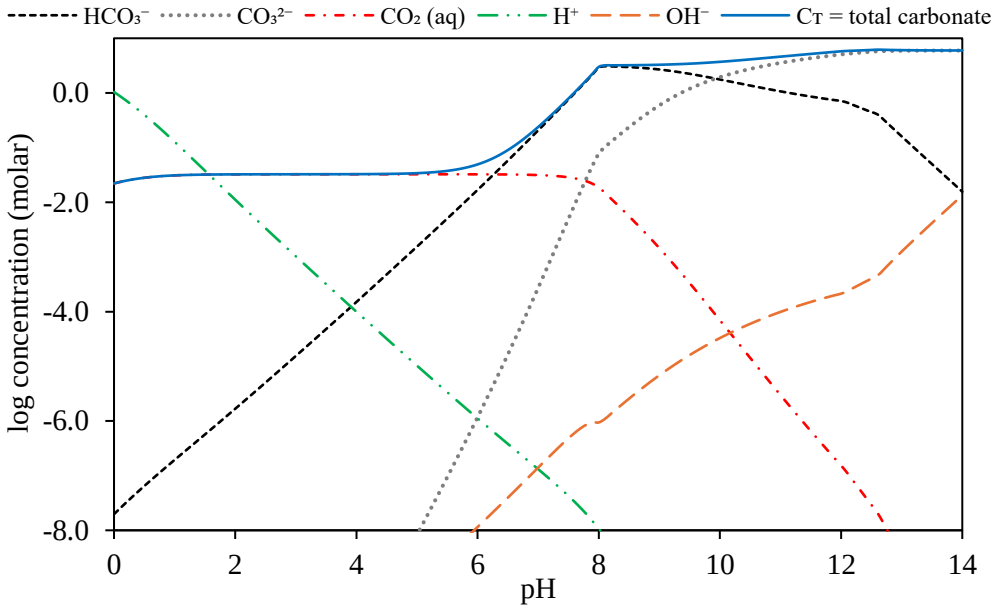

Figure 5.1: The thermodynamic effect of pH on the predicted molar concentrations of dissolved carbonate, H^+ and OH^- species in water at 25°C and 1 atm.

At pH < 5.0, total carbonate concentration (C_T) is approximately equal to the log molar concentration of CO_2 (aq), making it the dominant species. At this pH range, more than 95.5% of the Dissolved Inorganic Carbon (DIC) is present as CO_2 (aq), with about 4.5% of HCO_3^- ions present, and virtually no presence of CO_3^{2-} ions. As the pH increases to 7.0, the log molar concentration of HCO_3^- and CO_3^{2-} ions increases, and that of CO_2 (aq) remains constant. At pH > 6.5, HCO_3^- becomes the dominant species, and at pH between 7.0 and 8.0, the concentration of HCO_3^- is approximately equal to C_T. At this pH, 96.8% of DIC was present as HCO_3^-, 2.6% as CO_3^{2-}, and 0.6% as CO_2 (aq).

However, at pH > 8.0, the CO_2 (aq) and HCO_3^- concentrations decreases, while the concentration of CO_3^{2-} increases. Additionally, the concentration of H^+ decreases as the pH increases from 0.0 to 8.0, while the presence of OH^- ions begins from a pH of 6.0, and its concentration increases with increasing pH. Finally, at pH > 10, more than 52.5% of DIC was present as CO_3^{2-} and less than 47.5% as HCO_3^-, with virtually no CO_2 (aq).

The low concentrations of HCO_3^- and CO_3^{2-} ions at pH below 5.0 would be unfavourable for the recovery of Mn^{2+} due to the low supersaturation, leading to low recovery. The Mn^{2+} recovery would improve at the pH range of 5.0-8.0 due to the increased concentrations of HCO_3^- and CO_3^{2-} ions, which would increase the supersaturation and precipitation rate. In this range, small amounts of OH^- can react with CO_2 (aq) to form HCO_3^- (see Equation (2-5)). Maximum Mn^{2+} recovery would be achieved at pH > 8.0, where C_T is the highest, and this is consistent with $MnCO_3$ formation, as reported by Ma et al. (2013).

5.1.2 Effect of pH on the metal solubilities

The pH of the solution also affects the solubilities of the dissolved metals, which in turn influence their relative selectivity during precipitation. Figure 5.2 shows the effect of pH on the predicted equilibrium concentrations of Mn^{2+}, Ca^{2+} and Mg^{2+} in a sulphate solution at 25°C and 1 atm.

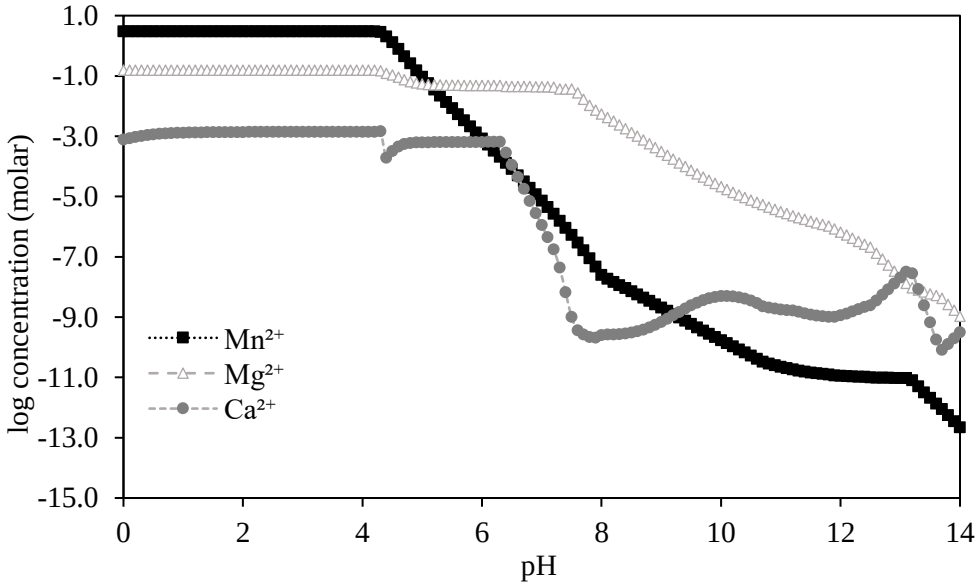

Figure 5.2: Effect of pH on the predicted equilibrium concentrations of the dissolved metal ions in the $MnSO_4$ solution at 25°C and 1 atm during carbonate precipitation (OLI Stream Analyser).

At pH values below 4.3, all three metals (Mn^{2+}, Ca^{2+} and Mg^{2+}) remain highly soluble due to the presence of H^+ ions from the dissociation of H_2CO_3 (aq), which is abundant. All these metals would begin to precipitate at the pH of 4.3, as shown by their decreasing concentrations. The concentration of Mn^{2+} decreases sharply between the pH of 4.3 and 7.4, indicating an increasing Mn^{2+} precipitation. Between the pH of 7.5 and 10.9, the rate of decrease in the concentration of Mn^{2+} is reduced, reaching a plateau between the pH of 11 and 13.1. Thereafter, it continues to decrease to lower levels which indicates that

precipitation would increase. The simulation predicts that Mn^{2+} would be recovered as only $MnCO_3$ between 4.3 and 13.1, and $Mn(OH)_2$ would only begin to precipitate at pH > 13.1. Therefore, a mixture of the two would be produced at pH > 13.1.

In the pH range between 4.3 and 6.3, the concentration of Ca^{2+} decreases slightly due to the slight precipitation of gypsum ($CaSO_4.2H_2O$), as shown by Yu et al. (2019c) and Rosenberg et al. (2012). When pH increases to 7.9, the concentration of Ca^{2+} decreases similarly to that of Mn^{2+}. However, the concentration of Ca^{2+} slightly increases at pH > 7.9, probably due to the increased solubility of $CaSO_4.2H_2O$ (Shukla et al., 2008). The concentration of Mg^{2+} slightly decreases when pH increases from 4.3 to 7.5 and continues to decrease above the pH of 7.5.

These observations highlight the critical role of pH in selectively separating Mn^{2+} from Ca^{2+} and Mg^{2+}. At pH < 6.6, both Mn^{2+} and Ca^{2+} can be recovered as $MnCO_3$ and gypsum. Because gypsum has a relatively high solubility in water, high-purity $MnCO_3$ would be formed when the product is washed. However, at this pH range, there are low equilibrium concentrations of HCO_3^- (< 0.035 mol/L) and even lower CO_3^{2-} (< $6x10^{-6}$ mol/L) ions. This would result in low supersaturation, leading to a lower precipitation rate and, thus, low Mn^{2+} recovery. Increasing the pH to 7.2 (and beyond) would enhance the Mn^{2+} recovery due to increased concentrations of HCO_3^- and CO_3^{2-} ions but would also lead to the co-precipitation of Ca^{2+} and Mg^{2+}.

These results indicate that it is thermodynamically possible to selectively precipitate Mn^{2+} from Mg^{2+} and Ca^{2+}. Furthermore, it is more favourable to separate Mn^{2+} from Mg^{2+} than from Ca^{2+}. A similar trend was observed by Lin et al. (2016b) when using thermodynamic simulations. From a thermodynamic perspective, high Mn^{2+} recovery is more favourable at a pH range of 6.0-8.0, but high selectivity is favourable at pH < 6. These results suggest that carbonate precipitation can achieve high Mn^{2+} selectivity, as reported by Zhang et al. (2010).

5.2 Experimental effect of pH on manganese recovery and selectivity

Figure 5.3 shows the effect of solution pH on the experimental Mn^{2+} recovery from the $MnSO_4$ pregnant leach solution, compared to the thermodynamic recovery predicted by OLI Stream Analyzer.

The experimental recovery of Mn^{2+} increased as the pH increased from 5.0 to 6.6. At the pH value of 5.0, 8.67% of Mn^{2+} was recovered. Increasing the pH to 5.5 and 6.0 resulted in an improved Mn^{2+} recovery of 16.4% and 28.6%, respectively. The recovery further increased to 39.6% when the pH was increased to 6.6. The thermodynamic simulations predicted significantly higher Mn^{2+} recoveries of more than 94% at pH values above 5.0. The observed difference in the experimental and predicted Mn^{2+} recoveries is thought to be due to the difference in the actual amounts of dissolved CO_2 gas in the solution.

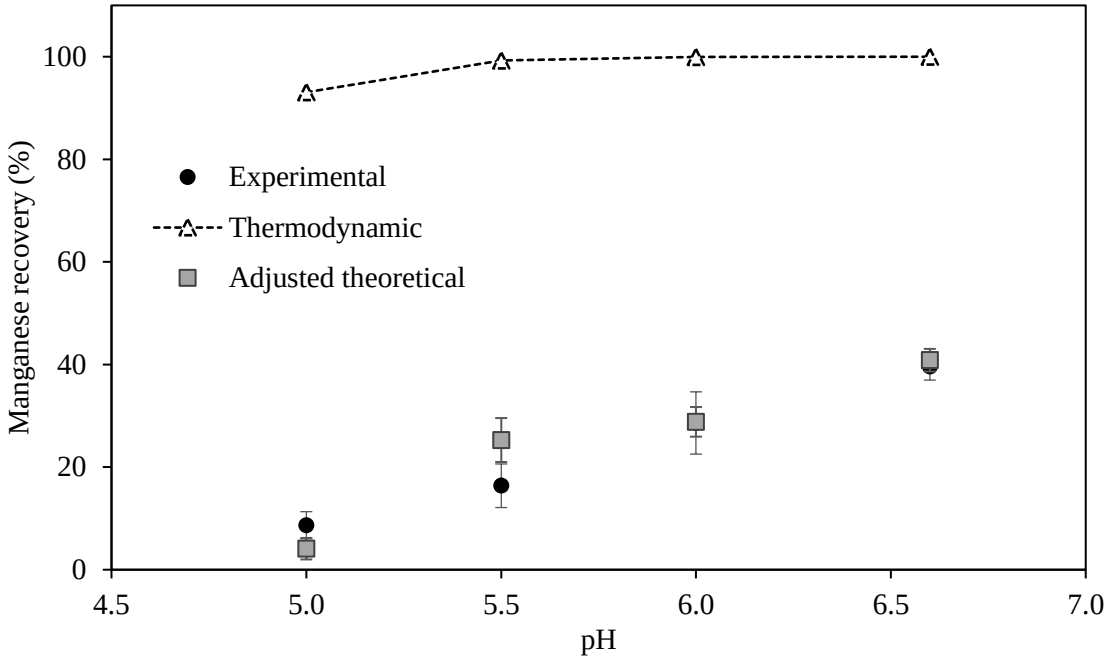

Figure 5.3: Effect of pH value on the Mn recovery compared to thermodynamic results.

Experimentally, a significant amount of CO_2 that was bubbled exited the reaction mixture without reacting. However, the thermodynamic model assumed that equilibrium was reached. The fast rise velocity of the gas bubbles reduced the gas-liquid contact time, which allowed a substantial portion of the bubbled CO_2 to exit the system through the vent. The impact of CO_2 transfer inefficiency was experimentally confirmed through the observed added amount of NH_3. Higher CO_2 absorption into the solution required more NH_3 to adjust the pH. At a pH of 5.0, for example, 96.5 g of NH_3 was thermodynamically required, yet only 2.02 g of NH_3 was experimentally added (see Appendix A.3), suggesting that most of the bubbled CO_2 into the reaction mixture exited without reacting, thus, there was low availability of HCO_3^- and CO_3^{2-} ions.

To better align the experimental results with thermodynamic predictions, the Mn^{2+} recovery was recalculated (with the use of OLI Analyzer) using the actual amounts of bubbled CO_2 gas and NH_3 added during the experiments. These adjusted Mn^{2+} recoveries (see the adjusted theoretical Mn^{2+} recovery in Figure 5.3) closely matched the observed experimental recoveries, which confirms that CO_2 loss was a key factor limiting the Mn^{2+} recovery. From this, it is recommended that future investigations consider optimising the reactor design for enhanced CO_2 absorption.

The increased Mn^{2+} recovery with increasing pH can be primarily attributed to the increase in the concentration of carbonate species (HCO_3^- and CO_3^{2-}) and the decrease in Mn solubility. The higher concentration of carbonate species results from the increased CO_2 absorption rate and enhanced dissociation of H_2CO_3 (aq). The absorption rate of CO_2 increases with pH because the addition of NH_3 solution introduces OH^- ions which react with H^+ ions, forming water (H_2O). As a result, the removal of H^+ ions shifts the equilibrium towards the dissociation of H_2CO_3 (aq) to form more H^+ ions and

enhancing CO_2 absorption. The combined increased concentration of carbonate species and reduced Mn solubility significantly increases the degree of supersaturation, which promotes a higher precipitation rate, thus, increases the recovery.

Zhang et al. (2010) and Xing et al. (2017) recovered Mn^{2+} from solutions containing 2.0 g/L and 0.018 mg/L of Mn^{2+} using Na_2CO_3 and $NaHCO_3$, respectively. Both studies reported no $MnCO_3$ precipitation at pH < 6.0. This contrasts with the findings of the current study, where $MnCO_3$ precipitation occurred even at the pH of 5.0, with recovery increasing to 28.6% at the pH of 6.0. The observed discrepancy can be attributed to differences in supersaturation level, as the lower Mn^{2+} concentrations in the referenced studies likely resulted in insufficient driving force for precipitation. When simulating the solutions in these papers on OLI Stream Analyzer, more than 89% of Mn^{2+} is predicted to precipitate at the pH of 5.9. Notably, these studies did not report their precipitation times, which may suggest that insufficient reaction durations may have contributed to the lack of observed precipitation. The recovery of 28.6% Mn^{2+} at a pH of 6.0 is consistent with the results reported by Funes et al. (2014), where less than 20% of Mn^{2+} was recovered from a 1.0 g/L Mn^{2+} solution using $NaHCO_3$. This was because the molar ratio of carbonate species to Mn^{2+} was more than 60 and reaction was conducted for 24 hours, thus, sufficient supersaturation was reached.

Other studies also reported the trend of increasing Mn^{2+} recovery with increasing pH (Shu et al., 2019, Xing et al., 2017, Zhang et al., 2010, Muanda and Omalanga, 2021). These studies showed that a pH > 8.0 results in the efficient Mn^{2+} recovery of more than 90%. Similarly, Korchef and Touaibi (2020) observed that the increase in the initial pH of Ca^{2+} solutions led to an increased supersaturation, which resulted in the increased precipitation rate of $CaCO_3$ and improved recovery. However, Ali et al. (2022) reported a decrease in Mn^{2+} recovery with increasing pH from 3 to 8, contrasting the findings of this present study. The decreasing Mn^{2+} recovery was attributed to the increasing concentration of Na^+ ions, which reacted with HCO_3^- ions to form $NaHCO_3$. This reaction consumed the HCO_3^- ions that would otherwise provide the carbonate ions for $MnCO_3$ precipitation, reducing the Mn^{2+} recovery at higher pH values.

These results show that the pH value affects the recovery of Mn^{2+} during precipitation. Furthermore, they validate the hypothesis that increasing the pH value from 5.0 to 6.6 increases Mn^{2+} recovery. However, these findings also show that operating at pH < 6.6 results in Mn^{2+} recovery of less than 40% due to poor dissolution of CO_2.

Therefore, it is recommended to investigate pH values greater than 6.6 for an improved CO_2 dissolution and, thus, an improved Mn^{2+} recovery from industrial $MnSO_4$ leachates when using CO_2 as a carbonate source. Additionally, the dissolution of CO_2 should be improved by investigating the use of nanobubbles, which have a higher surface area-to-volume ratio, or by increasing the gas-liquid contact time by using a taller reactor, or by using a pressured and closed reactor to ensure the bubbled CO_2 does

not exit the system but rather is dissolved and converted to carbonate species, thus, increasing the Mn^{2+} recovery.

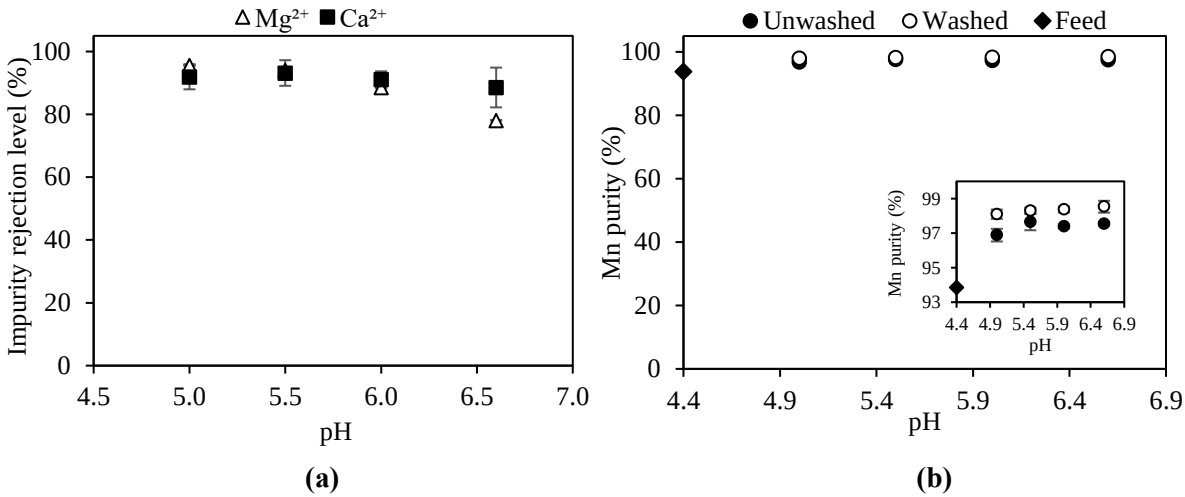

Figure 5.4: Effect of pH on the: (a) Mg^{2+} and Ca^{2+} impurity rejection levels; (b) purity of $MnCO_3$ precipitate during precipitation.

Figure 5.4(a) shows that as the pH increased from 5.0 to 6.0, the rejection of Mg^{2+} slightly decreased from 95.6 to 88.5%, while the rejection of Ca^{2+} was relatively constant at about 92%. A further increase in pH to 6.6 led to a slightly reduced rejection of Mg^{2+} and Ca^{2+} to 78.1 and 88.5 wt.%, respectively. As the pH increased, the total carbonate concentration increased and the solubilities of Ca^{2+} and Mg^{2+} impurities decreased (see Figure 5.1 and Figure 5.2) which ultimately led to levels that promoted their supersaturation. At these conditions, these impurities likely co-precipitated together as dolomite ($CaMg(CO_3)_2$) (Han et al., 2022, Gao et al., 2024, Hobbs et al., 2024, Deocampo, 2010).

Furthermore, as the pH increased from 5.0 to 6.6, the Mn purity of the unwashed $MnCO_3$ slightly increased from 96.9 to 97.6 wt.%. This is an improved purity from 93.9 wt.% in the feed solution at a pH of 4.4. The large error bars indicate that purity remained statistically constant at pH > 5.5. The preliminary results showed that the entrainment of the residual solution during filtration was significant, hence washing was required. The purity of the washed $MnCO_3$ precipitate was slightly higher than that of the unwashed. The Mn purity in the washed precipitate statistically remained constant at 98.5 wt.% as the pH increased from 5.0 to 6.6, comparable to the 99.7 wt.% of the Merck product.

Although the rejection of Mg^{2+} slightly decreased when the pH increased, washing the $MnCO_3$ precipitate showed a decreased Mg^{2+} content. This means the Mg^{2+} was entrained from the residual solution because its solubility is high at pH < 6.6. On the other hand, the Ca^{2+} content remained constant during the washing stage, suggesting that Ca^{2+} co-precipitated as $CaCO_3$ with $MnCO_3$. This is because its solubility is closer to that of Mn^{2+} at this pH range. This means $CaMg(CO_3)_2$ was not formed and that the rejection of Ca^{2+} and Mg^{2+} follows thermodynamic predictions that Mg^{2+} is rejected more than Ca^{2+}.

Based on these findings, it is recommended to maintain a pH < 6.6 to reject most of the Mg^{2+} and Ca^{2+} ions from the $MnCO_3$ precipitate. Furthermore, the results show that CO_2 gas and NH_3 (aq) can be used to recover high-purity $MnCO_3$ from industrial $MnSO_4$ leach solutions. Lastly, the pH range of 5.0 to 6.6 does not have a significant effect on the purity of the $MnCO_3$ precipitate produced when using a feed solution with high Mn to Mg ratio.

5.2.1 Effect of pH on the PSD, morphology, and shape of $MnCO_3$ particles

5.2.1.1 Particle Size Distribution

The PSD in Figure 5.5 shows that the $MnCO_3$ particles had a narrow distribution, and the average median particle size (d_{50}) varied between 3.2 and 4.4 µm as the pH increased from 5.0 to 6.6. Increasing the pH from 5.0 to 6.6 increased the modal size of $MnCO_3$ particles from 3.8 to 5.01 µm. These modal sizes suggest that the supersaturation was relatively constant which led to the formation of similar and smaller particle sizes. This means the nucleation rate was promoted and the growth rate was limited, as a result, a narrow distribution was produced. A narrow PSD indicates uniform particle size, which is beneficial for applications requiring uniform material properties.

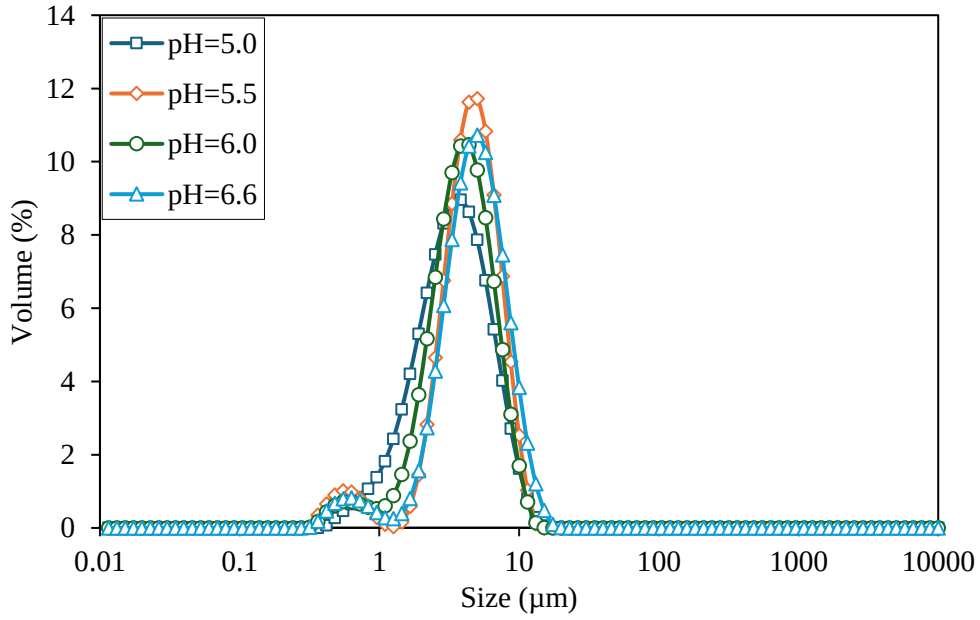

Figure 5.5: Effect of pH on $MnCO_3$ particle size distribution of the precipitate.

These results could explain the similar Mn purities observed at pH values between 5.0 to 6.6, which may be attributed to the similar particle sizes. This similarity suggests that the extent of the entrainment of the residual solution and the slight co-precipitation of Ca^{2+} were similar at all the tested pH values. Furthermore, they show that the pH range of 5.0-6.6 does not significantly affect the particle size of the produced $MnCO_3$. This could probably be because the dissolution rate of CO_2 gas does not significantly change between pH 5.0 and 6.6, which means the supersaturation relatively does not change.

5.2.1.2 XRD of $MnCO_3$ particles

The XRD pattern of the $MnCO_3$ precipitate recovered at pH values from 5.0 to 6.6 is shown in Figure 5.6. The formed $MnCO_3$ precipitates showed similar characteristic diffraction peaks at 28.21°, 36.60°, 43.85°, 48.49°, 52.88°, and 60.77° compared to the Merck product. These peaks confirm the formation of high-purity $MnCO_3$ with a rhombohedral crystal structure and no detectable secondary phases.

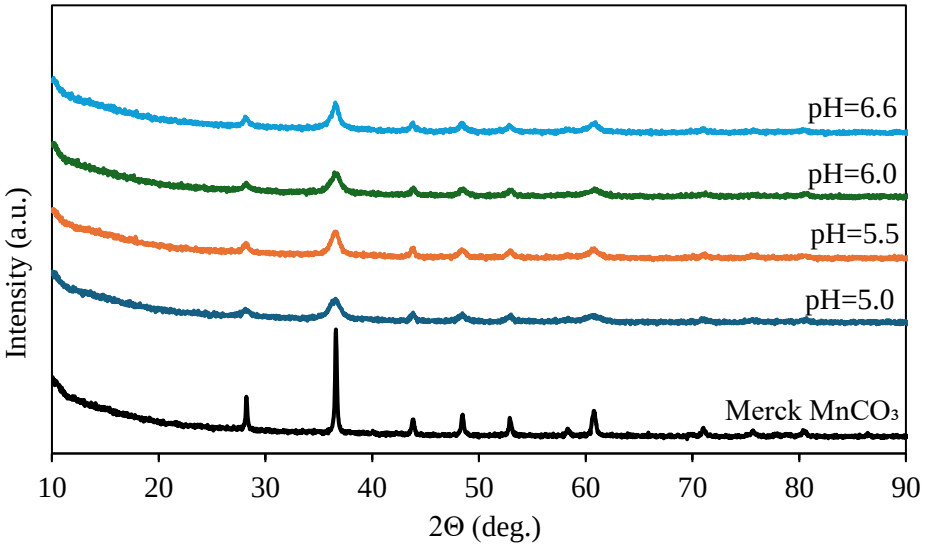

Figure 5.6: XRD patterns of obtained $MnCO_3$ precipitate at pH values from 5.0 to 6.6.

The increase in pH from 5.0 to 6.6 resulted in an insignificant change in the intensity of the diffraction peaks, which means this pH range does not change the phase or structure of the produced $MnCO_3$ precipitate. Although the XRD peaks show high-purity $MnCO_3$, the relatively low intensity of the diffraction peaks show that the $MnCO_3$ particles were predominantly amorphous or lacked long-range crystallinity.

5.2.1.3 SEM Images of $MnCO_3$ particles

The morphology of the $MnCO_3$ precipitate at varying pH values between 5.0 and 6.6 is shown by the SEM images in Figure 5.7.

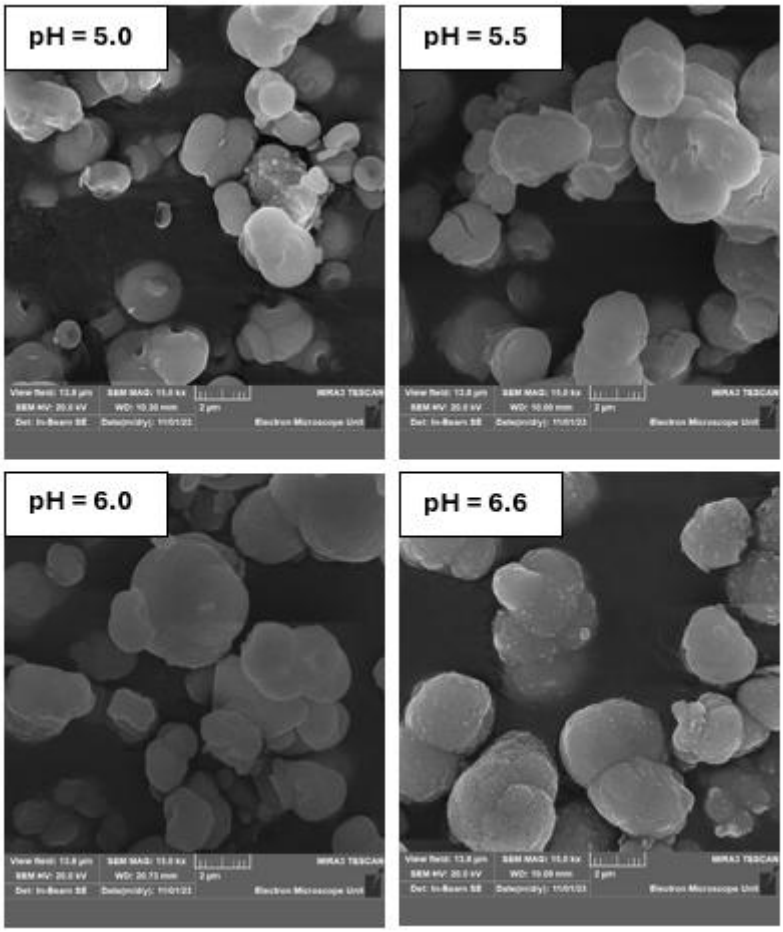

Figure 5.7: SEM images of $MnCO_3$ precipitated at different pH values.

At the pH of 5.0, the synthesized $MnCO_3$ were composed of ring-shaped structures with average sizes between 1.0 and 2.0 µm. As the pH increased to 6.6, these structures agglomerated, forming a cluster of spherical particles that were larger in size. These particles are comparable with those produced by Huang et al. (2015) who found that at pH between 6.5 and 7.5, spherical $MnCO_3$ with a rough surface was formed from compactly stacked, flake-like primary particles. However, Garcia et al. (2020) showed that rhombohedral and cubic $MnCO_3$ particles are prone to form from solutions with low Mn^{2+} concentration ($Mn^{2+} < 12x10^{-3}$ mol/L).

These findings suggest that pH and Mn^{2+} concentration affect the morphology of $MnCO_3$ particles, with high Mn^{2+} concentration promoting spherical particle formation. However, while pH influences the degree of agglomeration, it does not significantly affect the morphology of the particles.

5.3 Effect of CO_2 bubbling time on manganese recovery and selectivity

The thermodynamic simulations indicated that high recovery and high selectivity of Mn^{2+} can be achieved using CO_2 as a precipitant at a pH of 6.6. A stoichiometric amount of about 93 L (=3.87 moles) of CO_2 is required for complete precipitation of Mn^{2+}. However, the maximum CO_2 flowrate in the current setup was 0.4 L/min, which means that at least 4 hours of bubbling CO_2 is required to achieve

the complete recovery of Mn^{2+} when assuming perfect dissolution of CO_2. Therefore, the effect of CO_2 bubbling time on Mn^{2+} recovery and selectivity was investigated. The CO_2 was bubbled for 1 to 12 h at a pH of 6.6. Figure 5.8 shows the effect of CO_2 bubbling time on the Mn^{2+} recovery from the $MnSO_4$ pregnant leach solution.

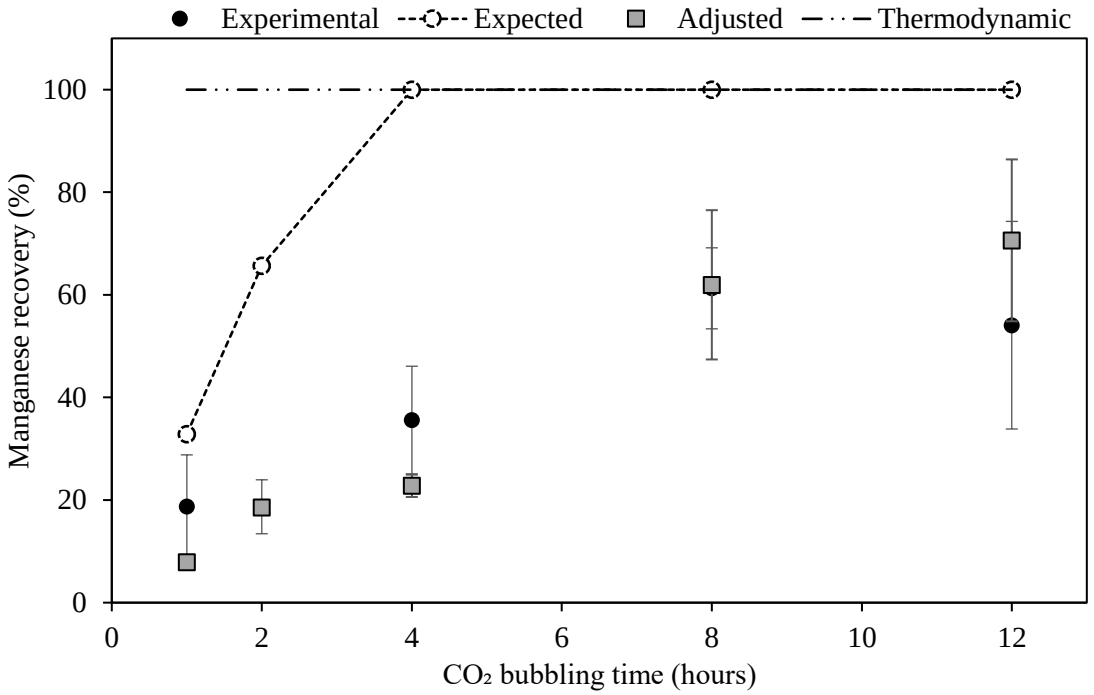

Figure 5.8: Effect of CO_2 bubbling time on the Mn^{2+} recovery.

Experimental results show that bubbling CO_2 for 1 and 2 h led to the same Mn^{2+} recovery of 18.7%. Increasing the CO_2 bubbling time to 4 and 8 h improved Mn^{2+} recovery to 35.6 and 61.3%, respectively. A further increase in the CO_2 bubbling time to 12 h led to a statistically constant Mn^{2+} recovery. Nonetheless, the increasing recovery over the first 8 h shows that prolonged bubbling of CO_2 is required for higher Mn^{2+} recovery, indicating that CO_2 is the limit reagent in the precipitation reaction under the experimental conditions.

The expected Mn^{2+} recovery was higher than the experimental values because it assumed that all the supplied CO_2 dissolved. The thermodynamic simulation predicted almost 100% Mn^{2+} recovery because it assumed equilibrium was reached. However, during the experiments, a large amount of CO_2 exited into the atmosphere due to the: (i) high bubble rise velocity and short reactor height which reduced the gas-liquid contact time; (ii) slow CO_2 dissolution rate that limited the absorption of CO_2; and (iii) the open vent of the reactor which led to the loss of unreacted CO_2. The combination of these factors limited the overall mass-transfer of CO_2 into the solution, reducing the availability of HCO_3^- and CO_3^{2-} ions, thereby resulting in significantly lower Mn^{2+} recovery than the predicted values. However, the individual contribution of these factors to the overall mass-transfer could not be investigated further as it was not the aim of this study.

Nevertheless, the inherently slow CO_2 dissolution rate has been highlighted previously by Ma et al. (2017) and Mulana et al. (2022), possibly played a major role in the low Mn^{2+} recovery. This slow dissolution rate led to a slow formation of HCO_3^- and CO_3^{2-} ions. Although the precipitation of $MnCO_3$ occurs spontaneously due to a low activation energy, the slow formation of carbonate species led to low supersaturation, and thus slow precipitation rate of $MnCO_3$ (Du et al., 2015). The potential increase in the dissolution of CO_2 due to its simultaneous dissolution and chemical reaction did not appear to significantly have increased the overall mass transfer rate in the setup used. This is because the short contact-time between the gas and liquid limited the mass-transfer.

The adjusted Mn^{2+} recovery was recalculated using the amounts of NH_3 (aq) added into the solution during the experiment. The small differences between the adjusted and experimental recoveries indicate they are not statistically different.

The reaction was expected to reach equilibrium after 4 h of bubbling CO_2. However, even after bubbling CO_2 for 12 h, the reaction still had not reached equilibrium. This is evidence that the CO_2 dissolution rate is slow under the operating conditions. Additionally, the concentrated pregnant leach solution used in this study required approximately 3.90 moles of dissolved CO_2 for complete Mn^{2+} precipitation, creating a high CO_2 demand that further constrained recovery. Therefore, the slow dissolution rate and subsequent loss of CO_2 explains why Mn^{2+} recovery was below the expected recoveries.

The maximum Mn^{2+} recovery from the precipitation process reached after 8 h of CO_2 bubbling time can be attributed to operational challenges and increased solid-liquid (S/L) ratio.

The operational challenges include sparger blockage and coating of the pH probe. The sparger blockage by $MnCO_3$ precipitate reduced the number of the available sparger holes in which CO_2 was supplied, increasing the gas rise velocity, thus further reducing the contact-time for the dissolution of CO_2. This limited the formation of HCO_3^- and CO_3^{2-} ions, thus slowing $MnCO_3$ precipitation, and hence, no further increase in Mn^{2+} recovery.

Additionally, it was observed that the pH probe was coated with the precipitate when operating for 8 h and became severe at 12 h of bubbling time. This coating likely disrupted the pH control as seen by the large variation in the added NH_3 (aq) (see Figure A.1 in Appendix A.3). Therefore, CO_2 dissolution varied greatly, resulting in high variation in Mn^{2+} recovery. In addition to coating, the large error bars in the experimental Mn^{2+} recovery were likely caused by the detection challenges using ICP-MS. This technique is more accurate for Mn^{2+} concentrations in the range between 0.002 mg/L to 5 g/L (Tyler and Yvon, 2003). However, the filtrate solution exceeded 50 g/L of Mn^{2+} ions in the present study. Therefore, it is recommended to use other analysis methods like atomic absorption technique (AAS) or potentiometric titration using permanganate ion to measure the high Mn^{2+} concentrations with high accuracy (Tyler and Yvon, 2003, Lingane and Karplus, 1946, Verdingh, 1981).

The Mn^{2+} recovery could also have been affected by the increase of the S/L ratio in the reactor over time since this is a semi-batch system. Higher S/L weakens the stirring force (since the mixing stirrer speed was constant), reduces gas-liquid interaction, and increases the viscosity of the solution, which all these limits the CO_2 dissolution and the production of carbonate species, resulting in lower Mn^{2+} recovery. It also reduces the mass transfer efficiency between the liquid and solid phases which lowers the precipitation rate (Chiang and Pan, 2017). The limited Mn^{2+} recovery with increasing S/L is similar to other studies on Ca^{2+} recovery from steel slags (Eloneva et al., 2012, Du et al., 2021, Dri et al., 2014). In contrast, Lee et al. (2012) did not observe any effect of S/L on the recovery of Ca from gypsum waste.

Finally, the decreased concentration of Mn^{2+} ions as the $MnCO_3$ precipitated led to a reduced supersaturation (as shown by Equation (2-11)), reducing the rate of $MnCO_3$ precipitation after 8 h and leading to low recovery of Mn^{2+}. Therefore, all these mechanisms collectively contributed to the statistically constant Mn^{2+} recovery when bubbling CO_2 for more than 8 h. The increased Mn^{2+} recovery with increasing CO_2 bubbling time observed in this study is consistent with other studies (Schütz et al., 2011, Tu et al., 2015, Yu et al., 2019a, Abe et al., 2021, Masindi et al., 2023).

The results from the current study show that CO_2 must be bubbled for a prolonged time to achieve higher Mn^{2+} recovery, and optimal recovery was achieved after bubbling CO_2 for 8 h. Bubbling longer than 8 h leads to operation challenges which result in no significant change in Mn^{2+} recovery.

Add a connecting sentence!

Figure 5.9 shows the effect of CO_2 bubbling time from 1 to 12 h on the rejection of Mg^{2+} and Ca^{2+} and the corresponding purity of the $MnCO_3$ precipitate.

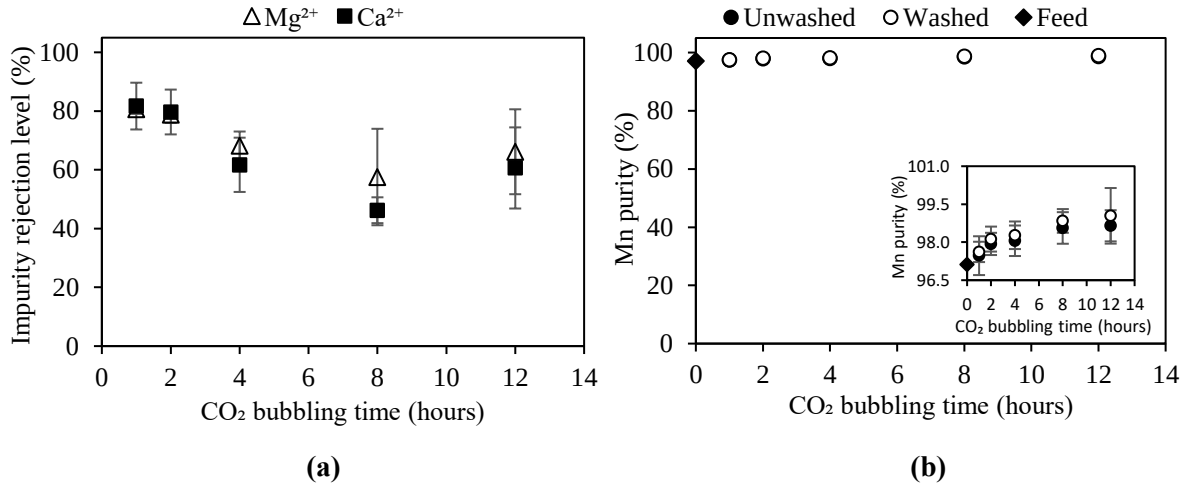

Figure 5.9: Effect of CO_2 bubbling time on the Mg^{2+} and Ca^{2+} impurity rejection levels.

Figure 5.9(a) shows that bubbling CO_2 for 1 and 2 h resulted in relatively similar rejections of 80.6% and 78.8% for Mg^{2+} and 81.7% and 79.7% for Ca^{2+}, respectively. As the CO_2 bubbling time was increased to 4 h, the rejection of Mg^{2+} decreased to 68.2% and levelled off at 57.6% after 8 h of bubbling CO_2. Likewise, the rejection of Ca^{2+} decreased to 61.7% and 46.3% as the CO_2 bubbling time increased

to 4 and 8 h, respectively. However, bubbling CO_2 for 12 h led to statistically insignificant changes in the rejection levels of Mg^{2+} and Ca^{2+} impurities, thus bubbling CO_2 for 8 h leads to lowest impurity rejections.

The decreased rejection levels of Mg^{2+} and Ca^{2+} with longer CO_2 bubbling time can be attributed to the reduced ionic activity of Mn^{2+} as $MnCO_3$ is continuously precipitated, thereby decreasing its supersaturation. This led to the enhanced ionic activities and supersaturation of Mg^{2+} and Ca^{2+}, leading to their co-precipitation. A similar trend was reported by Lin et al. (2016b), where the co-precipitation rates of Ca^{2+} and Mg^{2+} gradually increased when operating for longer than 4 h using NH_4HCO_3.

The rejection of Ca^{2+} was less pronounced than that of Mg^{2+} because $CaCO_3$ has a lower solubility (K_{SP}) than $MgCO_3$. However, the presence of Mg^{2+} reduced the precipitation rate of $CaCO_3$. With a high Mg^{2+}/Ca^{2+} molar ratio of more than 2, Mg^{2+} and Ca^{2+} likely co-precipitated as $CaMg(CO_3)_2$ (Liu et al., 2019). The presence of Mg^{2+} and Ca^{2+} ions impurities competed with Mn^{2+} ions during the nucleation process. When these impurities are absorbed into $MnCO_3$ nucleation sites, they increase the energy barrier for $MnCO_3$ nucleation (Loewenthal and Maais Gv, 1977). Specifically, Mg^{2+} ions are attached to kink sites on the $MnCO_3$ crystal surface, inhibiting the attachment of carbonate ions, and thus slowing the precipitation process. In contrast, the Ca^{2+} ions subtly altered the growth dynamics and morphology of $MnCO_3$ crystals (Mills et al., 2022).

Figure 5.9(b) shows that the purity of the unwashed $MnCO_3$ increased from 97.5 to 98.6 wt.% with increasing bubbling time from 1 to 12 h, exceeding the initial 97.1 wt.% Mn^{2+} purity in the feed solution. This increase contradicts the decreasing impurity rejection levels (see Figure 5.9(a)), which would typically lead to lower $MnCO_3$ purity. The likely cause for this could be attributed to the entrainment of the residual feed solution, which, because it had a high Mn^{2+} concentration, artificially boosted the measured $MnCO_3$ purity in the unwashed precipitate. The washed $MnCO_3$ had a slightly higher purity compared to the unwashed product due to the removal of the entrained solution during the washing process. However, the purity of the washed $MnCO_3$ also increased with CO_2 bubbling time, increasing from 97.6 to 99.0 wt.% between 1 and 12 h. This trend demonstrates two key points: first, the residual feed solution was indeed entrained and removed during washing; and second, the Mg^{2+} and Ca^{2+} impurities did not co-precipitate significantly, contrary to the initial assertion.

These results show that the use of CO_2 and NH_3 (aq) can produce high-purity $MnCO_3$ from an industrial $MnSO_4$ leach solution. Additionally, washing the precipitate is important to improve the purity of the product because the residual solution is entrained during filtration. The final purity was slightly lower than the battery-grade manganese products by 0.9 wt. %, likely because less water was used for washing the product. There was no statistical difference observed between the rejection levels and $MnCO_3$ purity when CO_2 is bubbled for 8 and 12 h. It is therefore recommended to wash the product more than three times or use more water to wash.

5.3.1 Effect of CO_2 bubbling time on the PSD, morphology, and shape of particles

5.3.1.1 Particle Size Distribution

The PSD of the $MnCO_3$ particles as CO_2 bubbling time increased from 1 to 12 h is shown in Figure 5.10.

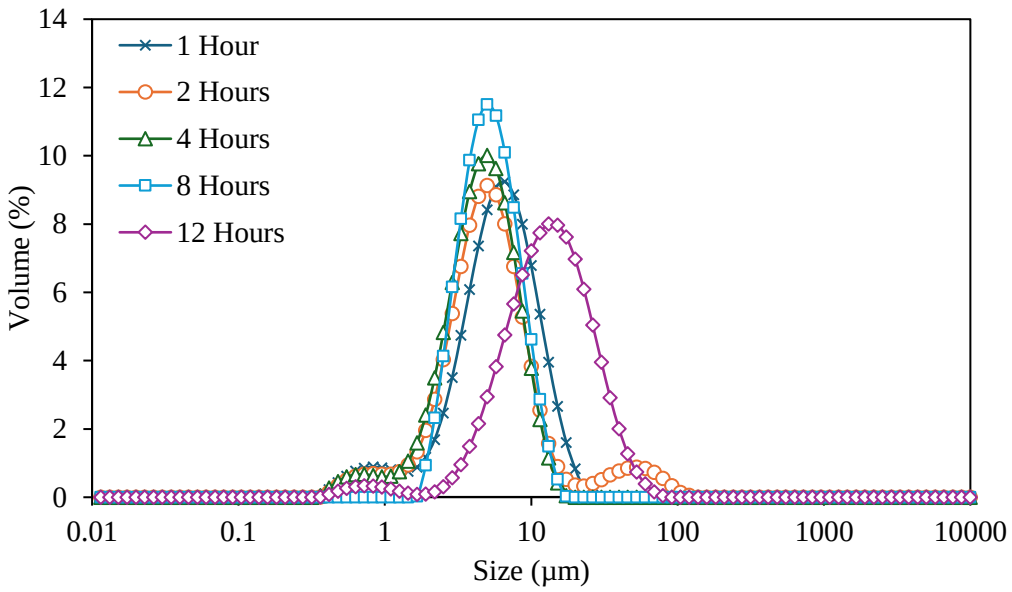

Figure 5.10: Effect of CO_2 bubbling time on particle size distribution of the precipitate.

As the CO_2 bubbling time was increased from 1 to 2 h, the distribution slightly shifted to the left, with d_{50} decreasing from 5.6 to 4.7 µm. An increased CO_2 bubbling time to 4 and 8 h led to d_{50} remaining in the range between 4.3 and 4.8 µm, showing no significant size differences. The modal particle size slightly decreased from 6.6 to 5.0 µm after bubbling CO_2 for 8 h.

Further increase in CO_2 bubbling time to 12 h led to the PSD shifting towards larger particles, with d_{50} increasing to 12.1 µm, which is consistent with findings by Pagnanelli et al. (2013). The particles with sizes between 20 and 100 µm when CO_2 was bubbled for 2 h were most likely agglomerates. Furthermore, the particles with sizes between 0.4 and 2 µm, which were initially agglomerated at shorter bubbling times, dissolved over longer bubbling times.

The observed changes in PSD suggest that longer bubbling times promote particle growth and aggregation. The decreasing modal particle size between 1 and 8 h CO_2 bubbling time indicates that nucleation rate is likely favoured than growth rate at this range, or there is localized dissolution of the precipitate. This observation was also noted by Radha and Navrotsky (2014) where $MnCO_3$ particles reached a maximum size after 2.5 h, followed by a decrease after 5 h.

The increased particle size after bubbling CO_2 for 12 h means the total surface area of crystals was reduced, reducing the entrainment of the residual solution, and leading to higher purity. These results show that bubbling CO_2 for less than 8 h will result in a predominant particle size of 5.0 µm, and this will increase to 12.1 µm when CO_2 is bubbled for 12 h.

5.3.1.2 XRD of $MnCO_3$ particles

Figure 5.11 shows that the washed $MnCO_3$ precipitates become more crystalline with increasing CO_2 bubbling time from 1 to 12 h. This is demonstrated by the gradual increase in the XRD peaks.

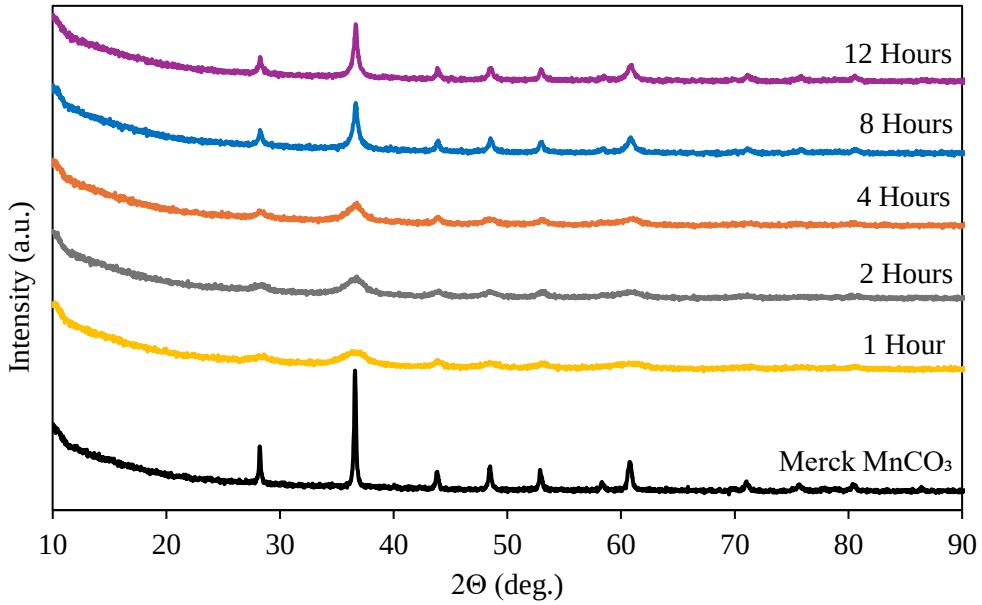

Figure 5.11: XRD patterns o obtained $MnCO_3$ precipitate at 1 to 12 h of CO_2 bubbling times.

The reference $MnCO_3$ (Merck) exhibits characteristic diffraction peaks at 28.21°, 36.60°, 43.85°, 48.49°, 52.88°, and 60.77°. All precipitates obtained at different CO_2 bubbling times display similar peaks, corresponding to the rhombohedral $MnCO_3$ crystal structure, which confirms the formation of high-purity $MnCO_3$ with no detectable secondary phases. Longer CO_2 bubbling time resulted in the increased intensity of these peaks in the precipitate, which aligns with the findings by Jimoh et al. (2017). Additionally, the diffraction peak at 36.60° shows a well-characterized calcite form of $MnCO_3$.

The increasing intensity of the $MnCO_3$ peaks was probably because longer CO_2 bubbling times promoted crystal growth, which resulted in more defined and ordered crystal lattices. This led to improved crystallinity, enhancing the diffraction signal, and resulting in sharper and more intense XRD peaks. The results also show that bubbling CO_2 for 1 h produced amorphous $MnCO_3$ particles, which indicates that there was initially a high precipitation rate which slowly decreased, as shown by the decreasing amorphous content, making the product more crystalline. This observation is in agreement with that reported by Radha and Navrotsky (2014), i.e., that amorphous $MnCO_3$ precipitates undergo slow crystallisation to transform into a calcite-like rhodochrosite phase over 40 days of storage.

5.3.1.3 SEM Images of $MnCO_3$ particles

Figure 5.12 shows the SEM images of the $MnCO_3$ particles produced at CO_2 bubbling time from 1 to 12 h.

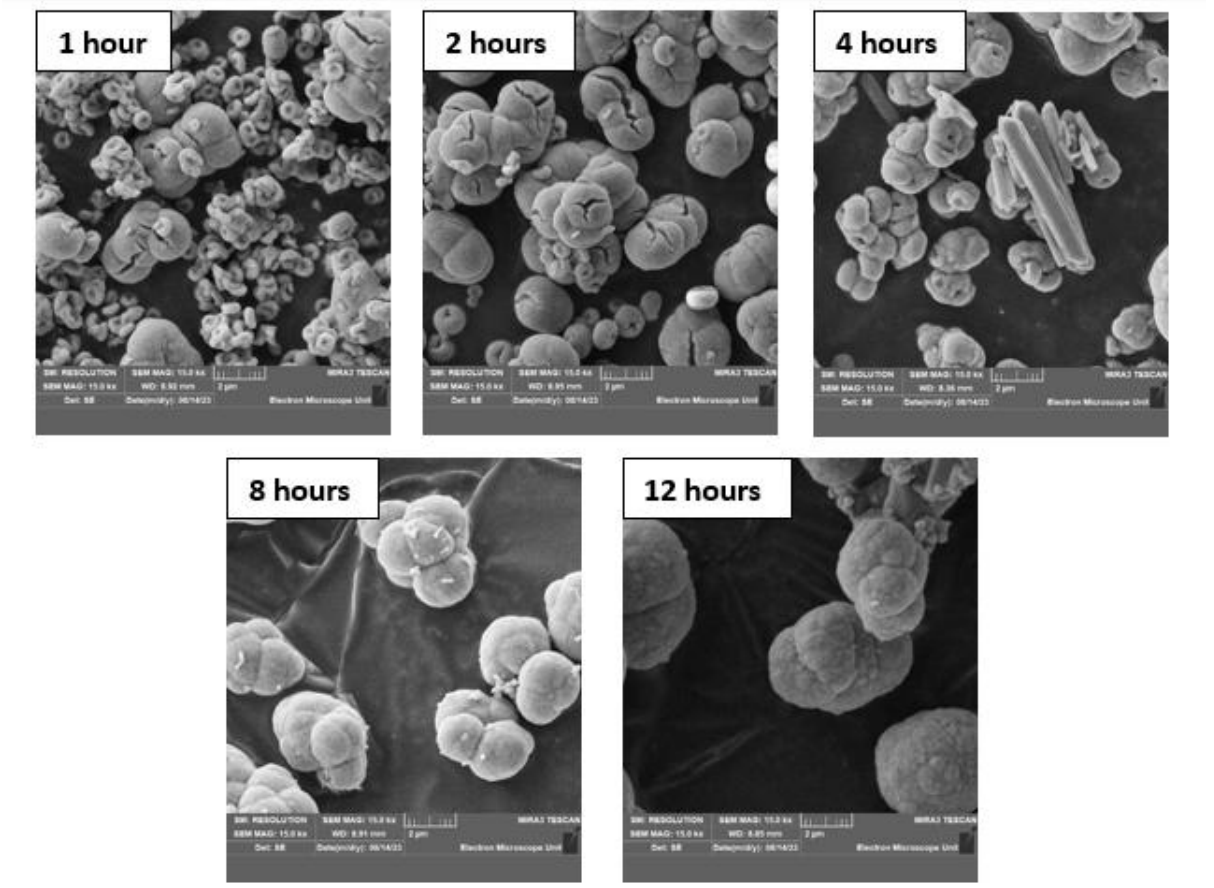

Figure 5.12: SEM images of $MnCO_3$ precipitated at different CO_2 bubbling time.

Bubbling CO_2 for 1 h formed a mixture of spherical $MnCO_3$ crystals with an average diameter 1.0 µm and larger $MnCO_3$ crystals with an average diameter of about 2.0 µm. As the CO_2 bubbling time was increased to 12 h, the morphology of the $MnCO_3$ crystals changed to larger non-uniform particles with rough surfaces, and the small particles disappeared entirely, which indicates that crystals are agglomerated and growing. This trend is in contrast to a study by Yu et al. (2019a) who produced hexagonal crystals of $MnCO_3$ when using a batch mode at pH 6.6. At 4 h, the rod-like crystals with regular morphology are likely $MgCO_3.3H_2O$, which is similar to that reported by Geng et al. (2019).

These results suggest that longer CO_2 bubbling times enhance the morphology of the $MnCO_3$ particles, which shift from small amorphous particles to larger, more crystalline structures.

6 CONCLUSIONS AND RECOMMENDATIONS

This study demonstrated the feasibility of using CO_2 and NH_3 for the selective recovery of Mn^{2+} from an industrial $MnSO_4$ pregnant leach solution containing at least 93.9 wt.% Mn^{2+}, 2.23 wt.% Mg^{2+}, and 0.14 wt.% Ca^{2+}. The predicted Mn^{2+} recovery and the rejections of Mg^{2+} and Ca^{2+} from thermodynamic simulation results were compared with laboratory experimental results in a 1.0 L semi-batch and continuously stirred glass reactor at ambient temperature and pressure. The bubbling rate of CO_2 and the speed of the agitator were kept constant at 0.4 L/min and 500 rpm, respectively. Thermodynamic simulation results showed that Mn^{2+} recovery is optimal in the pH range of 5.9-11.7, with recovery increasing with pH. However, high Mn^{2+} selectivity is favourable at pH < 6.6, with moderate selectivity present at pH values between 6.6 and 7.2.

Experiments investigated the effect of pH values from 5.0 to 6.6, which was controlled using 28-30% NH_3 (aq), and the effect of CO_2 bubbling times from 1 to 12 h. The Mn^{2+} recovery increased from 8.7% to 39.6% when pH was increased from 5.0 to 6.6. This was attributed to the increase in supersaturation and decreased Mn solubility, which increased the precipitation rate of $MnCO_3$. However, these recoveries were lower than those predicted by the thermodynamic simulations (> 94% at pH 5.0 and almost 100% at pH 6.6). On the other hand, the rejection of Mg^{2+} and Ca^{2+} decreased from 95.6% to 78.1% and 92.0% to 88.5% with increasing pH from 5.0 to 6.6, respectively. There was no significant change in particle size and morphology when pH was increased from 5.0 to 6.6.

Increasing the CO_2 bubbling time from 1 to 8 h resulted in an increased average Mn^{2+} recovery from 18.7 to 61.3%, attributed to the continuous HCO_3^- and CO_3^{2-} supply. Prolonging bubbling time to 12 h led to no statistical change in Mn^{2+} recovery. The rejection of Mg^{2+} decreased from 80.6% to 57.6%, whereas the rejection of Ca^{2+} decreased from 81.7% to 46.3% with increasing CO_2 bubbling time from 1 to 8 h. The rejections of Mg^{2+} and Ca^{2+} did not change statistically when bubbling for longer than 8 h.

The PSD showed a peak volume percentage at 6.6 µm after 1 h, 5.0 µm after 2, 4 and 8 h, and 12.1 µm at 12 h of CO_2 bubbling time, respectively. Longer bubbling times lead to more crystalline $MnCO_3$ particles. Precipitation was optimal at a pH of 6.6 and 8 h CO_2 bubbling time, in which the washed $MnCO_3$ precipitate contained 99.0 wt.% Mn, 0.15 wt.% Ca, and 0.05 wt.% Mg, meeting the high purity Mn specifications, but slightly lower than the battery grade Mn (> 99.9 wt.%, ultra-high purity).

This study has demonstrated that the utilization of CO_2 and NH_3 in the purification of industrial $MnSO_4$ pregnant leach solution with Mg^{2+} and Ca^{2+} impurities has great potential for industrial application. However, the CO_2 demand was significantly higher and thus longer bubbling times were required to achieve higher recoveries. It is therefore recommended to investigate the use of nanobubbles, increased CO_2 partial pressure, and pH values between 6.6 and 7.0 to increase the efficiency of the dissolution of CO_2, thus increasing the Mn^{2+} recovery. Additionally, the effects of pH and CO_2 bubbling time, respectively on all sampled $MnSO_4$ PLS solutions should be investigated.

7 REFERENCES

Abdullah, S. N., Hamzah, F., Husain, N. C., Veny, H., Rodhi, M. N. M. & Mohidem, N. A. 2023. Effect of Temperature and CO_2 Flowrate on the Formation of $CaCO_3$ in the Hydration Reaction of CO_2 Catalyzed by Immobilized Carbonic anhydrase into PVDF Membrane. *Chemical Engineering Transactions,* 106**,** 1015-1020. https://doi.org/10.3303/CET23106170

Abe, M., Tanaka, S., Noguchi, M. & Yamasaki, A. 2021. Investigation of Mineral Carbonation with Direct Bubbling into Concrete Sludge. *ACS Omega,* 6(24)**,** 15564-15571. https://doi.org/10.1021/acsomega.0c04758

Aboudheir, A., deMontigny, D., Tontiwachwuthikul, P. & Chakma, A. Important Factors Affecting Carbon Dioxide Removal Efficiency By Using Extra-high Concentrated Monoethanolamine Solutions and High-Capacity Packings. SPE Gas Technology Symposium, 15-18 March 1998 Calgary, Alberta, Canada. Society of Petroleum Engineers. https://api.semanticscholar.org/CorpusID:56120518%7D

Ali, S., Iqbal, Y., Shah, K. H. & Fahad, M. 2022. Synthesis and kinetic modeling of manganese carbonate precipitated from manganese sulfate solution. *Chemical Engineering Communications,* 209(1)**,** 96-107. https://doi.org/10.1080/00986445.2020.1839434

Altiner, M. 2018. Influences of CO_2 Bubbling Types on Preparation of Calcite Nanoparticles by Carbonation Process. *Periodica Polytechnica Chemical Engineering,* 62(2)**,** 209-214. https://doi.org/10.3311/PPch.10664

Andrade, C. 2020. Evaluation of the degree of carbonation of concretes in three environments. *Construction and Building Materials,* 230**,** 116804. https://doi.org/10.1016/j.conbuildmat.2019.116804

Andrade, C. & Sanjuán, M. Á. 2018. Updating Carbon Storage Capacity of Spanish Cements. *Sustainability,* 10(12)**,** 4806. https://doi.org/10.3390/su10124806

Aziz, H. A. & Smith, P. G. 1992. The influence of pH and coarse media on manganese precipitation from water. *Water Research,* 26(6)**,** 853-855. https://doi.org/10.1016/0043-1354(92)90017-X

Bamforth, S., Manning, D., Singleton, I., Younger, P. & Johnson, K. 2006. Manganese removal from mine waters – investigating the occurrence and importance of manganese carbonates. *Applied Geochemistry,* 21**,** 1274-1287. https://doi.org/10.1016/j.apgeochem.2006.06.004

Battaglia, G., Berkemeyer, L., Cipollina, A., Cortina, J. L., Fernandez de Labastida, M., Lopez Rodriguez, J. & Winter, D. 2022. Recovery of Lithium Carbonate from Dilute Li-Rich Brine via Homogenous and Heterogeneous Precipitation. *Ind Eng Chem Res,* 61(36)**,** 13589-13602. https://doi.org/10.1021/acs.iecr.2c01397

Baumgartner, S. J. & Groot, D. 2014. The recovery of manganese products from ferromanganese slag using a hydrometallurgical route. *Journal of the Southern African Institute of Mining and Metallurgy,* 114**,** 331-340.

Beckmann, W. 2013. Mechanisms of Crystallization. *Crystallization.* https://doi.org/10.1002/9783527650323.ch2

Benchmark Mineral Intelligence 2020. Manganese Sulphate Market Outlook. *In:* SOURCE, B. (ed.). https://www.benchmarkminerals.com/forecasts/manganese/

Botsaris, G. D. 1976. Secondary Nucleation — A Review. *In:* MULLIN, J. W. (ed.) *Industrial Crystallization.* Boston, MA: Springer US. https://doi.org/10.1007/978-1-4615-7258-9_1

Brugman, S., Ottenbros, A., Megens, F., van Enckevort, W. & Vlieg, E. 2020. Epitaxy of Rhodochrosite ($MnCO_3$) on Muscovite Mica and Its Relation with Calcite ($CaCO_3$). *Crystal Growth & Design,* 20(7)**,** 4802–4810. https://doi.org/10.1021/acs.cgd.0c00578

Butler, J. 2019. *Carbon Dioxide Equilibria and their Applications*. https://doi.org/10.1201/9781315138770

Charpentier, J.-C. 1981. Mass-Transfer Rates in Gas-Liquid Absorbers and Reactors. *In:* DREW, T. B., COKELET, G. R., HOOPES, J. W. & VERMEULEN, T. (eds.) *Advances in Chemical Engineering.* Academic Press. https://doi.org/10.1016/S0065-2377(08)60025-3

Chen, H., Liu, R., Liu, Z., Shu, J. & Tao, C. 2016. Immobilization of Mn and NH_4^+-N from electrolytic manganese residue waste. *Environmental Science and Pollution Research,* 23(12)**,** 12352-12361. https://doi.org/10.1007/s11356-016-6446-2

Chen, P., Tang, S., Yue, H., Liu, C., Li, C. & Liang, B. 2017. Lithium Enrichment of High Mg/Li Ratio Brine by Precipitation of Magnesium via Combined CO_2 Mineralization and Solvent Extraction. *Industrial & Engineering Chemistry Research,* 56(19)**,** 5668-5678. https://doi.org/10.1021/acs.iecr.6b04892

Chiang, P.-C. & Pan, S.-Y. 2017. *Carbon dioxide mineralization and utilization*, Springer Singapore. https://doi.org/10.1007/978-981-10-3268-4

Chitrakar, R., Kanoh, H., Miyai, Y. & Ooi, K. 2001. Recovery of Lithium from Seawater Using Manganese OxideAdsorbent ($H_{1.6}Mn_{1.6}O_4$) Derived from $Li_{1.6}Mn_{1.6}O_4$. *Industrial & Engineering Chemistry Research,* 40**,** 2054-2058. https://doi.org/10.1021/ie000911h

Choppin, G. R., Liljenzin, J.-O. & Rydberg, J. A. N. 2002. CHAPTER 9 - Uses of Radioactive Tracers. *In:* CHOPPIN, G. R., LILJENZIN, J.-O. & RYDBERG, J. A. N. (eds.) *Radiochemistry and Nuclear Chemistry (Third Edition).* Woburn: Butterworth-Heinemann. https://doi.org/10.1016/B978-075067463-8/50009-1

Christo N, N. 2015. Theory of Nucleation. *In:* NISHINAGA, T. & ELSEVIER (eds.) *Handbook of crystal growth.* Second edition. ed. Amsterdam: Elsevier. https://doi.org/10.1016/B978-0-444-56369-9.00007-1

Contreras Moreno, V., Ledoux, A., Estel, L., Derrouiche, S. & Denieul, M.-P. 2017. Valorisation of CO2 with epoxides: Influence of gas/liquid mass transfer on reaction kinetics. *Chemical Engineering Science,* 170**,** 77-90. https://doi.org/10.1016/j.ces.2017.01.050

Deocampo, D. M. 2010. Chapter 1 The Geochemistry of Continental Carbonates. *In:* ALONSO-ZARZA, A. M. & TANNER, L. H. (eds.) *Developments in Sedimentology.* Elsevier. https://doi.org/10.1016/S0070-4571(09)06201-3

Ding, Y., Cano, Z. P., Yu, A., Lu, J. & Chen, Z. 2019. Automotive Li-Ion Batteries: Current Status and Future Perspectives. *Electrochemical Energy Reviews,* 2**,** 1-28. https://doi.org/10.1007/s41918-018-0022-z

Doran, P. M. 2013. Chapter 11 - Unit Operations. *In:* DORAN, P. M. (ed.) *Bioprocess Engineering Principles (Second Edition).* London: Academic Press. https://doi.org/10.1016/B978-0-12-220851-5.00011-3

Dri, M., Sanna, A. & Maroto-Valer, M. M. 2014. Mineral carbonation from metal wastes: Effect of solid to liquid ratio on the efficiency and characterization of carbonated products. *Applied Energy,* 113**,** 515-523. https://doi.org/10.1016/j.apenergy.2013.07.064

Du, B., Zhou, C., Li, X., Guo, T. & Wang, Z. 2015. A kinetic study of Mn(II) precipitation of leached aqueous solution from electrolytic manganese residues. *Toxicological & Environmental Chemistry,* 97(3-4)**,** 349-357. https://doi.org/10.1080/02772248.2015.1050188

Du, M. Effect of pH on desorption of CO_2 from alkanolamine - rich solvents. 2017. 20-91. https://doi.org/10.1063/1.4992908

Du, Y., Fu, C., Gong, B., Miao, E., Zheng, X., Xiong, Z., Zhao, Y. & Zhang, J. 2021. Real-time investigation of the CO_2 mineral carbonation reaction rate through direct aqueous route using semi-dry desulfurization slag. *Journal of CO_2 Utilization,* 51**,** 101-614. https://doi.org/10.1016/j.jcou.2021.101614

Dukes, A. D., 3rd 2020. Measuring the Henry's Law Constant for Carbon Dioxide and Water with UV-visible Absorption Spectroscopy. *Anal Sci,* 36(8)**,** 971-975. https://doi.org/10.2116/analsci.19P477

Eloneva, S., Said, A., Fogelholm, C.-J. & Zevenhoven, R. 2012. Preliminary assessment of a method utilizing carbon dioxide and steelmaking slags to produce precipitated calcium carbonate. *Applied Energy,* 90(1)**,** 329-334. https://doi.org/10.1016/j.apenergy.2011.05.045

Farrah, H. E., Lawrance, G. A. & Wanless, E. J. 2007. Solubility of calcium sulfate salts in acidic manganese sulfate solutions from 30 to 105 °C. *Hydrometallurgy,* 86(1)**,** 13-21. https://doi.org/10.1016/j.hydromet.2006.10.003

Fick, A. 1855. Ueber Diffusion. *Annalen der Physik,* 170(1)**,** 59-86. https://doi.org/10.1002/andp.18551700105

Fleischmann, J., Hanicke, M., Horetsky, E., Ibrahim, D., Jautelat, S., Linder , M., Schaufuss , P., Torscht , L. & van de Rijt , A. 2023. Battery 2030: Resilient, sustainable, and circular.

Funes, A., de Vicente, J., Cruz-Pizarro, L. & de Vicente, I. 2014. The influence of pH on manganese removal by magnetic microparticles in solution. *Water Research,* 53**,** 110-122. https://doi.org/10.1016/j.watres.2014.01.029

Gamsjager, H., Koenigsberger, E. & Preis, W. 1998. Solubilities of metal carbonates. *Pure and Applied Chemistry,* 70(10)**,** 1913-1920. https://doi.org/10.1351/pac199870101913

Gao, X., Han, Z., Zhao, Y., Zhang, J., Zhai, D., Li, J., Qin, Y., Liu, F., Wang, Q., Steiner, M. & Han, C. 2024. Microbial-mineral interaction experiments and density functional theory calculations revealing accelerating effects for the dolomitization of calcite surfaces by organic components. *Science of The Total Environment,* 915**,** 169971. https://doi.org/10.1016/j.scitotenv.2024.169971

Garcia, J. C., Barai, P., Chen, J., Gutierrez, A., Wen, J., Arslan, I., Wang, X., Fister, T. T., Iddir, H. & Srinivasan, V. 2020. Predicting Morphological Evolution during Coprecipitation of $MnCO_3$ Battery Cathode Precursors Using Multiscale Simulations Aided by Targeted Synthesis. *Chemistry of Materials,* 32(21)**,** 9126-9139. https://doi.org/10.1021/acs.chemmater.0c01929

Geng, X., Lv, L., Li, C., Zhang, T., Liang, B., Chen, Y. & Tang, S. 2019. The kinetics of CO_2 indirect mineralization of $MgSO_4$ to produce $MgCO_3 \cdot 3H_2O$. *Journal of CO_2 Utilization,* 33**,** 64-71. https://doi.org/10.1016/j.jcou.2019.04.017

Giulietti, M., Seckler, M. m., Derenzo, S., Ré, M. & Cekinski, E. 2001. Industrial crystallization and precipitation from solutions: State of the technique. *Brazilian Journal of Chemical Engineering,* 18(4)**,** 1-25. https://doi.org/10.1590/S0104-66322001000400007

Gomez-Martin, A., Reissig, F., Frankenstein, L., Heidbüchel, M., Winter, M., Placke, T. & Schmuch, R. 2022. Magnesium Substitution in Ni-Rich NMC Layered Cathodes for High-Energy Lithium Ion Batteries. *Advanced Energy Materials,* 12(8)**,** 2103045. https://doi.org/10.1002/aenm.202103045

Gul, A. & Tezcan Un, U. 2022. Effect of Temperature and Gas Flow Rate on CO_2 Capture. *European Journal of Sustainable Development Research,* 6(2), 2542-4742. https://doi.org/10.21601/ejosdr/11727

Hai, Y., Zhang, Z., Liu, H., Liao, L., Fan, P., Wu, Y., Lv, G. & Mei, L. 2019. Facile Controlled Synthesis of Spinel $LiMn_2O_4$ Porous Microspheres as Cathode Material for Lithium Ion Batteries. *Frontiers in Chemistry,* 7. https://doi.org/10.3389/fchem.2019.00437

Han, B., Anwar Ui Haq, R. & Louhi-Kultanen, M. 2020. Lithium carbonate precipitation by homogeneous and heterogeneous reactive crystallization. *Hydrometallurgy,* 195, 105386. https://doi.org/10.1016/j.hydromet.2020.105386

Han, Z., Qi, P., Zhao, Y., Guo, N., Yan, H., Tucker, M. E., Li, D., Wang, J. & Zhao, H. 2022. High Mg/Ca Molar Ratios Promote Protodolomite Precipitation Induced by the Extreme Halophilic Bacterium Vibrio harveyi QPL2. *Front Microbiol,* 13, 821968. https://doi.org/10.3389/fmicb.2022.821968

Hariprasad, D., Dash, B., Ghosh, M. & Anand, S. 2009. Mn recovery from medium grade ore using a waste cellulosic reductant. *Indian Journal of Chemical Technology,* 16(4), 322-327.

Harris, M. M. D. M. & Auerswald, K. 1977. The production of electrolytic manganese in South Africa. *Journal of the Southern African Institute of Mining and Metallurgy,* 77(7), 137-142. https://doi.org/10.10520/AJA0038223X_738

Higbie, R. 1935. The rate of absorption of a pure gas into a still liquid during short periods of exposure. *American Institute of Chemical Engineers,* 31, 365-389.

Hobbs, F. W. C., Fang, Y., Lebrun, N., Yang, Y. & Xu, H. 2024. Co-precipitation of primary dolomite and Mg-rich clays in Deep Springs Lake, California. *Sedimentology,* 71(4), 1363-1383. https://doi.org/10.1111/sed.13176

Hongliang, C., Liu, R., Long, Q. & Liu, Z. 2016. Carbonation precipitation of manganese from electrolytic manganese residue treated by CO_2 with alkaline additives. *International Conference on Machinery, Materials Engineering, Chemical Engineering and Biotechnology.* https://doi.org/10.2991/mmeceb-15.2016.142

Huang, S., Wu, H., Chen, P., Guo, Y., Nie, B., Chen, B., Liu, H. & Zhang, Y. 2015. Facile pH-mediated synthesis of morphology-tunable $MnCO_3$ and their transformation to truncated octahedral spinel $LiMn_2O_4$ cathode materials for superior lithium storage. *Journal of Materials Chemistry A,* 3(7)**,** 3633-3640. https://doi.org/10.1039/C4TA06522K

International Energy Agency 2023. Global EV Outlook 2023 Catching up with climate ambitions. https://iea.blob.core.windows.net/assets/dacf14d2-eabc-498a-8263-9f97fd5dc327/GEVO2023.pdf

International Manganese Institute. 2024. *Manganese Essential For Life* [Online]. Paris, France: International Manganese Institute. Available: https://www.manganese.org/ [Accessed April 23 2024].

Ismail, A., Ahmed, E., Ibrahim, A. & Ahmed, M. 2008. A Comparative Study on Acid Leaching of Low Grade Manganese Ore Using Some Industrial Wastes as Reductants. *The Canadian Journal of Chemical Engineering,* 82**,** 1296-1300. 10.1002/cjce.5450820618

Ji, L., Zheng, X., Ren, Y., Wang, Y., Wang, Y. & Yan, S. 2024. CO_2 sequestration and recovery of high-purity $CaCO_3$ from bottom ash of masson pine combustion using a multifunctional reagent—amino acid. *Separation and Purification Technology,* 329**,** 125171. https://doi.org/10.1016/j.seppur.2023.125171

Jimoh, O., Otitoju, T., Hussin, H., Ariffin, K. S. & Baharun, N. 2017. Understanding the Precipitated Calcium Carbonate (PCC) Production Mechanism and Its Characteristics in the Liquid-Gas System Using Milk of Lime (MOL) Suspension. *South African journal of chemistry. Suid-Afrikaanse tydskrif vir chemie,* 70**,** 1-7. https://doi.org/10.17159/0379-4350/2017/v70a1

Jones, A. G. 1993. Particle breakage, abnormal growth and agglomeration during industrial crystallization. *Analytical Proceedings,* 30(11)**,** 456-457. https://doi.org/10.1039/AP9933000456

Jones, A. G. 2002. 5 - Crystal formation and breakage. *In:* JONES, A. G. (ed.) *Crystallization Process Systems.* Oxford: Butterworth-Heinemann. https://doi.org/10.1016/B978-075065520-0/50006-7

Ju, J., Feng, Y., Li, H., Wu, R., Xue, Z. & Ma, R. 2023. High-efficiency and environment-friendly separation and recovery of manganese from braunite via the ammonium sulfate roasting-water leaching process: Behavior and mechanism. *Chemical Engineering Journal,* 466**,** 143218. https://doi.org/10.1016/j.cej.2023.143218

Kartini, E., Fakhrudin, M., Astuti, W., Sumardi, S. & Mubarok, Z. 2022. *The study of (Ni,Mn,Co)SO_4 as raw material for NMC precursor in lithium ion battery*. https://doi.org/10.1063/5.0122596

Kesler, S. & Simon, A. 2015. *Mineral Resources, Economics and the Environment*. https://doi.org/10.1017/cbo9781139871426.002

Korchef, A. & Touaibi, M. 2020. Effect of pH and temperature on calcium carbonate precipitation by CO_2 removal from iron-rich water. *Water and Environment Journal,* 34(3)**,** 331-341. https://doi.org/10.1111/wej.12467

Lee, M. g., Jang, Y. N., Ryu, K. w., Kim, W. & Bang, J.-H. 2012. Mineral carbonation of flue gas desulfurization gypsum for CO_2 sequestration. *Energy,* 47(1)**,** 370-377. https://doi.org/10.1016/j.energy.2012.09.009

Levich, V. G. & Tobias, C. W. 1963. Physicochemical Hydrodynamics. *Journal of The Electrochemical Society,* 110(11)**,** 251C. https://doi.org/10.1149/1.2425619

Lewis, A. 2019. Precipitation. *In:* DUNNE, R. C., KAWATRA, S. K. & YOUNG, C. A. (eds.) *SME Mineral Processing and Extractive Metallurgy Handbook.* Littleton, UNITED STATES: Society for Mining, Metallurgy & Exploration, Incorporated. http://ebookcentral.proquest.com/lib/uoct/detail.action?docID=5649299

Lewis, A. E. 2010. Review of metal sulphide precipitation. *Hydrometallurgy,* 104(2)**,** 222-234. https://doi.org/10.1016/j.hydromet.2010.06.010

Li, J., Du, D., Peng, Q., Wu, C., Lv, K., Ye, H., Chen, S. & Zhan, W. 2018. Activation of silicon in the electrolytic manganese residue by mechanical grinding-roasting. *Journal of Cleaner Production,* 192**,** 347-353. https://doi.org/10.1016/j.jclepro.2018.04.184

Lin, Q.-q., Gu, G.-h., Wang, H., Zhu, R.-f., Liu, Y.-c. & Fu, J.-g. 2016a. Preparation of manganese sulfate from low-grade manganese carbonate ores by sulfuric acid leaching.

International Journal of Minerals, Metallurgy, and Materials, 23(5), 491-500. https://doi.org/10.1007/s12613-016-1260-x

Lin, Q. Q., Gu, G. H., Wang, H., Wang, C. Q., Liu, Y. C., Zhu, R. F. & Fu, J. G. 2016b. Separation of manganese from calcium and magnesium in sulfate solutions via carbonate precipitation. *Transactions of Nonferrous Metals Society of China,* 26(4), 1118-1125. https://doi.org/10.1016/S1003-6326(16)64210-3

Lingane, J. J. & Karplus, R. 1946. New method for determination of manganese. *Industrial & Engineering Chemistry Analytical Edition,* 18(3), 191-194. https://pubs.acs.org/doi/10.1021/i560151a010

Liu, D., Xu, Y., Papineau, D., Yu, N., Fan, Q., Qiu, X. & Wang, H. 2019. Experimental evidence for abiotic formation of low-temperature proto-dolomite facilitated by clay minerals. *Geochimica et Cosmochimica Acta,* 247, 83-95. https://doi.org/10.1016/j.gca.2018.12.036

Lívanský, K. 1982. Effect of temperature and pH on absorption of carbon dioxide by a free level of mixed solutions of some buffers. *Folia Microbiol (Praha),* 27(1), 55-9. https://doi.org/10.1007/bf02883839

Loewenthal, B. L. & Maais Gv, R. 1977. Calcium carbonate precipitation kinetics, part 2 effects of magnesium. *Water SA,* 3(3), 155-165. https://doi.org/10.10520/AJA03784738_2087

Lu, J., Dreisinger, D. & Glück, T. 2016. Electrolytic manganese metal production from manganese carbonate precipitate. *Hydrometallurgy,* 161, 45-53. https://doi.org/10.1016/j.hydromet.2016.01.010

Lu, W., Guo, H., Chou, I. M., Burruss, R. C. & Li, L. 2013. Determination of diffusion coefficients of carbon dioxide in water between 268 and 473K in a high-pressure capillary optical cell with in situ Raman spectroscopic measurements. *Geochimica et Cosmochimica Acta,* 115, 183-204. https://doi.org/10.1016/j.gca.2013.04.010

Lyu, K., Ma, B., Chen, Y., Wang, C. & Yang, H. 2021. Efficient and clean manganese electrowinning in an anion-exchange membrane electrolyzer by pulse current electrodeposition method. *Journal of Cleaner Production,* 318, 128611. https://doi.org/10.1016/j.jclepro.2021.128611

Ma, L., Nie, Z., Xi, X. & Li, X. 2013. Theoretical simulation and experimental study on nickel, cobalt, manganese separation in complexation–precipitation system. *Separation and Purification Technology,* 108**,** 124-132. https://doi.org/10.1016/j.seppur.2013.01.044

Ma, X., Abe, Y., Kaneko, A., Fujimoto, S. & Murakami, C. 2017. Study on Dissolution Process of Liquid CO_2 into Water under High Pressure Condition for CCS. *Energy Procedia,* 114**,** 5430-5437. https://doi.org/10.1016/j.egypro.2017.03.1687

Markov, I. V. 2016. *Crystal growth for beginners : fundamentals of nucleation, crystal growth and epitaxy,* New Jersey, World Scientific.

Masindi, V., Foteinis, S., Renforth, P. & Chatzisymeon, E. 2023. Wastewater Treatment for Carbon Dioxide Removal. *ACS Omega,* 8(43)**,** 40251-40259. https://doi.org/10.1021/acsomega.3c04231

Masindi, V., Foteinis, S., Renforth, P., Ndiritu, J., Maree, J. P., Tekere, M. & Chatzisymeon, E. 2022. Challenges and avenues for acid mine drainage treatment, beneficiation, and valorisation in circular economy: A review. *Ecological Engineering,* 183**,** 106740. https://doi.org/10.1016/j.ecoleng.2022.106740

Mettler Toledo. 2024. *Supersaturation and Crystallization - The Driving Force For Crystallization* [Online]. Available: https://www.mt.com/gb/en/home/applications/L1_AutoChem_Applications/L2_Crystallization/Supersaturation_Application.html#productsolutions [Accessed April 15 2024].

Mills, J. V., Barnhart, H. A., DePaolo, D. J. & Lammers, L. N. 2022. New insights into Mn^{2+} and Mg^{2+} inhibition of calcite growth. *Geochimica et Cosmochimica Acta,* 334**,** 338-367. https://doi.org/10.1016/j.gca.2022.06.015

Mishra, K. K. & Kapoor, M. L. 1978. Kinetics of liquid-gas reactions through bubbles. *Hydrometallurgy,* 3(1)**,** 75-83. https://doi.org/10.1016/0304-386X(78)90008-7

Muanda, M. M. & Omalanga, P. P. D. 2021. Modeling and Optimization of Manganese Carbonate Precipitation Using Response Surface Methodology and Central Composite Rotatable Design. *The Journal of Engineering and Exact Sciences,* 7(3)**,** 1-22. https://doi.org/10.18540/jcecvl7iss3pp12632-01-22e

Mulana, F., Munawar, E., Heldiana, H. & Rahmi, M. 2022. The effect of carbon dioxide gas pressure on solubility, density and pH of carbon dioxide – Water mixtures. *Materials Today: Proceedings,* 63**,** S46-S49. https://doi.org/10.1016/j.matpr.2022.01.033

Mullin, J. W. 2001. *Crystallization*, Elsevier Science.

Mwana, C., Kabangu Ngoie, M., Mbalaba Francis, M., Francis, K., Constantin, M., Gabriel, I. & Israel, I. 2022. Manganese Dioxide (MnO_2) Gaining by Calcination of Manganese Carbonate ($MnCO_3$) Precipitated from Cobalt Removal Solutions. *Open Journal of Applied Sciences,* 12**,** 598-613. https://doi.org/10.4236/ojapps.2022.124041

Myerson, A. 2002. *Handbook of Industrial Crystallization*, Elsevier Science.

Myerson, A. S., Erdemir, D. & Lee, A. Y. 2019. *Handbook of Industrial Crystallization,* Cambridge, Cambridge University Press. https://doi.org/10.1017/9781139026949

Nayl, A. A., Ismail, I. M. & Aly, H. F. 2011. Recovery of pure $MnSO_4 \cdot H_2O$ by reductive leaching of manganese from pyrolusite ore by sulfuric acid and hydrogen peroxide. *International Journal of Mineral Processing,* 100(3)**,** 116-123. https://doi.org/10.1016/j.minpro.2011.05.003

Nie, X. D., Liang, Y. Z., Tang, Y. G. & Xie, H. L. 2013. Trace amounts of impurities in electrolytic manganese metal by sector field inductively coupled plasma mass spectrometry. *Journal of Central South University,* 20(12)**,** 3385-3390. https://doi.org/10.1007/s11771-013-1863-6

Ning, D., Wang, F., Zhou, C. B., Zhu, C. L. & Yu, H. B. 2010. Analysis of pollution materials generated from electrolytic manganese industries in China. *Resources Conservation and Recycling,* 54(8)**,** 506-511. https://doi.org/10.1016/j.resconrec.2009.10.007

Oishi, T., Koyama, K., Konishi, H., Tanaka, M. & Lee, J.-C. 2007. Influence of ammonium salt on electrowinning of copper from ammoniacal alkaline solutions. *Electrochimica Acta,* 53(1)**,** 127-132. https://doi.org/10.1016/j.electacta.2007.06.024

OLI Systems Inc 2017. Selecting AQ, MSE or MSE-SRK for your Scaling Calculation. http://www.aqsim.com/downloads.aqsim.com/2017-OLIWhitePaper-AQvsMSEandMSE-SRK-forOil_GasProduction.pdf

OLI Systems Inc 2021. Introduction to OLI Studio V11.5. https://wiki.olisystems.com/wiki/images/6/69/OLI_Studio_V11.5_User_Guide.pdf

OLI Systems Inc 2024. OLI Studio 11.5.1.9. Parsippany NJ 07054 USA. https://www.olisystems.com/

Pagnanelli, F., Granata, G., Moscardini, E. & Toro, L. 2013. Synthesis of $MnCO_3$ nanoparticles by microemulsions: statistical evaluation of the effects of operating conditions on particle size distribution. *Journal of Nanoparticle Research,* 15(9), 1887. https://doi.org/10.1007/s11051-013-1887-8

Pakarinen, J. & Paatero, E. 2011. Recovery of manganese from iron containing sulfate solutions by precipitation. *Minerals Engineering,* 24(13), 1421-1429. https://doi.org/10.1016/j.mineng.2011.06.004

Park, S. Y., Min, B. M., Lee, J. S., Nam, S. C., Han, K. H. & Hyun, J. S. 2004. Division of Petroleum Chemistry, American Chemical Society. *Petroleum Preprints Volume 49 #1-4.* Philadelphia, Pennsylvania, USA.

Powlson, D. S. & Dawson, C. J. 2022. Use of ammonium sulphate as a sulphur fertilizer: Implications for ammonia volatilization. *Soil Use and Management,* 38(1), 622-634. https://doi.org/10.1111/sum.12733

Qasem, N. A. A., Mohammed, R. H. & Lawal, D. U. 2021. Removal of heavy metal ions from wastewater: a comprehensive and critical review. *npj Clean Water,* 4(1), 36. https://doi.org/10.1038/s41545-021-00127-0

Qin, J.-T., Wang, J.-W., Wang, H.-F., Zhao, P.-Y. & Lu, F.-H. 2019. Equilibrium distribution of Mg in manganese electrolysis system. *Materials Research Express,* 6(9), 0965d4. https://doi.org/10.1088/2053-1591/ab34ac

Radha, A. & Navrotsky, A. 2014. Manganese carbonate formation from Amorphous and nanocrystalline precursors: Thermodynamics and geochemical relevance. *American Mineralogist,* 99(5-6), 1063-1070. https://doi.org/10.2138/am.2014.4734

Ramírez Velázquez, L. E., Palos, L., Le Page Mostefa, M. & Muhr, H. 2024. Recovery of lithium from Li-ion battery leachate by gas-liquid precipitation. *Journal of Crystal Growth,* 631**,** 127625. https://doi.org/10.1016/j.jcrysgro.2024.127625

Rosenberg, Y. O., Reznik, I. J., Zmora-Nahum, S. & Ganor, J. 2012. The effect of pH on the formation of a gypsum scale in the presence of a phosphonate antiscalant. *Desalination,* 284**,** 207-220. https://doi.org/10.1016/j.desal.2011.08.061

Rozelle, P., Mamula, N., Arnold, B., O'Brien, T., Rezaee, M. & Pisupati, S. 2021. Secondary Cobalt and Manganese Resources in Pennsylvania: Quantities, Linkage with Mine Reclamation, and Preliminary Flowsheet Evaluation for the U.S. Domestic Lithium-Ion Battery Supply Chain.

Said, A., Mattila, H.-P., Järvinen, M. & Zevenhoven, R. 2013. Production of precipitated calcium carbonate (PCC) from steelmaking slag for fixation of CO_2. *Applied Energy,* 112**,** 765-771. https://doi.org/10.1016/j.apenergy.2012.12.042

Salmón, I. R., Cambier, N. & Luis, P. 2018. CO_2 Capture by Alkaline Solution for Carbonate Production: A Comparison between a Packed Column and a Membrane Contactor. *Applied Sciences* [Online], 8(6). https://doi.org/10.3390/app8060996

Schütz, M. K., Lopes, N., Cenci, A., Ligabue, R., Dullius, J., Einloft, S. & Ketzer, J. M. 2011. Effect of time on the carbonation reaction of saline aquifers with controlled pH. *Energy Procedia,* 4**,** 4546-4551. https://doi.org/10.1016/j.egypro.2011.02.412

Shu, J., Wu, H., Chen, M., Peng, H., Li, B., Liu, R., Liu, Z., Wang, B., Huang, T. & Hu, Z. 2019. Fractional removal of manganese and ammonia nitrogen from electrolytic metal manganese residue leachate using carbonate and struvite precipitation. *Water Research,* 153**,** 229-238. https://doi.org/10.1016/j.watres.2018.12.044

Shukla, J., Mohandas, V. P. & Kumar, A. 2008. Effect of pH on the Solubility of $CaSO_4 \cdot 2H_2O$ in Aqueous NaCl Solutions and Physicochemical Solution Properties at 35 °C. *Journal of Chemical & Engineering Data,* 53(12)**,** 2797-2800. https://doi.org/10.1021/je800465f

Sibrell, P. L., Chambers, M. A., Deaguero, A. L., Wildeman, T. R. & Reisman, D. J. 2007. An Innovative Carbonate Coprecipitation Process for the Removal of Zinc and Manganese

from Mining Impacted Waters. *Environmental Engineering Science,* 24(7), 881-896. https://doi.org/10.1089/ees.2006.0126

Silva, A. M., Cunha, E. C., Silva, F. D. & Leão, V. A. 2012. Treatment of high-manganese mine water with limestone and sodium carbonate. *Journal of Cleaner Production,* 29, 11-19.

Singh, V., Chakraborty, T. & Tripathy, S. K. 2020. A Review of Low Grade Manganese Ore Upgradation Processes. *Mineral Processing and Extractive Metallurgy Review,* 41(6), 417-438. https://doi.org/10.1080/08827508.2019.1634567

Söhnel, O. & Garside, J. H. 1992. *Precipitation: Basic Principles and Industrial Applications*.

Sorensen, B., Gaal, S., Ringdalen, E., Tangstad, M., Kononov, R. & Ostrovski, O. 2010. Phase compositions of manganese ores and their change in the process of calcination. *International Journal of Mineral Processing,* 94(3), 101-110. https://doi.org/10.1016/j.minpro.2010.01.001

Speight, J. G. 2017. *Lange's Handbook of Chemistry,* New York, McGraw-Hill Education.

Stefánsson, A. 2007. Iron (III) hydrolysis and solubility at 25 degrees C. *Environ Sci Technol,* 41(17), 6117-23. https://doi.org/10.1021/es070174h

Stumm, W. & Morgan, J. J. 1996. *Aquatic chemistry : chemical equilibria and rates in natural waters,* New York, Wiley. http://www.loc.gov/catdir/bios/wiley042/94048319.html

Su, H., Zhou, W., Lyu, X., Liu, X., Gao, W., Li, C. & Li, S. 2023. Remediation treatment and resource utilization trends of electrolytic manganese residue. *Minerals Engineering,* 202, 108264. https://doi.org/10.1016/j.mineng.2023.108264

Sun, K., Luo, S.-H., Du, N., Wei, Y. & Yan, S. 2024. Research progress of lithium manganese iron phosphate cathode materials: From preparation to modification. *Electroanalysis,* 36(8), e202400120. https://doi.org/10.1002/elan.202400120

Sunagawa, I. 2005. Crystals: Growth, Morphology, and Perfection. *Crystals: Growth, Morphology, and Perfection,* https://doi.org/10.1017/CBO9780511610349, 1-295. https://doi.org/10.1017/CBO9780511610349

Tangstad, M. 2013. Chapter 7 - Manganese Ferroalloys Technology. *In:* GASIK, M. (ed.) *Handbook of Ferroalloys.* Oxford: Butterworth-Heinemann. https://doi.org/10.1016/B978-0-08-097753-9.00007-1

Teir, S., Kuusik, R., Fogelholm, C.-J. & Zevenhoven, R. 2007. Production of magnesium carbonates from serpentinite for long-term storage of CO_2. *International Journal of Mineral Processing,* 85(1)**,** 1-15. https://doi.org/10.1016/j.minpro.2007.08.007

Tokuda, H., Kuchar, D., Mihara, N., Kubota, M., Matsuda, H. & Fukuta, T. 2008. Study on reaction kinetics and selective precipitation of Cu, Zn, Ni and Sn with H_2S in single-metal and multi-metal systems. *Chemosphere,* 73(9)**,** 1448-1452. https://doi.org/10.1016/j.chemosphere.2008.07.073

Tu, M., Zhao, H., Lei, Z., Chen, D., Yu, H. & Qi, T. 2015. Aqueous Carbonation of Steel Slag: A Kinetics Study. *ISIJ International,* 55**,** 2509-2514. https://doi.org/10.2355/isijinternational.ISIJINT-2015-142

Tünay, O. & Kabdaşli, N. I. 1994. Hydroxide precipitation of complexed metals. *Water Research,* 28(10)**,** 2117-2124. https://doi.org/10.1016/0043-1354(94)90022-1

Tyler, G. & Yvon, J. ICP-OES , ICP-MS and AAS Techniques Compared. 2003.

U.S. Geological Survey 2024. Mineral commodity summaries 2024. *Mineral Commodity Summaries.* Reston, VA. https://doi.org/10.3133/mcs2024

Verdingh, V. 1981. Precise potentiometric titration of manganese. *Fresenius' Zeitschrift für analytische Chemie,* 307(3)**,** 202-204. https://doi.org/10.1007/BF00527487

Wang, N. F., Fang, Z. J., Peng, S., Cheng, D. X., Du, B. & Zhou, C. B. 2016. Recovery of soluble manganese from electrolyte manganese residue using a combination of ammonia and CO_2. *Hydrometallurgy,* 164**,** 288-294. https://doi.org/10.1016/j.hydromet.2016.06.019

Wang, Y., Zeng, L., Zhang, G., Guan, W., Sun, Z., Zhang, D. & Qing, J. 2019. A novel process on separation of manganese from calcium and magnesium using synergistic solvent extraction system. *Hydrometallurgy,* 185**,** 55-60. https://doi.org/10.1016/j.hydromet.2019.01.008

Wen, J., Tran, T. T. & Lee, M. S. 2024a. Recovery of Pure Co(II) and Ni(II) Solutions from Synthetic Sulfate Leach Liquor of Laterite Ores by Precipitation and Solvent Extraction. *Mineral Processing and Extractive Metallurgy Review,* https://doi.org/10.1080/08827508.2024.2346652**,** 1-10. https://doi.org/10.1080/08827508.2024.2346652

Wen, Q., Liu, B., Zhang, J., Shen, H., Lu, X., Wang, S. & Zhang, S. 2024b. Efficient leaching of manganese from electrolytic manganese residue and recovery of the leaching solution: Reuse and purification. *Separation and Purification Technology,* 332**,** 125648. https://doi.org/10.1016/j.seppur.2023.125648

Whitman, W. G. 1962. The two film theory of gas absorption. *International Journal of Heat and Mass Transfer,* 5(5)**,** 429-433. https://doi.org/10.1016/0017-9310(62)90032-7

Wilhelm, E. 1985. Solubility of gases in liquids: a critical review. *Pure and Applied Chemistry - PURE APPL CHEM,* 57**,** 303-322. https://doi.org/10.1351/pac198557020303

Wu, T., Ma, B., An, Y., Chen, Y. & Wang, C. 2024. Improvement of manganese electrolytic process and secondary resources recovery of manganese: A review. *Process Safety and Environmental Protection,* 186**,** 895-909. https://doi.org/10.1016/j.psep.2024.03.097

Xing, R., Li, R., Xu, Y., Li, B., Liu, J., Liu, S., Luo, D. & Mao, L. 2017. Hydrothermal-assisted homogeneous precipitation synthesis of dumbbell-like $MnCO_3$ nanostructures. *Ceramics International,* 43(16)**,** 14426-14430. https://doi.org/10.1016/j.ceramint.2017.07.212

Xinzhuang, F., Niu, Z., Lin, M., Gao, Y., Sun, W. & Yue, T. 2021. Strengthened Oxygen Oxidation of Ferrous Ions by A Homemade Venturi Jet Microbubble Generator towards Iron Removal in Hydrometallurgy. *Minerals,* 11**,** 1342. https://doi.org/10.3390/min11121342

Ying, M., Yuhua, X. U. E., Hengpeng, Y. E. & Dongyun, D. U. 2017. Selective separation and recovery of manganese from manganese-bearing wastewater using carbon dioxide. *CIESC Journal,* 68(7)**,** 2798-2804. https://doi.org/10.11949/j.issn.0438-1157.20161737

You, Z., Li, G., Zhang, Y. & Peng, Z. 2015. Extraction of manganese from iron rich MnO_2 ores via selective sulfation roasting with SO_2 followed by water leaching. *Hydrometallurgy,* 156. https://doi.org/10.1016/j.hydromet.2015.05.017

Yu, C., Mei, Y., Xue, Y., Wu, C., Ye, H., Li, J. & Du, D. 2019a. A novel approach for recovery of manganese from on-site manganese-bearing wastewater. *Journal of Cleaner Production,* 227**,** 675-682. https://doi.org/10.1016/j.jclepro.2019.04.085

Yu, C., Mei, Y., Xue, Y. H., Wu, C. J., Ye, H. P., Li, J. L. & Du, D. Y. 2019b. A novel approach for recovery of manganese from on-site manganese-bearing wastewater. *Journal of Cleaner Production,* 227**,** 675-682. https://doi.org/10.1016/j.jclepro.2019.04.085

Yu, L., Daniels, L. M., Mulders, J. J. P. A., Saldi, G. D., Harrison, A. L., Liu, L. & Oelkers, E. H. 2019c. An experimental study of gypsum dissolution coupled to $CaCO_3$ precipitation and its application to carbon storage. *Chemical Geology,* 525**,** 447-461. https://doi.org/10.1016/j.chemgeo.2019.08.005

Zeng, H., Wan, Y., Niu, S., Yu, X., Chen, Z., Li, B., Fu, D., Han, P. & Liu, J. 2025. Lithium manganese iron phosphate materials: Design, progress, and challenges. *Energy Materials and Devices,* 3(1)**,** 9370060. https://doi.org/10.26599/EMD.2025.9370060

Zeng, Q., Guo, Y., Niu, Z. & Lin, W. 2013. The absorption rate of CO_2 by aqueous ammonia in a packed column. *Fuel Processing Technology,* 108**,** 76-81. https://doi.org/10.1016/j.fuproc.2012.05.005

Zhang, N., Li, J., Li, H. Y., Liu, A., Huang, Q., Ma, L., Li, Y. & Dahn, J. R. 2018. Structural, Electrochemical, and Thermal Properties of Nickel-Rich LiNiMnCoO Materials. *Chemistry of Materials,* 30(24)**,** 8852-8860. https://doi.org/10.1021/acs.chemmater.8b03827

Zhang, W. & Cheng, C. Y. 2007a. Manganese metallurgy review. Part I: Leaching of ores/secondary materials and recovery of electrolytic/chemical manganese dioxide. *Hydrometallurgy,* 89(3)**,** 137-159. https://doi.org/10.1016/j.hydromet.2007.08.010

Zhang, W. & Cheng, C. Y. 2007b. Manganese metallurgy review. Part II: Manganese separation and recovery from solution. *Hydrometallurgy,* 89(3)**,** 160-177. https://doi.org/10.1016/j.hydromet.2007.08.009

Zhang, W., Cheng, C. Y. & Pranolo, Y. 2010. Investigation of methods for removal and recovery of manganese in hydrometallurgical processes. *Hydrometallurgy,* 101(1-2)**,** 58-63. https://doi.org/10.1016/j.hydromet.2009.11.018

Zhu, C., Wang, H., Li, G., An, S., Ding, X., Teng, H. & Zhao, L. 2017. CO_2 Absorption and Magnesium Carbonate Precipitation in $MgCl_2$–NH_3–NH_4Cl Solutions: Implications for Carbon Capture and Storage. *Minerals,* 7(9)**,** 172. https://doi.org/10.3390/min7090172

Zou, X., Wu, P. & Xie, H.-C. 2016. Effect of High Levels of Impurity Calcium on the Electrochemical Performance of Spinel $LiMn_2O_4$. *International Conference on Material Science and Engineering*. Atlantis Press. https://doi.org/10.2991/icmse-16.2016.84

8 APPENDICES

A.1 Sample calculations for gas flowrate

It was assumed that the drag force (F_D) and drag coefficient (C_D) of air and CO_2 are the same. The drag force is defined by Equation (8-1):

$$F_D(\text{air}) = \frac{1}{2} C_D \rho A_l v^2 \tag{8-1}$$

where ρ is the density of fluid, A_l is the area that is projected, v is the relative velocity between the fluid and material. The densities if air and CO_2 gas are 1.20 g/L and 1.98 g/L. The projected area is the same for both gases since the flowmeter does not change size. The relative velocity of air is 0.5 L/min as measured by the flowmeter.

$$F_D(\text{air}) = F_D(CO_2)$$

$$\frac{1}{2} C_D \rho_{air} A_l {v_{air}}^2 = \frac{1}{2} C_D \rho_{CO2} A_l {v_{CO2}}^2$$

$$\therefore \rho_{air} {v_{air}}^2 = \rho_{CO2} {v_{CO2}}^2$$

$$v_{CO2} = \sqrt{\frac{\rho_{air} {v_{air}}^2}{\rho_{CO2}}} = \sqrt{\frac{1.2 * (0.5)^2}{1.98}}$$

$$\therefore v_{CO2} = \mathbf{0.4\ L/min}$$

A.2 Preparation of the $MnCO_3$ saturated solution

The $MnCO_3$ saturated solution was prepared by mixing 5.0 g of the Merck $MnCO_3$ powder with 5 L of boiling de-ionized water on a hot plate for 10 minutes. The plate was then switched off and the hot mixture was then let to cool while continuously mixing using a magnetic stirrer for 7 days. After that, it was filtered using a vacuum pump and nylon membrane filter with a pore size of 0.22 µm.

Table A.1 shows that the produced saturated $MnCO_3$ solution had insignificant concentration of dissolved metal ions, and therefore, it would not affect the purity of the washed precipitate. The solution also had other metals (Ni, Co, Ba, Cr, Zn, Cu, and Fe) at concentrations less than 0.05 mg/L.

Table A.1: The concentration of the prepared saturated $MnCO_3$ solution.

Element	Mn	Na	K	Mg	Ca	Si	P	Pb	Al	Sr
Concentration (mg/L)	14.1	3.48	1.07	<0.5	<0.5	<0.5	<0.5	<0.25	<0.15	<0.025

A.3 The added amount of ammonia in experiments

The added amount of NH_3 was extracted from the Titrando Metrohm 842 unit as measured by the Tiamo™ software. However, the software provided the volume of the added 28-30 wt.% NH_3 solution and not the actual mass of NH_3. Therefore, the volume was converted to the mass of NH_3 using the lowest concentration of 28 wt.%. Below are the sample calculations for the mass of added NH_3 using the average of **15.13 mL** added 28-30 wt.% NH_3 volume when bubbling CO_2 for 1 hour at pH 6.6. The density of 28-30 wt.% NH_3 was estimated to be **0.9 g/mL** from OLI Stream Analyzer.

$$\text{Mass of } NH_3 = \text{Volume of 28 wt.\% } NH_3 \times \text{density of 28 wt.\% } NH_3 \times 28\%$$

$$\text{Mass of } NH_3 = 15.13\text{mL} \times 0.9\frac{\text{g}}{\text{mL}} \times 28\% = \mathbf{3.81\ g}$$

The added masses of NH_3 as a function of pH and CO_2 bubbling time are shown in Figure A.1 and Figure A.2, respectively.

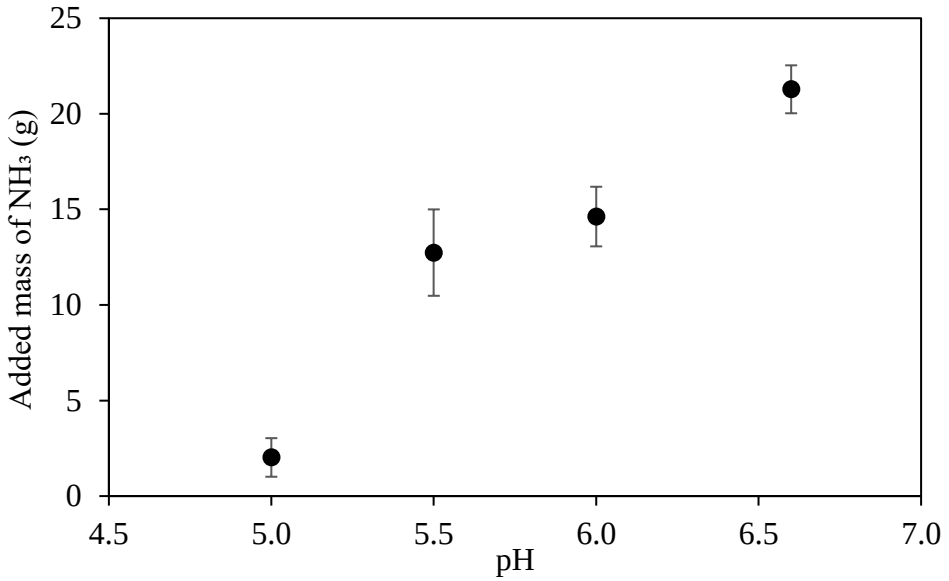

Figure A.1: Effect of pH on the added mass of NH_3.

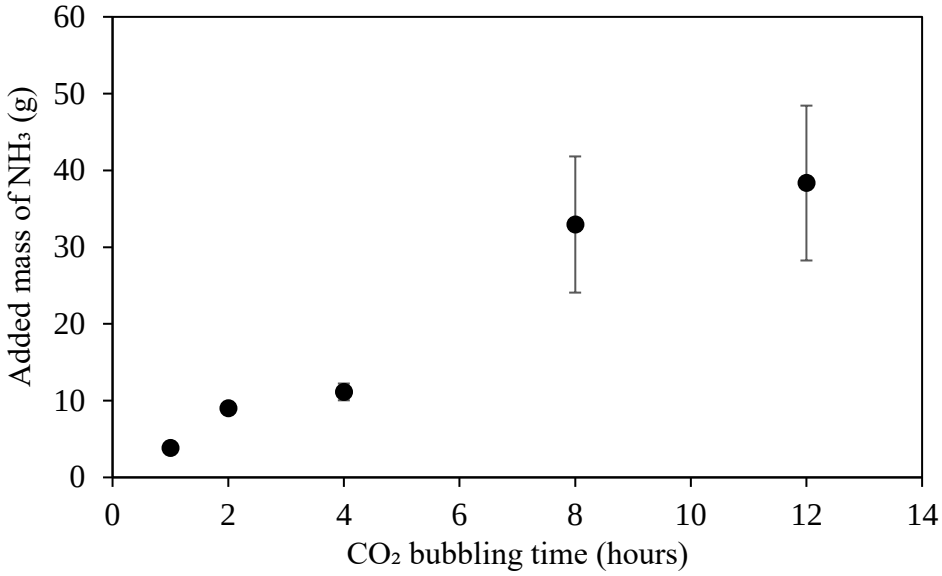

Figure A.2: Effect of CO_2 bubbling time on the added mass of NH_3.